Type-II Shell Evolution in ^{98}Zr

Typ-II Schalenentwicklung in ^{98}Zr
Zur Erlangung des Grades eines Doktors der Naturwissenschaften (Dr. rer. nat.)
genehmigte Dissertation von Waldemar Witt aus Frunse
Tag der Einreichung: 25.01.2019, Tag der Prüfung: 18.02.2019
Darmstadt — D 17

1. Gutachten: Prof. Dr. Dr. h. c. Norbert Pietralla
2. Gutachten: Prof. Dr. Thomas Aumann

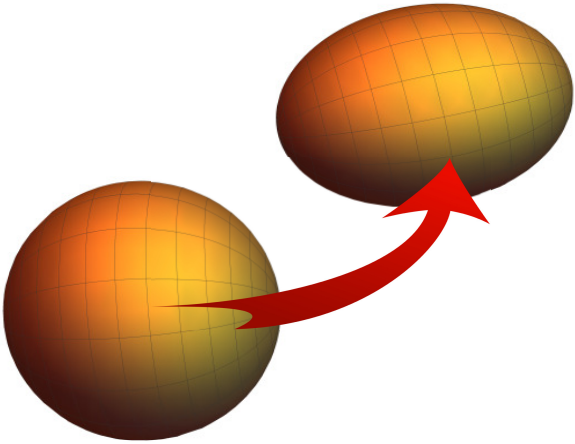

TECHNISCHE UNIVERSITÄT DARMSTADT

Institut für Kernphysik
Fachbereich Physik

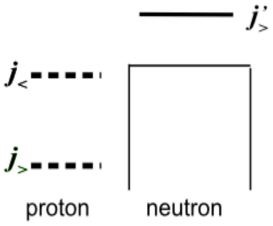

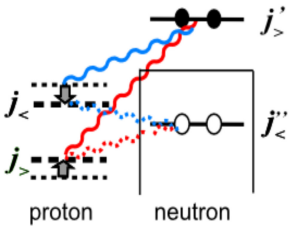

SPONSORED BY THE
Federal Ministry of Education and Research
Grant No. 05P15RDFN1

HGS-HIRe for FAIR
Helmholtz Graduate School for Hadron and Ion Research

Type-II Shell Evolution in ^{98}Zr
Typ-II Schalenentwicklung in ^{98}Zr

Genehmigte Dissertation von Waldemar Witt aus Frunse

1. Gutachten: Prof. Dr. Dr. h. c. Norbert Pietralla
2. Gutachten: Prof. Dr. Thomas Aumann

Tag der Einreichung: 25.01.2019
Tag der Prüfung: 18.02.2019

Darmstadt — D 17

Erklärung zur Dissertation

Hiermit versichere ich, die vorliegende Dissertation ohne Hilfe Dritter nur mit den angegebenen Quellen und Hilfsmitteln angefertigt zu haben. Alle Stellen, die aus Quellen entnommen wurden, sind als solche kenntlich gemacht. Diese Arbeit hat in gleicher oder ähnlicher Form noch keiner Prüfungsbehörde vorgelegen.

Darmstadt, den 25.01.2019

(Waldemar Witt)

Abstract

The atomic nuclei in the Zirconium isotopic chain show a ground-state shape transition uniquely pronounced in the nuclear chart with respect to its abruptness. Between the (mostly) ground-state spherical ^{96}Zr and the ground-state deformed ^{100}Zr, ^{98}Zr lies somewhere between the beginning and the ending of this narrow transition area. This work quantifies the sudden onset of quadrupole collectivity at the transitional nucleus ^{98}Zr.

As measure for quadrupole collectivity, the first-time determination of the $B(E2; 2^+ \rightarrow 0^+_{g.s.})$ transition strength value of ^{98}Zr was performed: A Coulomb excitation experiment with a radioactive ^{98}Zr ion beam at the Argonne National Laboratory (USA) yielded a decisively small upper limit for the transition strength of interest. Complementary, the respective lifetime of the 2^+_1 level was measured with the RDDS method employing a ^{96}Zr(^{18}O, ^{16}O)^{98}Zr two-neutron transfer reaction at IFIN-HH (Romania).

The analysis of the two independent experiments is described and the results combined and discussed. The findings are compared to recent theory and confirm the predicted shape coexistence in ^{98}Zr as effect of type-II shell evolution.

Consequently, the nucleus ^{98}Zr is placed at the brink of the examined structural change and identified as closest nucleus to the critical point of the underlying quantum phase transition.

Zusammenfassung

Die Atomkerne der Zirconium-Isotopenkette weisen in ihren Grundzuständen einen Kernformübergang auf, der in seiner Abruptheit in der Nuklidkarte einmalig ist. Zwischen dem im Grundzustand (größtenteils) sphärischen ^{96}Zr und dem im Grundzustand deformierten ^{100}Zr, lässt sich ^{98}Zr nur vage in dieser schmalen Übergangsregion platzieren. Die vorliegende Arbeit quantifiziert den plötzlichen Anstieg an Quadrupol-Kollektivität im Übergangskern ^{98}Zr.

Als Maß für Quadrupol-Kollektivität wurde zum ersten mal der Wert der $B(E2; 2^+ \rightarrow 0^+_{g.s.})$ Übergangsstärke von ^{98}Zr bestimmt: Durch Coulomb-Anregung eines radioaktiven ^{98}Zr-Strahls in einem Experiment am Argonne National Laboratory (USA) wurde eine entscheidend kleine obere Schranke für den Wert der Übergangsstärke gewonnen. Ergänzend wurde die entsprechende Lebensdauer des 2^+_1 Zustands mit der RDDS Methode gemessen, wofür eine ^{96}Zr(^{18}O, ^{16}O)^{98}Zr Multineutrontransfer - Reaktion am IFIN-HH (Rumänien) angewandt wurde.

Im Rahmen dieser Doktorarbeit wird die Analyse der beiden unabhängigen Experimente beschrieben, sowie ihre Ergebnise zusammengeführt und diskutiert. Die Erkentnisse werden mit moderner Theorie verglichen und bestätigen die vorhergesagte Koexistenz verschiedener Kernformen in ^{98}Zr als Folge der Typ-II Schalenentwicklung.

Folglich wird der Kern ^{98}Zr direkt an die Kante der untersuchten Kernstrukturänderung platziert und als Kern identifiziert, welcher dem kritischen Punkt des zugrundeliegenden Quantenphasenübergangs am nächsten ist.

Contents

1 Introduction

Understanding the world surrounding us has been a major drive for development since the beginning of human existence roughly 300.000 years ago [1]. Analogue to the development process, e.g., in terms of population growth and technical achievements, also the understanding, characterized by predictive description of observations, explosively gained in quality only in the last minor fraction on the time scale of humanity. As can be said about nearly every historical process in retrospective, the history of comprehending nature is a history of misunderstanding, and, since the universal description of everything is nowhere near, can be considered as ongoing. The potential misunderstandings we came to accept as state-of-the-art truth originated in ancient Greece between the 7th and 3rd centuries before the common era, when through the work of philosophy (Thales of Miletus, Leucippus, Plato and Aristotle [2]) mythology and religion as generator of observed phenomena were replaced by natural cause. Science and its main branch physics (literally meaning "nature") were born and in their quest to describe nature shortly after produced the (first) "theory of the universe" (Democritus) introducing the "atom" as indivisible building unit of all matter [3]. Since then, in particular after the Scientific Revolution (16th and 17th centuries), the theory describing natural matter went through a series of major developments of the atomic model by the works of Dalton (1800's), Thompson (1890's), Rutherford (1910's), Bohr (1910's), Schrödinger (1920's), and others [4, 5, 6], eventually literally breaking the former principles by dividing the indivisible.

Contemporary, accepted theory describes the atom as composition of electrons and the composite particles neutrons and protons. The constituents of all matter and their interactions are described in the frame of the "standard model" of elementary particles in terms of the matter particles "quarks", e.g. "up" and "down" quarks forming neutrons and protons, and "leptons" (e.g. the electron found in the atom), as well as the interaction carriers "gauge bosons", which are interchanged between interacting objects [7, 8, 9]. Therefore, the formation of observable matter objects (more precisely: bound states of fundamental particle admixtures) of different scale is a direct effect of the three fundamental interactions; i.e., gravitation producing stellar objects (planets, stars, galaxies), the electroweak interaction holding together molecules (and electrons with the atomic nucleus), and finally the strong interaction bringing together quarks into hadrons (such as protons and neutrons), and causing the formation of atomic nuclei. The unification of all inter-

actions to one single fundamental force, predicted to be applicable at high energy, is the goal of current particle physics theory [8, 10, 11]. While the formation of hadrons is well-described by the theory of quantum chromodynamics (QCD) [7, 12], the binding of neutrons and protons in different compositions into atomic nuclei is considered a residual effect of the strong interaction, and cannot (yet) be described by QCD for heavier nuclei. It is this topic of the nucleon-nucleon interaction that forms the base of nuclear structure physics and this thesis.
Since naturally-existing atomic nuclei can be made up of up to ∼300 nucleons (neutrons and protons), the nuclear forces extracted from QCD for light nuclei can only be generalized to some limited extent [13]. In practice, mainly their general characteristics are accounted for. Those are a strongly attractive effect between nucleons at small distances (∼one femtometre [fm]), which rapidly decreases to negligibility ($\gtrsim$2.5 fm), and a strong repulsion at close distances ($\lesssim$0.7 fm) [10, 14]. To predict the resulting nuclear properties analytically, solving the resulting many-body two-type quantum fluid is then required; which, computationally, can get as challenging as the description might suggest. A phenomenological approach is the systematic modelling of the effective nuclear force in dependence on the nucleons composing a nuclei. For this systematic perspective the nuclei are best represented on the chart of nuclides, i.e. as two-dimensional graph with neutron (N) and proton number (Z) as abscissa and ordinate. This is depicted in figure 1.1 for experimentally observed nuclei (noteworthy, only ∼3600 of ∼6000 theoretically predicted [15]).

Regarding the lifetimes of the resulting nuclei alone (cp. figure 1.1, bottom) reveals a slightly bent diagonal in this chart, at which the nuclei live exceptionally long (>3000 years). They are considered stable (depicted as black squares) and form the so-called "valley of stability" in this nuclear landscape, towards which less-stable nuclei decay. Even more can be learned from systematic observation [17] when the considered property is the excitation energy of the first excited state; i.e. for even N, even Z nuclei the 2_1^+ state with its energy $E(2_1^+)$ (for notation refer to chapter 3). This perspective is shown in figure 1.1 (centre), where nuclei (along blue lines) at certain values of N and Z stand out with significant higher excitation energies as compared to their neighbours. The origin of these special "magic" numbers of N and Z has been the subject of nuclear structure physics of the last century [18], and their consistency for exotic nuclei, i.e. (far) away from the valley of stability, will occupy this scientific field for the decades to come [19]. Again a different picture of the same nuclear chart is obtained when excitation energy ratios are looked at (cp. figure 1.1, top): Emerging patterns in terms of elevated $E(4_1^+)/E(2_1^+)$ ratios between those magic numbers signify the effect of the nuclear interaction on nuclear structure, which is yet to be fully understood. For a complete

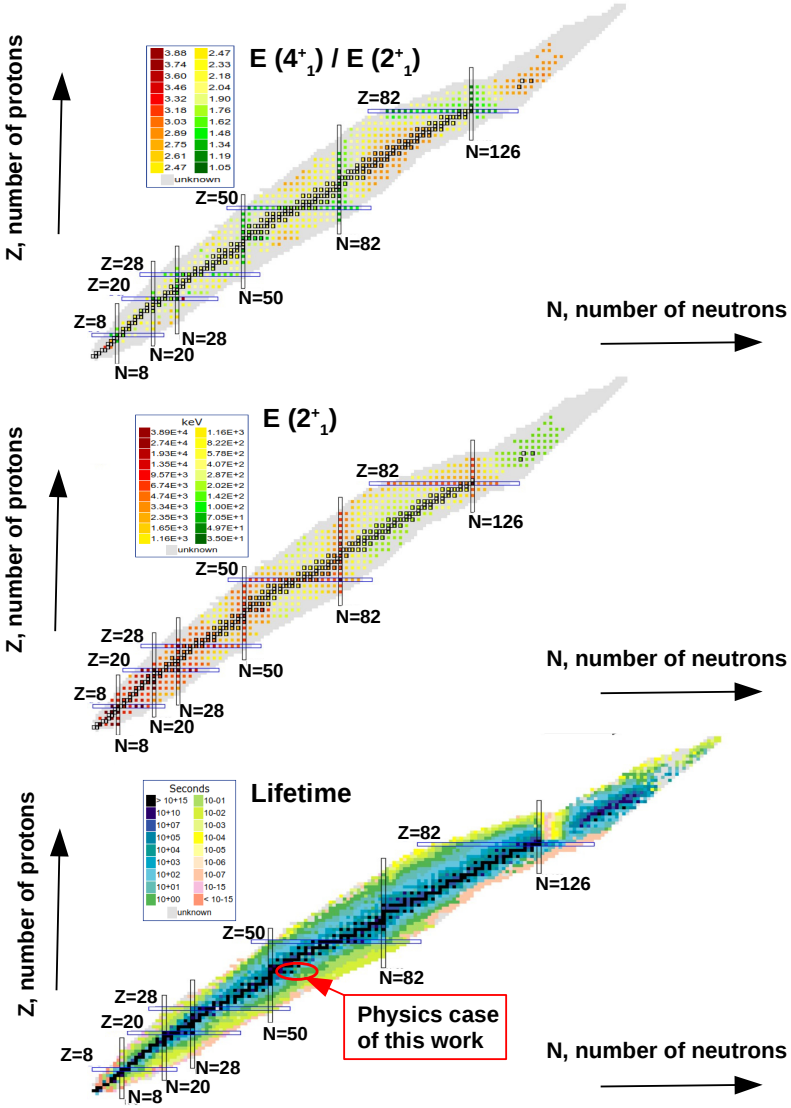

Figure 1.1.: Chart of nuclides depicting different properties of atomic nuclei depending on the number of neutrons N and protons Z composing them: nuclear lifetimes (bottom), energies of the excited levels (centre), and their ratios (top). For details refer to the text. Figures taken from [16] and modified. A zoom is given in figure 1.2.

grasp on the underlying effects causing the observed structural effects in nuclei, a systematic study of the whole nuclear chart from different perspectives in terms of nuclear properties is indispensable. However, as can be observed in figure 1.1 from bottom to top, the amount of experimentally studied nuclei decreases when the required properties increase in quantity. It is the aim of the experimental work described in this thesis to illuminate the nucleus ^{98}Zr within the introduced nuclear scenery, which bears the marks of the nucleon-nucleon interaction in its structure with exceptionally-pronounced concreteness. Its location in the chart of nuclides is pointed at in figure 1.1, and the motivation for the study of exactly this nucleus is introduced in section 1.1.
Compared to the complicated and intriguing structure of nuclei, the structural composition of this thesis can be considered as rather straight forward: In chapter 2 the reader is introduced to a selected part of the theoretical work aspiring to describe the observed nuclear phenomena and predicting unobserved ones. The bridge of this theory to the experimental work performed in the frame of this thesis is built by some basic principles introduced in chapter 3, where the relevant observables of nuclear structure experiments are described. This is followed up by a roundup of established experimental techniques, which were employed in this work, in the course of chapter 4. The application of those methods builds a main part of the thesis, and in chapter 5 the reader learns about the preparation, implementation, and evaluation of two complementary experiments, sections 5.1 and 5.2, respectively. Consequent results of the carried out experiments are discussed conjoined in chapter 6, where they are also compared to theory. The work is concluded in chapter 7 with an additional perspective on potential future work on this topic.

Parts of this work (i.e., the results of the experiment presented in section 5.1) have been published in [20] and highlighted in [21, 22]. They have also been presented at various conferences with preliminary results of the experiment presented in section 5.2 (cp. appendix E).

1.1 Motivation

The phenomenological access to the effects of the nucleon-nucleon interaction on nuclear structure is best approached by describing anomalies in nuclear property systematics over the chart of nuclides. While the association of energies of the lowest-lying excited states of a nucleus and their ratios to the underlying nuclear structure is better illuminated in the following chapter 2, for the motivation of this work's physics case it suffices to regard abrupt systematic changes in those parameters as fingerprints of structural changes. When screening the nuclear chart

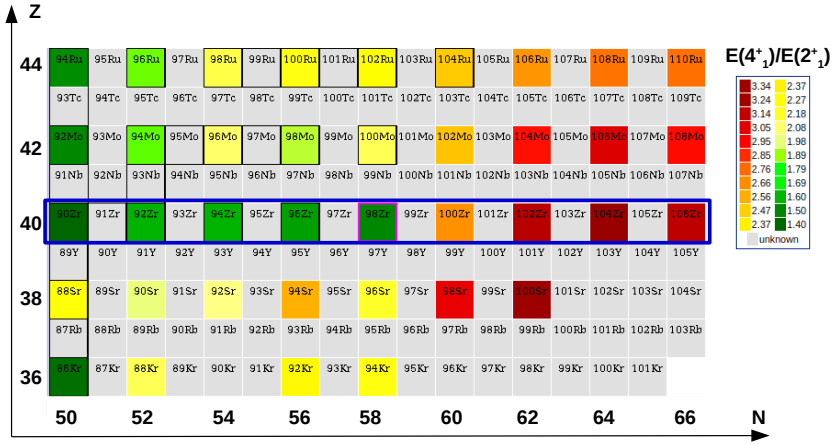

Figure 1.2.: Zoom into the region of this work's physics case in the nuclear chart (region globally depicted in figure 1.1, bottom). The development of excited level energy ratios $E(4_1^+)/E(2_1^+)$ reveals an abrupt change in the Zr isotopic chain (marked in blue) associated with sudden nuclear restructuring. Figure taken from [16] and modified.

for such evolution away from the numbers considered as magic in N and Z (cp. figure 1.1), the region marked in figure 1.1 (bottom), i.e. the Zirconium (Zr) $Z=40$ isotopic chain (and its vicinity) stands out, cp. [23, 24]. In particular, the discontinuity in development of experimental observables associated with nuclear structure between the stable $^{92-96}$Zr ($N=52$-56) and the unstable ^{100}Zr ($N=60$) is uniquely pronounced in the nuclear chart [25, 17, 26], cp. figure 1.2 as zoom into the region of interest.

A closer look at known properties of the nuclei located in this outstanding area of nuclear structure transition is given in figure 1.3, where the level schemes, i.e. the energy patterns of low-lying excited nuclear levels, as well as the structure-associated $E(4_1^+)/E(2_1^+)$ ratios, and additional transition strength (cp. chapter 3) values are depicted for the nuclear area of interest. It is evident that the sudden increase of $E(4_1^+)/E(2_1^+)$ ratios between $N=56$ ($A=96$) and $N=60$ ($A=100$) suggests a structural alteration within few nucleons. The unstable (lifetime smaller than a minute, [16, 27]) nucleus ^{98}Zr finds itself in the center of this transition, and, thus, its study is crucial for the characterization of the observed phenomenon. In

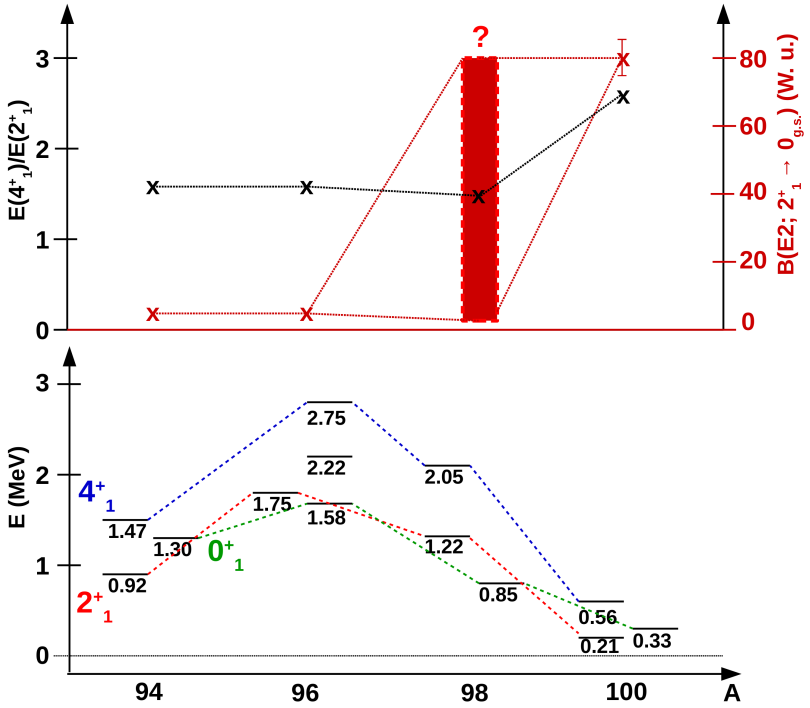

Figure 1.3.: Level schemes and systematic evolution of $E(4^+)/E(2_1^+)$ ratios and transition strength values $B(E2; 2_1^+ \rightarrow 0_{g.s.}^+)$ in the Zr isotopic chain manifesting in a structural change. Data taken from [16, 31, 32, 27, 33].

particular, its $B(E2; 2_1^+ \rightarrow 0_{g.s.}^+)$ value contains much information for this purpose. However, given the available data prior to this work, only a lower, near-zero, limit on this value [28] did not allow for any further interpretation. It was the aim of this work to measure this $B(E2; 2_1^+ \rightarrow 0_{g.s.}^+)$ value of ^{98}Zr to better judge on its role in the found transition, and to test its presumable description by recent theory [29, 30] (cp. section 2.5), with a direct link to the underlying nucleon-nucleon forces.

2 Theoretical Background

The fascinating interplay between theory and experiment, oscillating back and forth towards a better understanding of the phenomena observed in the nuclear landscape and their origin, gives rise to a very vivid and vast field of concepts, models, and prediction. As simple as describing the accumulation of a finite and rather small amount (<300) of only two kinds of particles (protons and neutrons) might sound, when it comes to nuclear systems governed by the strong interaction, one quickly finds that the opposite is the case. Indeed, though continuously growing effort has been made in the theory of nuclear structure since the beginning of the 20th century, nowadays, close to one hundred years later, still no claim to full understanding can be made. Contrary to that, the theoretical background of nucleons and their interaction continues to evolve and no ending to this can be foreseen. Driven by parallel developments in the experimental field, many exciting new phenomena can be expected to not have been accounted for so far.

It is this seemingly endless area of nuclear theory filling so many books that shall be selectively introduced in this section in those parts that are knotted with the experimental contribution of this work. The model descriptions found in this section are parallel to recommendable textbooks to this topic [17, 34, 10], and, of course, there is no evading condensing the topic to a small portion of the whole.

While a usual chicken-or-egg case in other scientific fields, in nuclear structure physics it is a satisfactory find for the experimentalist that the "origin" of this field stems from observation and patterns within them, and thus, theory was driven by experiment. Historically first, and the structure of this chapter subordinates to this time order, exceptionally strongly-bound nuclear systems showed a pattern in the nuclear landscape depending on the number of neutrons and protons building up the nucleus [35]. It is difficult to deny the scepticism of the theoretical community when it came to the naming of this nuclear structure phenomenon: the "magic" numbers were born [36]. Finding an appropriate analogon in atomic physics, a theory to analytically describe the origin of those numbers started to develop, which concluded in the nuclear shell model [18]. This model is presented in section 2.1. By describing individual single particle motions in a spherical potential created by the ensemble of nucleons, the shell model succeeded in reproducing the magic numbers for protons and neutrons after some modifications to the original harmonic oscillator potential. However, already on the way to this, some "arbitrary" "residual" interaction had to be accounted for, and indeed it was found to be

major cause for deviations of shell model predictions when even only slightly deviating from magic nucleon numbers. The observance of collective behaviour, where those residual interactions, previously regarded as perturbations, became essential, and the lack of computational power for the calculation-hungry microscopic shell-model approach motivated the beginning of a different access: the collective models. Those are described in section 2.2, and make use of geometrical nuclear symmetries to describe nuclei deviating from the naive idea of a spherical shape in a macroscopic way. From those models, nuclear deformation and different shapes can be derived, and they are introduced in the subsequent section 2.3.
When the nuclear chart is regarded as a jigsaw puzzle with models defining and describing its separate pieces, the chart's grid-like division by the magic numbers of the shell-model compares to the frame of the whole puzzle. When going on towards further completion, the same question that drove the motivation for associating in-between areas of the nuclear chart with deformed shapes, resurfaces afresh: What happens between? Consequently, the transitions between different nuclear shapes pose a logical continuation to the quest. They are introduced in section 2.3 and prove to rest upon physical principles that are far more general than the specific field of nuclear structure might suggest, cp. section 2.4. This chapter on theoretical background closes by specifying, from a theoretical perspective, the physics case of this work (cp. 2.5), that finds its home in this very twitchy field of transitions.

2.1 Nuclear Shell Model

First approaches trying to explain the "magic"-titled numbers of neutrons and protons, at which nuclei showed exceptionally-strong binding, originated from the following idea around the 1930's [37]: Instead of studying the interaction between every single nucleon making up the nucleus and deducing the observed binding energies from the ensemble of all possible pairings, focus on a single nucleon and understand its motion as effect of its interaction with the remaining nucleus. Thus, the particle could be regarded as independently moving in a potential composed by all other nucleons. This can be formulated in the framework of Hamiltonian mechanics as follows [17]:
Consider the nucleons with masses m_i and momentum $\vec{p}_i$ under the influence of the nucleon-nucleon interaction producing a two-body potential $V_{i,k}$ between each of them. The Hamiltonian H of the system made up of A such nucleons can then be written:

$$H = T + V = \sum_{i=1}^{A} \frac{\vec{p_i}^2}{2m_i} + \sum_{i>k=1}^{A} V_{i,k}(\vec{r_i} - \vec{r_k}) \tag{2.1}$$

The simplification of the two-body potential into a spherical mean field potential $U(\vec{r})$ acting on every nucleon then leaves:

$$H = \sum_{i=1}^{A} \frac{\vec{p_i}^2}{2m_i} + U_i(\vec{r}) + H_{residual}, \tag{2.2}$$

with $H_{residual}$ absorbing everything that gets lost by this approximation; i.e.

$$H_{residual} = \sum_{i>k=1}^{A} V_{i,k}(\vec{r_i} - \vec{r_k}) - U_i(\vec{r}). \tag{2.3}$$

The single particle energies E of the nucleons, each characterized by its wave function Φ, can be obtained by solving the Schrödinger equation [6]

$$H\Phi = E\Phi = E_{nlm}\Phi_{nlm}, \tag{2.4}$$

making use of the good quantum numbers of a spherical potential with n: the radial quantum number, l: the orbital angular momentum quantum number (historical notation: l = 0, 1, 2, 3, 4, 5, ... → s, p, d, f, g, h, ...), and m: the eigenvalue of its projection l_z on the z-axis. Without going into detail here (instead consider the description given in e.g. [10]), it can be quite eye-opening to realize, that alone the inherent central and centrifugal effects on the nucleons, and the exclusion by the Pauli exclusion principle [38], suffice to create an energy distribution, with density accumulations divided by spaces, already resembling the observed magic structure: The input of the most simple spherically-symmetric binding potential, i.e., the harmonic oscillator potential, results in the description of the found magic numbers to some degree, with the nucleons occupying shells of the harmonic oscillator defined by $N = (2n-1)+l$. This is depicted on the left hand side of figure 2.1. However, the energies obtained this way are degenerate; i.e., for each oscillator shell N more than one combination of n and l yields the same energy. This calls for the Pauli principle that effectively limits the amount of nucleons occupying such an orbit. Taking into account the intrinsic spin $s = 1/2$ of a nucleon occupying an orbit corresponding to l, the total angular momentum j can then be written as $j = l + s$. Thus, $2j+1$ nucleons can occupy one orbital before the energetically next one has to be filled.

However, this simple idea does not yet precisely describe all observed magic numbers, and, in particular the higher ones could not be reproduced. It was in the late 1950s that refinements and independent further developments [39] concluded in the first total description of the magic numbers. In a nutshell, those developments included the modification of the used potential, the inclusion of an effective l^2 term, and finally the coupling of the nucleon spin $\vec{s}$ and the orbital angular momentum $\vec{l}$ to a spin-orbit term. Sparing the reader with details here (please refer to the textbooks for more information), those modifications ensured that the effective potential affecting the single particle (the whole original idea) showed an interior constancy, and that nucleons occupying higher angular momentum orbitals were effectively drawn stronger towards the center. In particular, the addition of the spin-orbit term took into account the (purely quantum-mechanical) like-spin coupling between orbital and nucleon spin and accounted for nuclear surface effects on the potential. The effective force of this was found to be comparable in strength to the effect caused by the initial harmonic oscillator potential. The resulting single particle energies finally reproduce all the observed magic numbers. This is depicted in figure 2.1.

The major theoretical breakthrough describing the nuclear structure at closed shells forms the foundation of nuclear structure physics. Since, as can be deduced, the total angular momentum of a closed shell is $J = 0$, all nuclei made of a closed shell nucleus and one more or less neutron or proton, can be described by it to some degree as well. However, the dependency of the calculated single particle energies on nucleon number and the whole (substantial) area of the nuclear chart located between those closed shells are a realm not covered by this simple model. In particular when going away from closed shells, the effects of the so-far neglected residual nucleon-nucleon interaction have to be considered as they become predominant. From a practical calculation point of view: Even though the then-needed diagonalization of the residual interaction is technically achievable, the spanned dimension space very quickly exceeds computational limits. While truncations and/or simplifications (e.g. Monte Carlo methods [40, 41]) remedy this issue to some degree at the cost of precision, in general different physics approaches are needed to describe nuclei between closed shells. Note, that model calculations performed using the Monte Carlo Shell Model (MCSM) approach will be referred to in chapter 6 of this work.

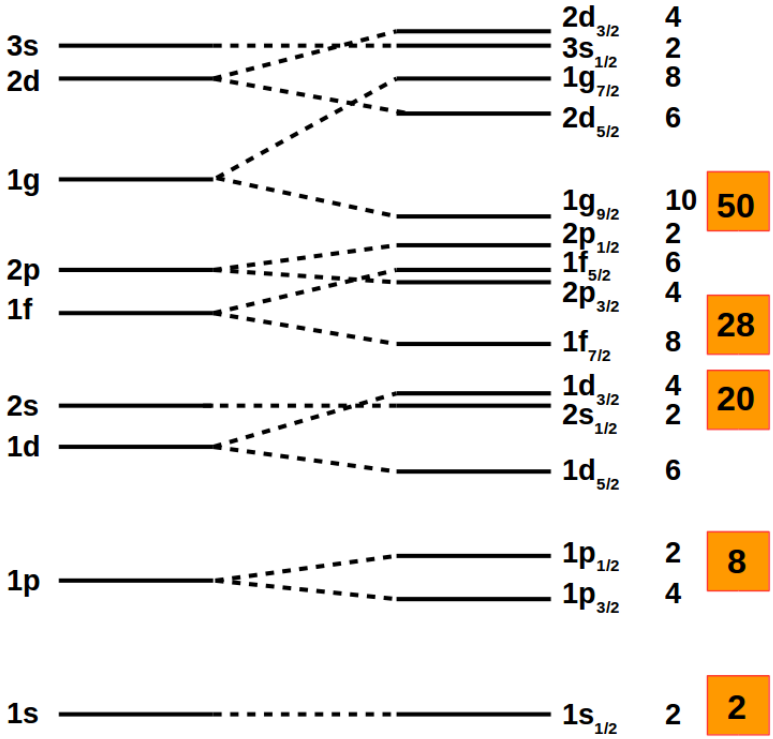

Figure 2.1.: Single particle energies calculated in the frame of the nuclear shell model with an initially harmonic oscillator potential (left), and with the inclusion of $\vec{l}^2$ and the $\vec{l} \cdot \vec{s}$ modifications (right). The resulting orbitals reproduce the observed magic numbers.

2.2 Deformation and Collective Nuclear Models

The whole idea that so beautifully describes the formation of nuclear shells, i.e. that of independent particles in a spherical potential, breaks down when leaving the stable patterns close to magic numbers in the nuclear chart. Different approaches to describe this majority of nuclei follow the logical deductions from the contradiction: either the potential has to be nonspherical, and/or the particles' motions depend on each other.

The former idea was formalized by Nilsson in the 60s [42] and builds on the line of thought that a particle distribution over the nuclear orbitals no longer shows uniformity when going (far) away from closed shells. Since the effective potential thus follows this distribution, it can no longer be spherical but has to be deformed. When regarding single particle energies of the nucleons in this deformed potential (still no interaction here), additionally to the spherical origin, the orientation of the nucleons towards the nuclear symmetry axis comes into play. The correlated quantum number K introduced here, which is then depending on the deformation of the potential, is then employed to characterize Nilsson orbitals and follow the single particle energies shifting around as a function of deformation. Since this model was not employed in the current work, for more than a brief introduction the reader is referred to the canonized literature.

For the second approach the nucleus is best pictured as an accumulation of water-molecules that form a drop by mutual interaction. Regarding nuclear excitations, this macroscopic description of microscopic objects was transferred from water forming drops to nucleons forming nuclei by Bohr, Mottelson and Rainwater [43]. Fittingly, it was introduced as the liquid drop model and with the influence of other contributors over the time became the collective model [44]. Analogue to the water drop the motion of the nucleus can therefore be described as deformations of its surface, with nuclear excitations corresponding to rotations and surface vibrations. This is, in general, formalized [17] in the multipole expansion of the nuclear surface R:

$$R(\phi,\theta,t) = R_0\left[1+\sum_{l=0}^{\infty}\sum_{m=-l}^{l}\alpha_{l,m}(t)Y_{l,m}(\theta,\phi)\right], \tag{2.5}$$

with R_0: the mean nuclear radius, and with $\alpha_{l,m}(t)$ and $Y_{l,m}(\theta,\phi)$: the time-dependent amplitude and direction of the deformation, respectively. A differentiation can be made on the multipole order l of the deformation ($l=0$: monopole, $l=1$: dipole, etc.) with the respective deformations corresponding to oscillations ($l=0$) [45, 46, 47], relocations $l=1$ [48, 49, 50], and non-spherical oscillations ($l\geq 2$) [51].

The most-usual ones and of relevance to the subject of this work, are the deformations of second multipole order; i.e., the quadrupole deformations. Following the above introduced nuclear surface, they are expressed to lowest order of β as

$$R(\theta) = R_0(1 + \beta Y_{20}(\theta)), \tag{2.6}$$

introducing the deformation parameter β as a measure for quadrupole deformations, with the case of no deformation described by $\beta = 0$. To take into account axial asymmetry of the deformation a parameter γ is introduced, ranging from $\gamma = 0^\circ$ (prolate) to $\gamma = 60^\circ$ (oblate deformation).
It is worth noting, that the macroscopic description of nuclear deformation by collective motions can be derived from the microscopic origin as proven by the random phase approximation [52].
Apart from those two (eventually converging) models tackling the world between closed nuclear shells, another, more recent, take on this problem was taken by the so called Interacting Boson Approximation (IBA) [53], that proved to be quite effective. The corresponding model (IBM) builds on the foundation so well presented by the shell model: closed shells. For nuclei away from those, the additional nucleons, and only those, are considered to contribute to collective excitations, and thus form the valence nucleons. They are paired into bosons of different total angular momentum L and the nucleus' Hamiltonian can then be expressed in terms of their creation and annihilation operators within the second quantization formalism. The combinations of those operators are then used to describe the conserved quantum numbers of the corresponding physics. The result is the correspondence of nuclear potentials (shapes) to the dynamical symmetries of group theory [54] and the description of spherical nuclei (vibrational excitations analogue to the U(5) symmetry group) and deformed (rotational, and γ-soft) nuclei. Since group-theoretical symmetries construct a rather simple algebra, in which the bosons responsible for collective motions are mathematically addressed, excitation energies and transitions can be described well analytically. The resulting symmetries are usually depicted spanning a triangle resembling a phase diagram (e.g. P, T, V of water). This is depicted in figure 2.2 including the characterizing model benchmarks of typical experimental observables.

To sum up the introduced models, nuclear structure theory is able to describe spherical closed-shell nuclei microscopically and deformed nuclei distanced from those by deformed potential and macroscopic, geometric formalisms. The IBM associates all encountered nuclear shapes with algebraic symmetries, and describes excitation behaviour of nuclei corresponding to these shapes.

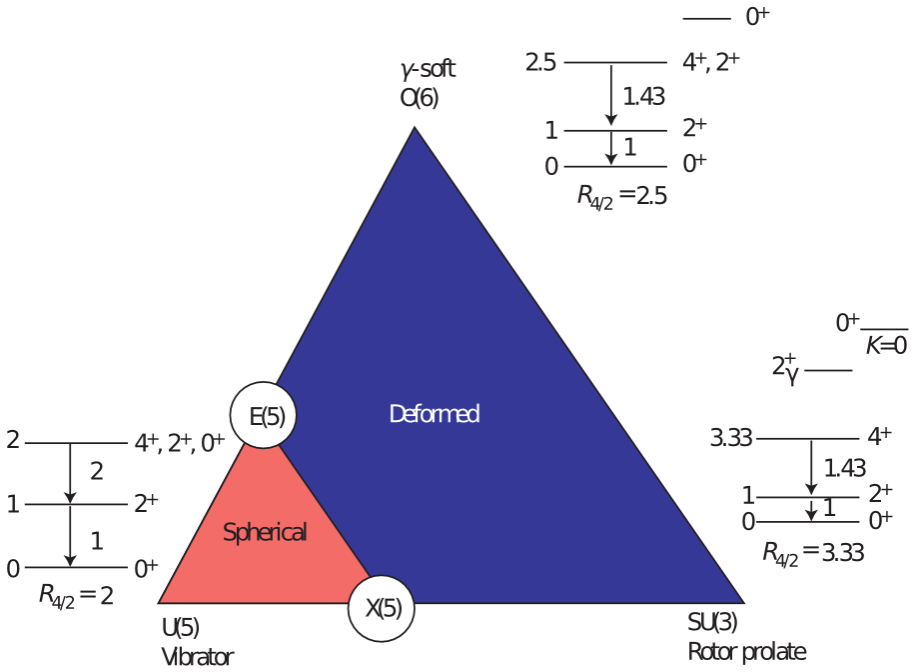

Figure 2.2.: Symmetries of the IBM, and their corresponding nuclear shapes. Additionally, the specific values for experimental observable ratios $R_{4/2} = B(E2; 4_1^+ \rightarrow 2_1^+)/B(E2; 2_1^+ \rightarrow 0_1^+)$ are shown. Also depicted are the critical transition points between vibrator and γ soft nuclei [E(5)], and between vibrator and prolate rotor [X(5)]. Figure taken from [55].

2.3 Nuclear Shape Transitions and Transitional Nuclear Shapes

When trying to apply the above-introduced theoretical models to the nuclear chart, one finds that only few of the nuclei composing it, conform taking a model shape. Indeed, the expected contribution to nuclear shape by valence-nucleon interaction eventually leads to a deformed character at mid-shell regions. However, this is a deformation process gradually developing with (usually) the addition of valence nucleons, and therefore most nuclei found between closed shells show some mixing of different model shapes (or IBM symmetries). As they thus can be located in the transit between two distinct nuclear shapes, they form the group of so-called transitional nuclei. The shape transitions characterizing them, often referred to as structural evolution, can be regarded (again) in the two frames that were employed to look at distinct shapes in first place. In the former the nuclear potential is (of course) a harmonic oscillator at closed shells, which becomes wider and smaller (i.e., less steep) when moving towards mid-shell, where it is completely deformed. A quantification of this process can then be achieved by the development of β (and γ) during this transition. The second approach, that of collective motion, regards the transition between two nuclear shapes as a mixing of two distinct configurations with the degree of mixing between deformed and spherical configuration as critical measure for the transition. Conclusively, a systematic behaviour of the model predictions for low-lying excitation energies corresponding to such transition towards mid-shell regions, is observed. A typical (schematic) pattern is depicted in figure 2.3.
While the transition covered in the frame of this work is following this interplay of macroscopic, collective behaviour originating from microscopic cause, it is worth noting that the topic of transitional nuclei is by now also addressed within the IBM. The axis of the symmetry triangle (cp. figure 2.2), corresponding to the transitions from vibrator to γ-soft and from vibrator to symmetric rotor, within that model, have been extended (out of the IBM scale) [56, 57]. The newly found approximate analytic expressions E(5), and X(5), respectively were shown to describe nuclei at the critical points of this transitions. These can be generalized to analytic descriptions between X(5) and the SU(3) limit or between E(5) and the O(6) limit, respectively [58].

2.4 Quantum Phase Transitions

It is of surprising analogy that the original model to describe collective motion of nucleons, i.e. that of the liquid water drop, still shows parallel concepts when it comes to describing the transitions between the incidentally deduced nuclear

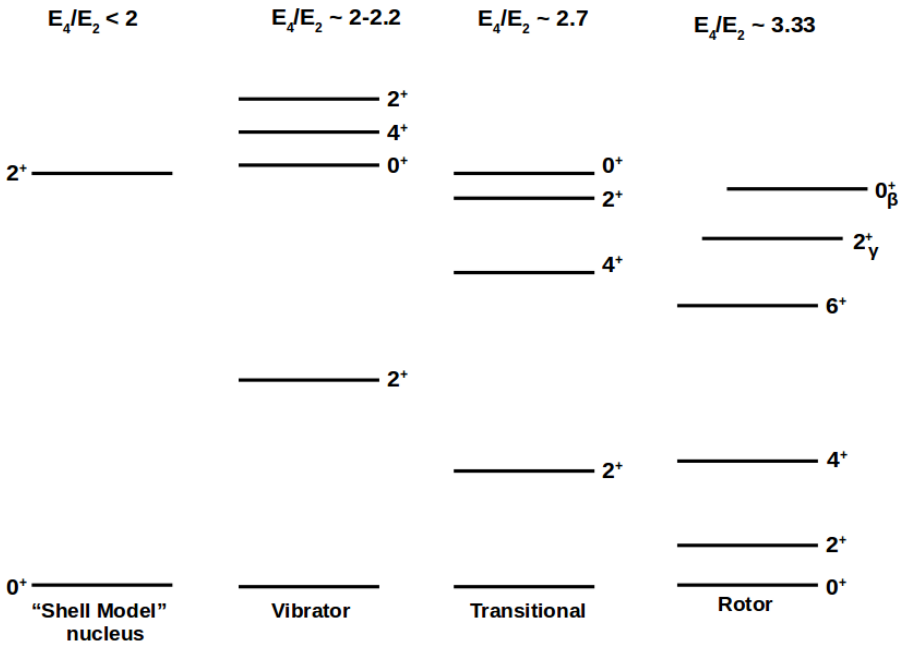

Figure 2.3.: Ideal energy level patterns in nuclear shape transitions from closed shell to mid-shell. The ratio $E_4/E_2 = E(4_1^+)/E(2_1^+)$ is characteristic for the model shape of the nucleus. Figure similar to [17].

shapes. When talking about water and transitions, the prominent transitions from solid to liquid to gas, and vice versa, are one of the oldest and most-studied natural phenomena [59]. The extension of their description to phases depending on certain control parameters (e.g. temperature), and, in particular, the phase transitions, can be borrowed and implemented in the field of nuclear structure physics. The general concept of a phase transition is the change of an observable depending on a control parameter at the critical value of this parameter. Depending on the degree of abruptness of this change, the phase transition is characterized in different orders. Mathematically, this order of the phase transition corresponds to the order of derivative of the observable with respect to the control parameter, which first shows a discontinuity. For clarification, this differentiation is exemplary depicted in figure 2.4 for the case of macroscopic transitions as introduced by Ehrenfest [60].

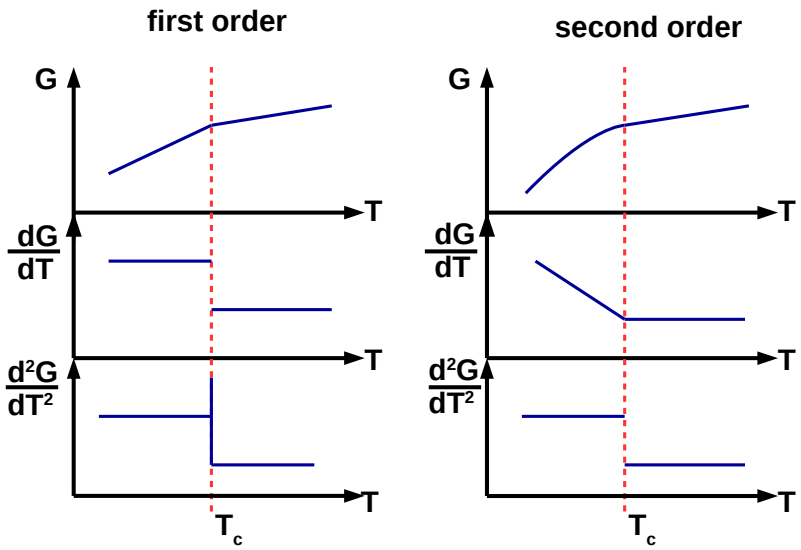

Figure 2.4.: Orders of phase transitions explaining the concept. Left-hand side: a first order phase transitions (e.g., liquid to gas) defined by an abrupt change of the observed parameter G at the critical value of the control parameter T_c and a discontinuity in the first derivative (below); r.h.s.: second-order phase transition (e.g., paramagnetic to ferromagnetic) with a discontinuity in the second order derivative (below).

When transferring this concept to the quantum system [61] of finite nuclei with the nuclear shapes corresponding to phases, the number of valence nucleons, since discrete by quantum nature, cannot be used as control parameter. However, since nuclear properties directly depend (among others) on discrete numbers of nucleons, the use of such a correlated observable, e.g. a single particle energy, becomes valid as control parameter for quantum phase transitions. Compared to classical macroscopic phase transitions, for nuclei this means that critical transition points do not necessarily, and actually very unlikely do, correspond to actual nuclei. Instead they are found within a nuclear region and usually between two distinct nuclei. The transfer from infinite to finite (nuclear) systems leads to a requirement for taking finite-size scaling effects into account [62], which effectively smear out the discontinuity; i.e., towards an observed continuum in the control parameter. "Effective" critical nuclei in such a finite-particle quantum phase transition can be related to the turning points (zeroes of the second derivatives w. r. t. the control parameter) of the observable [63], cp. figure 2.5. The appearance of both, first and second, orders of phase transition within one system is not the general case and makes nuclei special in this regard.

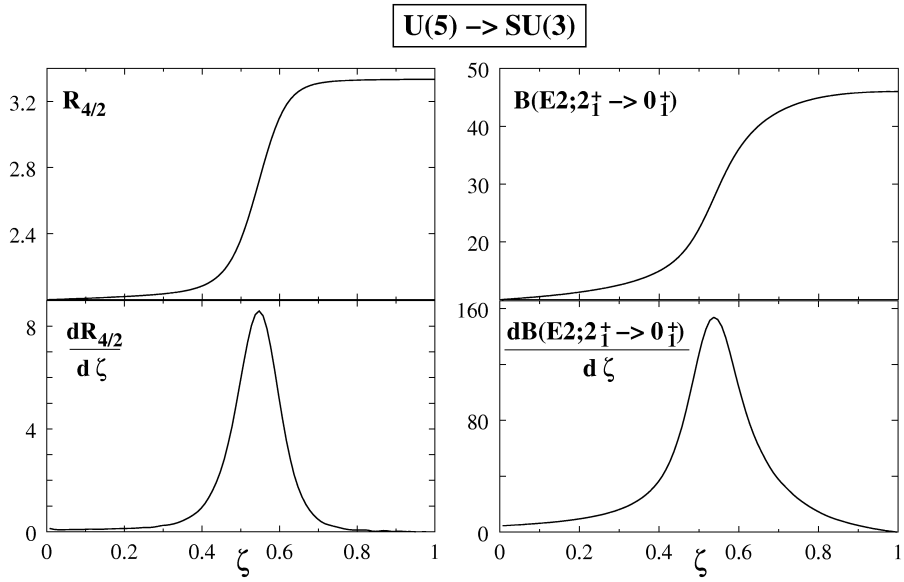

Figure 2.5.: Systematic behaviour of nuclear structure observables $R_{4/2} = E(4_1^+)/E(2_1^+)$ and $B(E2; 2_1^+ \rightarrow 0_1^+)$ as function of the IBA control parameter ς for the transitional region between U(5) and SU(3) symmetries. Already for the small boson number calculated (N = 10), singularities in the derivative identify effective critical points in this transition. Figure taken from [63].

The abrupt change of the nuclear shape at the critical point is related to the simultaneous appearance of both configurations. While the critical point as continuous value in a discrete parameter system is hard to coincide with actual nuclei, this shape coexistence is very well observable in reality and was proven to be a reliable companion of quantum phase transitions in transitional nuclei [64]. A differentiation of appearing coexisting shapes within one nucleus has to be made between strongly-mixing potentials of the two distinct configurations and a high/wide potential barrier separating them [65], cp. figure 2.6. For the former case, the approximation of the effective collective potential by an infinite square well (corresponding to one single valence space), as done within the X(5) and E(5) solutions, is applicable. This kind of coexistence is found in transitional mid-shell nuclei, e.g. ^{154}Gd and ^{152}Sm. The coexistence of weakly-mixing configurations is a relatively-recent field, and has to be treated differently, since the description

within one valence space does not apply. For this, the nucleus ^{98}Zr studied within this work is a prime example, and the coexistence of structures with different degree of (quadrupole) collectivity was experimentally confirmed [66] very lately.

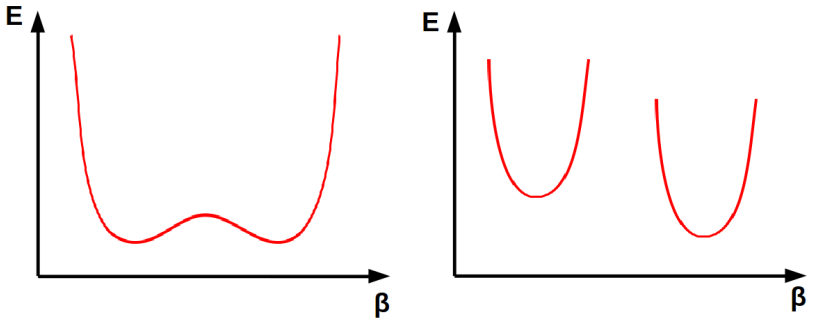

Figure 2.6.: Two different cases of coexisting structures with different degree of deformation β and their respective (effective) potential energies E. Left-hand side: A low barrier allows for strong mixing and the treatment within one valence space. Right-hand side: A high barrier and/or large difference in degree of deformation causing weakly-mixing potentials.

2.5 Shell Evolution induced by Nuclear Force

The phenomenon of shape coexistence in transitional nuclei can be successfully described by developments of the shell model in the late 1990s [64, 67, 68] and was recently linked to the microscopic origin in the nucleon-nucleon interaction [69], and in particular the monopole part of the tensor force [70]. Without going too much into detail here (please refer to [69] and references given therein), the effect is a shift of closed-shell single-particle energies caused by the nucleons occupying certain orbitals. This energy shift $\Delta\epsilon_j$ of the regarded orbit j can be written as

$$\Delta\epsilon_j = v_m(j, j')n_{j'}, \tag{2.7}$$

with v_m: the monopole interaction, j': the additionally occupied orbit, and with the expectation value of the occupation number operator $n_{j'}$. This is best depicted in schematic way, as done in figure 2.7.

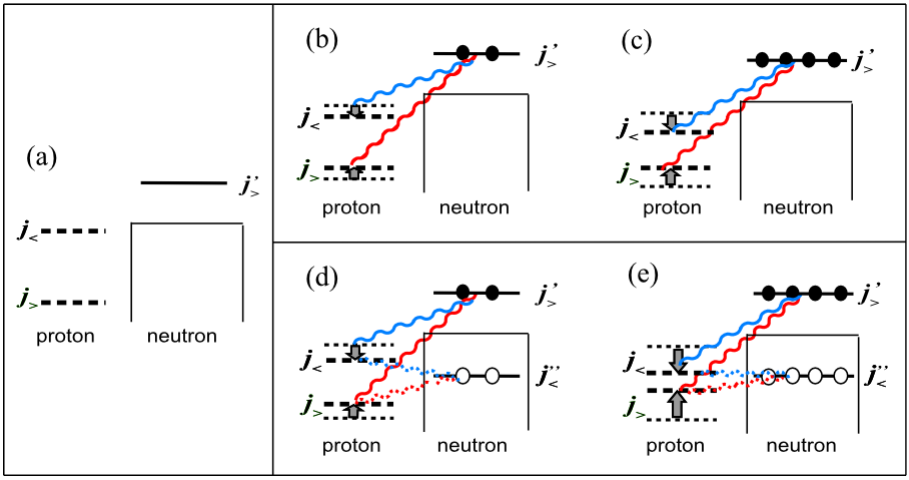

Figure 2.7.: Nuclear shell evolution as direct effect of the nuclear tensor force (wavy lines; blue: attractive, red: repulsive): (a) closed-shell orbitals, (b) type-I shell evolution by addition of valence neutrons, and (d) type-II shell evolution by excitation of neutrons into a higher orbital; (c), (e) increase of the effect for the respective case. For details refer to the text. Figure taken from [69].

Considering proton and neutron orbits, as presented in figure 2.7 (a), as spin-orbit partners, i.e., $j_> = l + 1/2$, and $j_< = l - 1/2$, the tensor force is attractive only for the coupling between the $j_<$ and $j'_>$ orbits, and repulsive otherwise [70]. The effects of this interaction can then be regarded by the occupation of $j'_>$ by additional neutrons, cp. figure 2.7 (b), equivalent to what happens in an isomeric chain of nucleons: the tensor force effectively reduces the spin-orbit splitting between $j_>$ and $j_<$. Due to the linearity of the interaction, doubling the occupation number $n_{j'}$ doubles the single particle shift and further reduces the splitting, cp. figure 2.7 (c). Thus, a shell evolution takes place, and eventually (with enough added neutrons), the orbits can even interchange in relative energy. This is in particular of interest for the subject of disappearing classical magic numbers and appearance of new ones in neutron-rich nuclei [19, 30]. This idea of nuclear structure change as effect of the tensor force due to the change in nucleon number defines the so-called type-I shell evolution.

Since the main cause for shell evolution in this picture is the nucleons' occupying a higher orbit $j'_>$, the actual addition of, here, neutrons is not necessary. This idea provides the base for type-II shell evolution and is depicted in figure 2.7 (d, e):

Here, the particle-hole excitation is sufficient to cause the shift of orbits; similar to the case of added neutrons. Additionally, by removing the neutrons from the lower orbit $j''_<$ (adding holes), the previously opposite effect of the tensor force, i.e. splitting the proton orbits, is weakened and an effective increase of the principle of type-I shell evolution is observed. Not only is the effect of type-II shell evolution, thus, potentially stronger, but also, when considering multi-particle-hole excitations, cp. figure 2.7 (e), the scaling with valence neutrons is significantly more pronounced.
The introduced shell-evolution mechanisms are interlinked with the previously discussed quantum phase transitions in transitional nuclei. As presented in particular in the case of type-II shell evolution the effective reduction of single particle energies can become dominant (i.e. on the scale of the shell-model single particle energies themselves) when regarding collective excitations. This raise in collective behaviour is exactly what motivated the geometric perspective on nuclei. With the quasi-control parameter of nucleon number not changing for a collective excitation within one nucleus, and as the distances of the potential control parameter single particle energies are reduced, the abruptness presupposing a quantum phase transition can (easily) be complied with. Considering the appearance of orbital crossing in the frame of this evolution, i.e. single-particle energies exchanging their ordering, a structural change is evident. Bringing those two developments together the ingredients for a first order quantum phase transition in existing transitional nuclei can be deduced from the nucleon-nucleon interaction.

3 Basic Principles

In this chapter some fundamental aspects of nuclear structure physics are introduced, in particular to the reader unfamiliar with the topic of nuclear lifetime and transition strength measurements. They serve as interface between the theoretical model world presented in chapter 2 and the experimental access to nuclear structure manifesting in relevant observables, cp. chapter 4. Since the interplay between theory and experiment is the driving force for scientific progress, the principles presented here have a long historical background. During their development and depending on the context, however, not only did their content change, but also different notations and conventions have been established. It is the aim of the following introduction of principles to set a standard for expressions that are used throughout this work. As such, only the main principles that are essential for understanding the work are presented in a condensed form. For more details on specific topics and explanations on basics considered of minor importance for this work, the reader is referred to the established general literature, e.g. [6, 71] and the references given.

3.1 Nuclear Levels and Transitions

While the content of theoretical descriptions of atomic nuclei is rich to a degree that, hypothetically, an infinite amount of benchmarking values can be constructed and defined, the experimental approach is limited to very few distinct variables to serve as observables. This limitation stems in first place from the need for the physically concrete character of the variable (as opposed to mathematical abstracts in theory). Also the means of measuring the variable in terms of technical feasibility (instruments, methods, etc.) is a prerequisite. The highest precision for physical measurements can be achieved when the subject of measurement is an energy (corresponding to a frequency) and/or time (difference), and, hence, those are the two dimensions, in which also the easiest-accessible observables of nuclear structure physics can be found. "Fortunately", those happen to also be values obtainable by theory. The direct link between energies predicted by nuclear theory and energies measured in experiment can be established by regarding at least two energetically-distinct nuclear levels, as depicted in figure 3.1, and in particular the energy difference between them that can be measured. Here, we focus on a

transition by emission of a γ-quantum (a γ decay) as this kind of decay is the predominant case in the course of this work. Note, that transitions of other kinds, e.g. involving the emission of particles or by absorption of energy/particles, exist as well, and usually even take place in mutual combination.

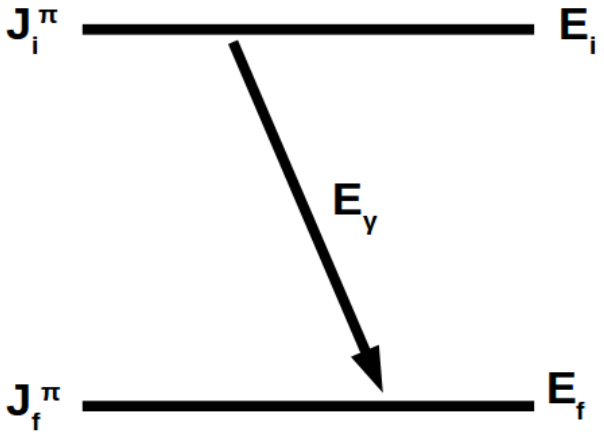

Figure 3.1.: Two nuclear levels and a transition between them linking predictions made by theoretical models and experimental measurement. Also, characterizing quantum number of the levels are shown for identification.

Due to the limitation set by the Pauli principle, fermions (in the nucleus the nucleons neutrons and protons) can only occupy the same orbital (associated with its energy) when they differ in at least one other quantum number. Thus, the formation of so-called orbitals, comparable to shells of the atomic shell model, takes place, in which a fixed set of particles (according to independent quantum numbers) resides at the same energy (cp. section 2.1). The total spin J and the parity π of the nucleus at different energies E_i and E_f are used to characterize the nuclear levels. The absolute value of those energies is related to the so-called ground-state; i.e, the level with minimal achievable sum energy in a nuclear system. Occupations of energetically higher-lying levels, connected with a gain in total system energy, are referred to as excited states. For minimizing the total energy, eventually a de-excitation, a decay, takes place, as depicted in figure 3.1, in which the surplus energy is released, numerically the difference between the energies E_i and E_f of the two involved levels. In the case of γ decays, the transition taking place between two levels is characterized by its multipole order l and radiation character σ as ei-

ther electric or magnetic depending the parity π of the involved levels: electric (E) for $\pi_i \cdot \pi_f = (-1)^l$, and magnetic ($M$) for $\pi_i \cdot \pi_f = (-1)^{l+1}$. For a transition to be physically possible, the multipole order is limited by the Pauli principle as well as parity and momentum conservations concluding in the selection rule [71]

$$|J_f - J_i| \leq l \leq J_f + J_i. \tag{3.1}$$

The likelihood of an allowed transition to happen can be expressed by its transition rate $\lambda(\sigma l)$. At this point the other main observable accessible by experiment comes into play, namely the mean lifetime τ. It describes the mean time an excited state takes to decay into a less-excited or the ground state and is inversely proportional to the transition rate; i.e., $\tau = \frac{1}{\lambda(\sigma l)}$. Connected by the transition strength B to theory this observable serves as direct model-independent probe on the wave functions $|\phi_i\rangle$, $|\phi_f\rangle$ of the involved states: With the transition operator $T_{\sigma l}$, the reduced transition strength is defined as [71]

$$B(\sigma l, J_i \to J_f) = \frac{1}{2J_i + 1} \sum |\langle J_f || T_{\sigma l} || J_i \rangle|^2, \tag{3.2}$$

and expressing the transition rate by the reduced transitions strength establishes the link

$$\lambda(\sigma l) = \frac{8\pi(l+1)}{\hbar l((2l+1)!!)^2} \left(\frac{E_\gamma}{\hbar c}\right)^{2l+1} B(\sigma l, J_i \to J_f). \tag{3.3}$$

Implied within this equations is the higher probability for magnetic to electric transitions of the same multipole order, and the suppression of higher-order transitions. Two formalisms applying the above defined transition strength and lifetime that find use in this work are the decay laws and the Weisskopf estimates:

Decay Laws

Since the experimental access to level lifetimes depends on the observation of the level's decays, for an ensemble of excited nuclei conclusion on the lifetime can be made by the amount of non-decayed nuclei at a given time $A(t)$ (e.g. [10])

$$A(t) = A(t=0) \exp\left[\frac{-t}{\tau}\right], \tag{3.4}$$

and for a decay passing through a chain of excited levels the decay rates for a given level are described by a set of differential equations known as the Bateman equations [72]. In particular, for the decay rate of a level of interest with λ_{int},

which is populated by another decay, a so-called feeder, with λ_{feed}, the decay law can be written as

$$A_{int}(t) = A_{feed}(t=0)\frac{\lambda_{int}}{\lambda_{int}-\lambda_{feed}}(\exp[-\lambda_{int}t]-\exp[-\lambda_{feed}t]) + A_{int}(t=0)\exp[-\lambda_{int}t]. \tag{3.5}$$

Weisskopf Estimates

To compare different transition strength values B, it is useful to normalize them to single-particle (neutron or proton) transitions. The estimate for this, the so-called "Weisskopf estimate" B_W [71] allows to judge on comparably weak or strong character of the transition. For electric transitions it is defined as

$$B_W(E\lambda) = \frac{1}{4\pi}\left(\frac{3}{3+\lambda}\right)^2 (1.2A^{1/3})^{2\lambda} e^2 f m^{2\lambda}, \tag{3.6}$$

and transitions with a strength in the order of one Weisskopf unit (W. u.) can be considered to result from transitions of a few particles only. Conclusively, a transition with strength in the order of >10 W. u. is considered to result from many particles taking part in the transition, and is therefore regarded as collective, cp. section 2.2.

3.2 Coulomb Excitation

One of many ways to excite a nucleus from the ground state into energetically higher-lying levels makes use of the energy-dependence of different interactions by excluding hadronic interaction. As the remaining interaction is purely electromagnetic, this form of excitation is called Coulomb excitation. In the case of two nuclei, this interaction causing the excitation of one or both nuclei, happens by exchange of a virtual photon. The energy threshold E_{CB} for this process, the Coulomb barrier, depends on the masses $A_{1,2}$ and electrical charges $Z_{1,2}$ of the reaction partners 1, 2, and can be denoted as [73]

$$E_{CB} = \frac{e^2}{4\pi\epsilon_0}\frac{Z_1 Z_2}{r_0(A_1+A_2)^{1/3}}, \tag{3.7}$$

with r_0=1.3 fm.

Several conventions exist that define the exclusion of hadronic interaction. One of the easiest to picture is the "Cline criterion" [74], requesting a certain minimum

distance D_{min} between the reaction partners' surfaces, e.g. 5 fm. For the collision process of two particles (projectile and target) this requirement defines a limiting impact parameter $b(E_b, \theta)$, which can be satisfied by the choice of the impact energy E_b and/or the limitation of the scattering angle θ. For better picturing a schematics is depicted in figure 3.2.

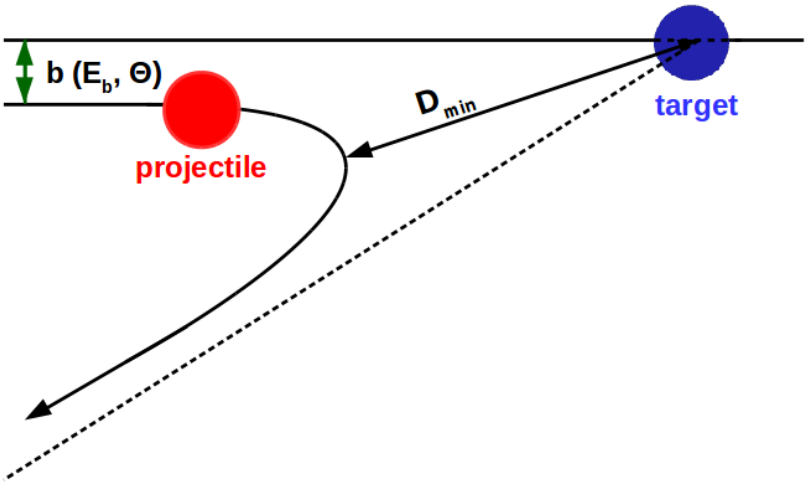

Figure 3.2.: Two-particle scattering process, here for a Coulomb excitation. For the minimum required distance D_{min} between nuclear surfaces set by the Cline criterion, the minimum of the impact parameter $b(E_b, \theta)$ must not be exceeded.

What makes the Coulomb excitation remarkable is the special case of a one-step E2 excitation from the ground state. For that, the cross-section for the excitation is directly depending on the transition strength connecting the two levels. Therefore, measurements of transition strength values or respective level lifetimes can be transferred to measurements of cross-sections, which is sometimes experimentally less challenging. For more details about Coulomb excitation, the reader is referred to the profound work in references [73, 75]. For connection of cross-section and $B(E2)$ transition strength one can derive

$$\sigma_{E2} = \alpha(Z_1, Z_2, v, \mu) B(E2; 0^+_{g.s.} \rightarrow 2^+) \beta(\Delta E), \tag{3.8}$$

where α is a constant depending on the reaction partners' charges, relative velocity v and reduced mass μ , and β is a function decreasing with rising excitation energy. In the general case, the Coulomb excitation cross-section is a result of many single processes with multiple parameters. Calculations of those cross-sections therefore have to employ computer algorithms. Some popular ones are CLX [76] and GOSIA [77, 78].

It is worth noting that by the nature of the excitation process (virtual photon exchange) the cross-sections for electric transitions of low multipole order are favoured compared to magnetic transitions of the same order, and higher multipole orders are suppressed as compared to lower ones.

4 Experimental Methods

Having introduced the theoretical model approach that strives to describe nuclear structure (cp. chapter 2) and having repeated the basic physics principles (cp. chapter 3) that define observables as measure for the theories, in this section the background of this work is concluded with the experimental methods used. The application of the presented experimental techniques is the measurement of energies and times connected with nuclear structure, i.e., nuclear transition energies and level lifetimes. Since those methods have been developed and applied over a historical time period of many decades, the following summary cannot claim to include every detail about them. Instead it focuses on the principles only. Further information can be found in the usual specialist literature dealing with this topic (e.g. [79]).

The application of the experimental methods is first and foremost limited by the value range of the observables to be measured and the instruments available for that. In particular, when it comes to precision and limits, strong developments have been achieved in instrumental capabilities [80]. The equipment employed in this work will be presented in the chapters 5.1, 5.2, where the respective experiments are covered. It is worth mentioning that the results obtained in this work would not be possible to obtain without the used state-of-the art equipment.

Considering the ranges of energies and level lifetimes relevant for nuclear structure studies, typical γ-transition energies average in the order of 50 keV to some MeV. This range of $\sim$two orders of magnitude can all be covered by the means of γ-ray spectroscopy. Due to its rather basic physics nature, regarding the topic of γ-ray spectroscopy the reader is referred to general literature on this subject [81, 82], and specific publications of state-of-the-art developments as reviewed in [80].

The case is different when level lifetimes are regarded: Since short-lived levels can go down to some femtoseconds (10^{-15} s) while long-lived isomeric states range at some milliseconds (10^{-3} s), to cover the whole scale of observable lifetimes of $\sim$12 orders of magnitude requires specific range-dependent techniques. The established techniques to tackle lifetime measurements at different time ranges are presented in the following. Note, that times (and their differences) can be measured by the same equipment as used for γ-ray spectroscopy. However, good time resolution and good energy resolution at the same time are hard to achieve within one detector material [81], and the combination of detectors has to be chosen according to the subject of measurement.

4.1 Measurement of Nuclear Level Lifetimes

The classical approach to measuring times in general is based on the comparison of the time difference between an event starting and its ending with a clock. While the replacement of a classical mechanical clock to electronic timing increases the precision of the measured time, when going down to lower time magnitudes the timing capabilities of the used electronics eventually come to an end. With the current possibilities this is reached at a time scale of some tens of picoseconds [83, 84]. When faster nuclear level decays become the subject of interest, timing alone does not suffice and measuring other observables followed by dedicated analysis to deduce correlated lifetimes is required. As was already described in the previous section 3.2 indirect approaches as the Coulomb excitation can be applied here. Another successfully-employed indirect method for deduction of smaller lifetimes is the Nuclear Resonance Fluoroscence (NRF) method: Here, the lifetime is deduced from the direct relation of lifetimes to γ-decay widths as defined by the equation $\tau = \frac{\hbar}{\Gamma}$ [85].
Regarding direct methods for measurements of smaller nuclear level lifetimes, the measurement of γ-ray energies at flight is employed to relate decays in flight at relativistic velocities to lifetimes by the observed energy shift. Since the decay energy of emitted γ-rays is observed depending on the relative velocity between emitter and observer, the decaying nucleus' state of motion directly affects the respective energy. This shift is the so-called Doppler-shift [86], and it allows to apply the tools of γ spectroscopy to obtain nuclear lifetimes by means of two distinct techniques: the Doppler Shift Attenuation Method (DSAM), and the Recoil Distance Doppler Shift (RDDS).

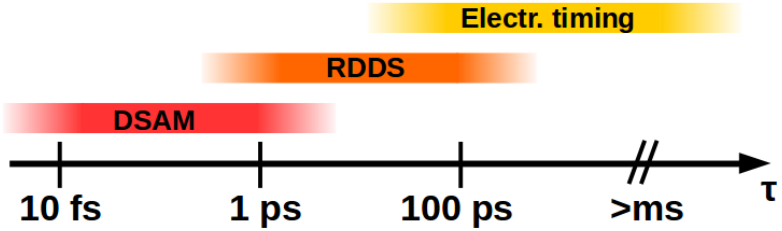

Figure 4.1.: Methods for the experimental access to nuclear level lifetimes and the time range for their application. Note, that the transitions are overlapping, rather soft, and a subject to technical developments.

Figure 4.1 depicts the time scale of nuclear level lifetimes, and the three applicable techniques (electr. timing, RDDS, and DSAM) for direct measurements. In the following, these techniques are described.

4.1.1 Electronic Timing

The electronic timing is the oldest approach to lifetime measurements. It combines the simple principle of a mechanical stop clock with the improved timing capabilities of electronics. For this, a trigger signal corresponding to the population of the level of interest, e.g. a γ decay into this level, starts the clock. The stop signal is then provided by the de-population of the regarded level. This principle is depicted in figure 4.2 for a β-decay population and a Time-to-Amplitude-Converter (TAC) to convert the time difference into a digital signal with a proportionally high amplitude.

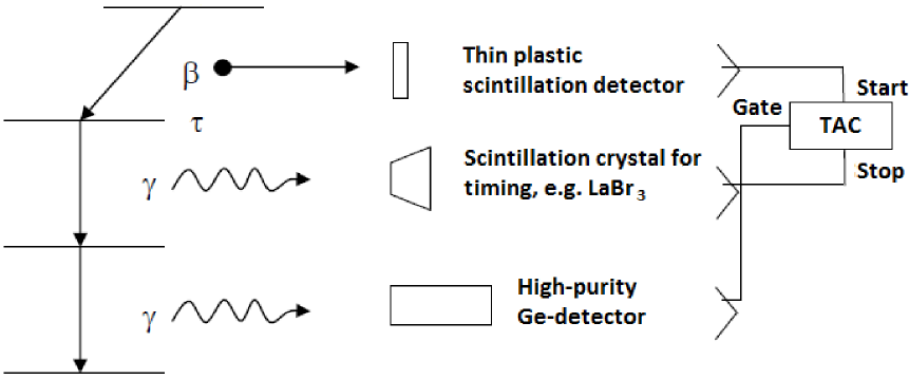

Figure 4.2.: Schematics of the method used for lifetime measurement by electronic timing: The level of interest is populated with a β-decay (can be different), which triggers the start signal of the TAC. The stop signal is provided by the de-excitation of the decaying state resulting in a time difference measured. Additional Ge detectors can optionally be used to provide a better energy resolution. Figure taken from [87].

By working principle, the limiting factor for the time resolution of electronic timing is the detector's timing capability. Using a fast scintillating material (e.g. plastics), the measurable time can be pushed down to few picoseconds. Since fast-timing

detector material happens to have a comparably bad energy resolution, for disentangling different energetically-close lying γ rays an experimental setup can be expanded by e.g. Ge-detectors with a relatively good energy resolution. Coincident conditions can then be used to differentiate contaminating decays and/or better identification by coincidence conditions (gates) on decay cascades.
Provided sufficient statistics, recent analysis methods allow to reduce the observed times beyond the detector's resolution. Prime examples are the decay curve, or the centroid shift method [88] making use of the characteristic time distributions following a nuclear level decay. Also of recent interest for the improvement of this method is the development of fast-sampling digitizers that increases the timing capabilities by directly digitizing and processing the measured signals [89]. The limit for the lowest lifetimes measurable with this technique is claimed to be in the range of some picoseconds [90, 91].

4.1.2 Recoil Distance Doppler Shift

As suggested by the naming, Recoil Distance Doppler Shift, the RDDS method makes use of the relativistic Doppler shift of γ-ray energies emitted in flight at relativistic velocities. The typical expression for the decay of the level of interest (cp. chapter 3) is extended to include decays at flight (at velocity β) and at rest [92]

$$\frac{A_{flight}}{A_{rest}+A_{flight}} = \exp\left[\frac{x}{\beta c\tau}\right] \tag{4.1}$$

This is achieved by populating the nuclear level of interest by a reaction in a target material at the time $t=0$, after which the excited particle is in flight with velocity v, cp. figure 4.3. Decays happening during this stage (within its flight time t_f) take place in motion and, thus, are subject to the Doppler shift. Stopping the particle after a certain flight distance x (at time $t = t_f$) ensures the decays happening after that to take place at rest. Thus, for them no Doppler shift is observed. The comparison of decay intensities at rest A_{rest} (after $t = t_r$) and in flight A_{flight} (during t_f) then directly yields a function of the level lifetime to be measured. The experimental implementation of this principle is sketched in figure 4.3.
Lifetimes measured by this technique can be as low as ∼one picosecond, which is due to the minimal separation distance accurately achievable between the target and the stopper (some micrometers). For precision of the lifetimes measured in this way, this distance has to be known precisely. Therefore, and since the range of target-stopper distances, which is sensitive to the lifetime, is limited, a typical RDDS measurement takes place at multiple consecutive distances. This ensures a

statistical average of the decay component ratios. If the level of interest is populated by other decaying levels, this so-called feeding can be accounted for by the use of the Bateman equations (cp. section 3.1).
An extension of the RDDS principle worth mentioning, the differential decay curve method (DDCM) [93], allows for suppression of systematic errors and reduces the amount of required measurement distances for precise lifetime determination. However, its application comes with the requirement for high coincidence statistics, which limits its use for low-rate experiments.

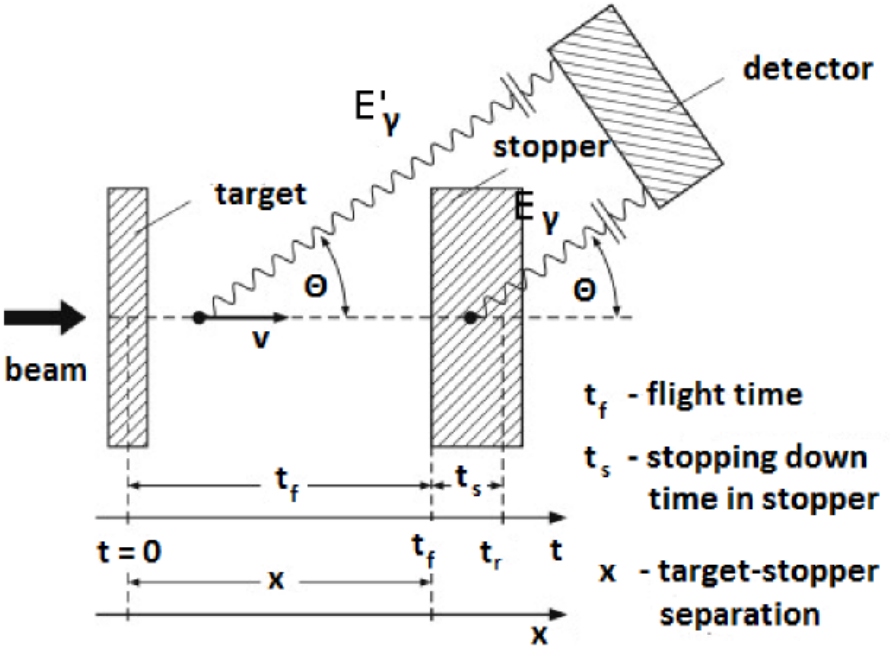

Figure 4.3.: Simple methodical principle of the RDDS method: The level with lifetime to be measured is populated within a particle in the excitation target (t=0). It decays at relativistic velocities v during its flight until it is stopped (t_f). After that (t_r) decays happen at rest. All decays are measured by detectors surrounding the setup. Here, one is positioned at forward angles Θ. For detail refer to the text. Figure taken from [92].

4.1.3 Doppler Shift Attenuation Method

The lifetime measurement of shorter-lived nuclear levels is achievable by an expansion of the principle already introduced in the RDDS method. While for the RDDS technique decays at two states of motion, in flight and at rest, are regarded, the observance of decays at all velocities between the excitation and the full stop holds additional information about the lifetime of the involved levels. This is the basis of the Doppler shift attenuation method (DSAM) [79, 94]. Instead of varying the distance between the excitation target and a stopper, both layers are directly connected (can even be the same). This ensures the start of the stopping process directly after the population of the level of interest. γ rays emitted during this stopping process contribute to a Doppler-shifted energy distribution depending on the particle's decreasing velocity. The result is a shape measured in the γ-ray spectrum with energies between the one corresponding to decays at rest and the one corresponding to the maximum velocity after excitation. This so-called lineshape is sensitive to the velocity distribution of the particle, and thus the stopping process, and more importantly to the lifetime of the decaying level(s). The stopping process needs to be simulated taking into account electronic and nuclear stopping. Then the lifetime is the only remaining parameter of a functional fit to this lineshape. The composition of the lineshape as sum of contributions from decays at different velocities is depicted in figure 4.4 for a detector at forward angles.
The lower lifetime limit accessible by this method is correlated to the time needed to stop the particle in the stopper, which is in the order of some femtoseconds for usual particle-stopper combinations. This marks the lowest scale of lifetimes directly measurable by experiment. Also the accuracy of the obtained results depends strongly on the knowledge of the stopping process. For this reason a systematic uncertainty of $\sim$10% usually cannot be avoided [96], which is directly linked to the uncertainties of the stopping powers.
Some (recent) developments improve the quality of DSAM measurements. Examples worth noting are the differential DSAM and the continuous angle DSAM (caDSAM) [95]. In the former the excited particle is only partially stopped, and therefore can be detected after the transition through the stopper. This allows for conditional correlations to clean up the obtained spectrum, e.g. in the case of strong background contributions. On the other hand, caDSAM makes use of state-of-the art detector arrays with a large continuous solid angle coverage. This allows to take the detectors' angles into account and produce a three-dimensional lineshape to separate angle-dependent contributions to the lineshape.

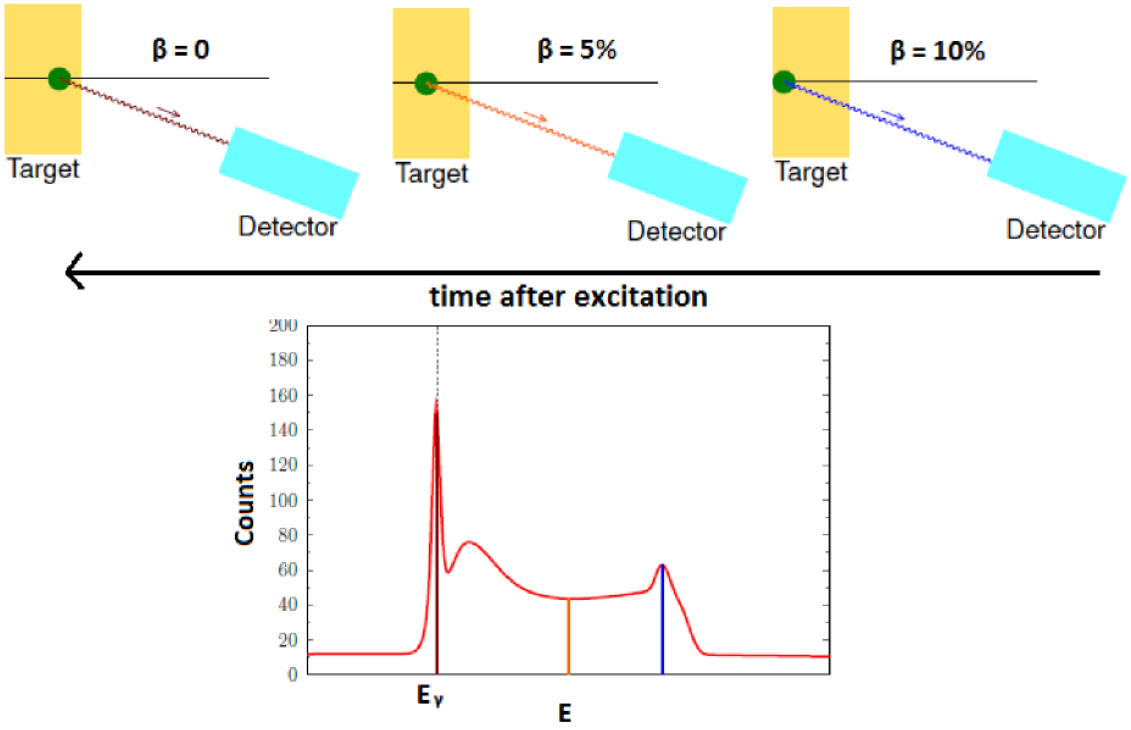

Figure 4.4.: Principle of the Doppler shift attenuation method: decays at different velocities result in a different Doppler-shift in energy. The resulting lineshape is sensitive to the involved lifetime(s). Figure taken from [95].

5 Experiments and Analysis

As has been motivated in section 1.1, the nucleus ^{98}Zr plays a pivotal role in understanding the phenomena of shell evolution and shape coexistence (cp. section 2.3) in the Zr isotopic chain. An experimental determination of its $B(E2; 2_1^+ \rightarrow 0_1^+)$ transition strength, equivalent to the determination of the respective level lifetime, is crucial for clarity in this physics case. It is this task that is tackled within the mainframe of this work. The experimental approach and the consequent analysis of the obtained data are presented in this chapter.

With ^{98}Zr representing an unstable nucleus, i.e., β^--decaying into ^{98}Nb with a rather short half-life $T_{1/2}$ of 30.7 s [16, 27], the use of naturally-available material is excluded. Therefore, its production is the first experimental challenge. While this is within the realm of possibilities of RIB facilities [97, 98] by means of, e.g. fusion(-fission) [99] or deep-inelastic scattering [100, 101] production mechanisms, its location in terms of nucleon numbers close to medium-mass stable nuclei in the nuclear chart allows different mechanisms to be taken into account for its production.
The small difference of one neutron pair to the closest stable Zr isotope ^{96}Zr makes the transfer of two neutrons, a production mechanism recently employed to great success in other experiments [102, 103, 104], a suitable option. For the transferred neutrons can stem from stable low-mass ion beams, all the benefits of stable beams apply; i.e., nearly absolute purity, high particle rates and good beam energy control. However, with the low natural abundance of 2.8% [16] for ^{96}Zr, which forms the base for this reaction, a slight drawback of this method is apparent.
Unstable medium-mass nuclei, such as ^{98}Zr, are also produced in the well-studied fission of high-mass nuclei. Compared to fusion-fission and deep-inelastic reactions the distribution of produced radioactive isotopes here peaks at the two distinct mass regions of the binary-reaction partners. Although not all nuclei can be accessed with spontaneous fission, for nuclei close to those product distribution maximums, comparably high production rates can be achieved [15]. However, the separation of unwanted fission products, and, thus the ion beam purity, becomes the main challenge for such experiments. With selection and charge breeding of nuclei of interest before acceleration leaving them in their ground or isomeric excited state, an additional excitation process after acceleration becomes essential for

nuclear structure studies.
Both the excitation of states and the aim of transition strength determination between levels in ^{98}Zr can be addressed by employing Coulomb excitation (cp. section 3.2) following fission. The prerequisite, a comparably high strength for the transition of interest, can be estimated from the systematic development of $B(E2; 2_1^+ \rightarrow 0_1^+)$ values in the Zr isotopes. On the other hand, the same systematics point to an expected range of the lifetimes to be measured. From this the applicability of the RDDS technique (cp. section 4.1) in this case is suggestive.
To achieve the set goal of lifetime/transition strength measurement of the 2_1^+ state of ^{98}Zr, the above mentioned considerations culminated in two experiments, which will be elaborated on in the following sections: a Coulomb excitation experiment of a radioactive ^{98}Zr ion beam produced by spontaneous fission (section 5.1), and an RDDS experiment of ^{98}Zr after two-neutron transfer to ^{96}Zr from a stable ^{18}O ion beam (section 5.2).
It is worth noting that while the results of both conducted experiments respectively can stand on their own feet, the combination of two completely independent experimental methods and setups, highly increases the reliability of the achieved combined result.

5.1 Coulomb Excitation of Radioactive ^{98}Zr Ion Beam at ANL

To study the $B(E2; 2_1^+ \rightarrow 0_1^+)$ transition strength of ^{98}Zr the first experiment conducted in the course of this work was performed in March 2015 at the ATLAS facility [106] (cp. figure 5.1) of the Argonne National Laboratory (ANL) [107]. It employed the Coulomb excitation of a radioactive ^{98}Zr ion beam on a ^{196}Pt excitation target (inverse kinematics as demonstrated in [108]) to obtain Coulomb-excitation cross sections, which transferred to transition strength values of the beam ions relative to the target excitation.
The production of ^{98}Zr with other radioactive ions was achieved by spontaneous fission of a ^{252}Cf source with a nominal activity of 37 GBq (1 Ci). For the extraction of the nuclei of interest the CARIBU [109, 110](cp. figure 5.2) source was utilized. Therefore, after thermalisation, achieved by the ions' passage through a series of degrader foils, the fission fragments were caught in an admixture of gases, the so-called gas catcher. Here, the ions were electron-stripped to an H-like (1^+) charge state. Sequentially, a first isobaric separation of nuclei was performed before they were charge-bred in the ECR ion source. After injection into the ATLAS superconducting linear accelerator, the ion composition was accelerated to a final energy of 464 MeV. Employing the beam ions' deflection sensitivity to magnetic fields, an isobaric $A = 98$ selection by magnetic rigidity was performed. The product

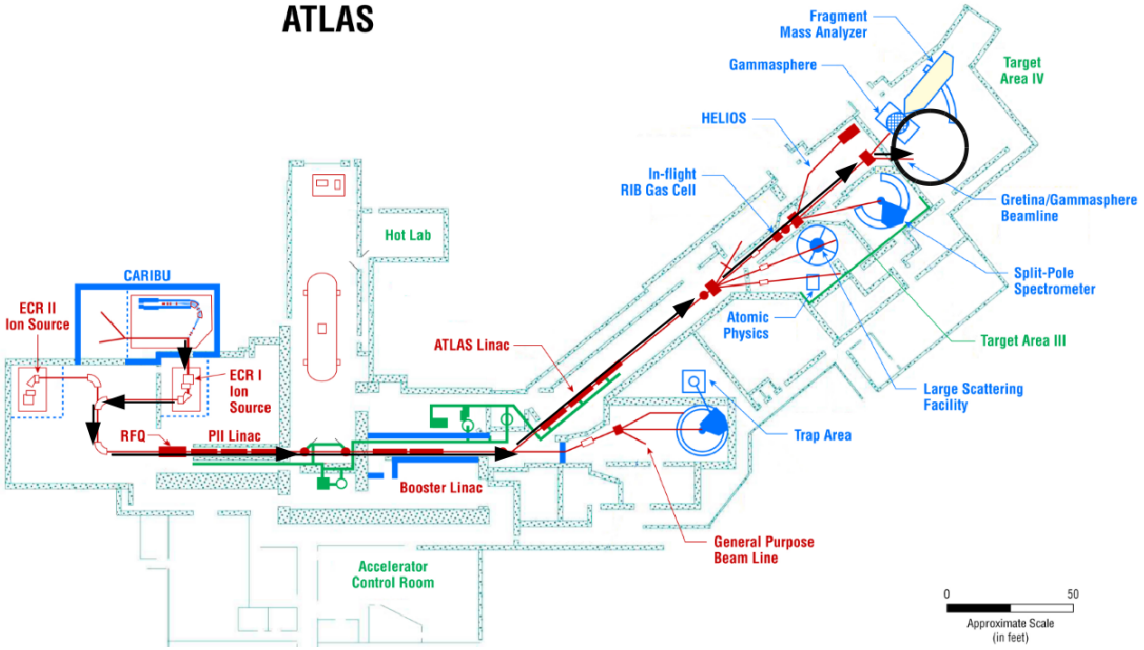

Figure 5.1.: Schematic layout of the ATLAS facility at ANL, at which the experiment was performed. Additionally, the passage of the ions through the beamline and the location of the experimental measurements are depicted in black (arrows and circle). Figure taken from [105].

was a beam consisting of ^{98}Zr and its isobars from the radioactive ^{98}Sr to the stable ^{98}Mo. The exact beam composition is elaborated in the analysis in section 5.1.3.

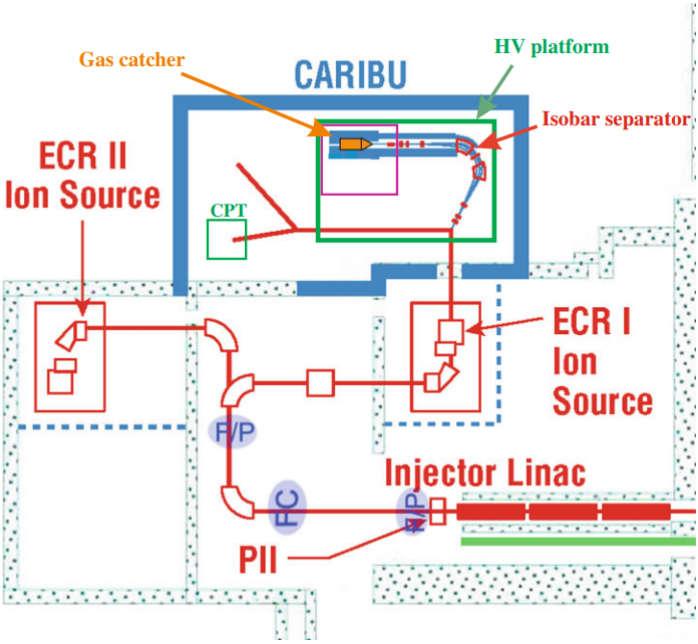

Figure 5.2.: Schematic layout of the CARIBU source used to extract ^{98}Zr ions after ^{252}Cf fission. Figure taken from [110].

The composition of accelerated ions impinged on a ^{196}Pt target with a thickness of 1.59 mg/cm^2. Simultaneously, the target and beam ions were Coulomb-excited. The selected excitation target thickness allowed the beam-like and target-like ions to pass the target material. Those particles were then detected within CHICO2 (cp. section 5.1.1) and this was made use of for the ion selection and the kinematics reconstruction in the analysis (cp. section 5.1.2). The scattering angles covered with CHICO2 influenced the beam energy choice, as the combination of scattering angles and energy were chosen to account for the safe Coulomb excitation criterion (cp. section 3.2). γ-rays emitted in flight by de-excitations of beam- and target-like ions were detected with the GRETINA spectrometer (cp. section 5.1.1).

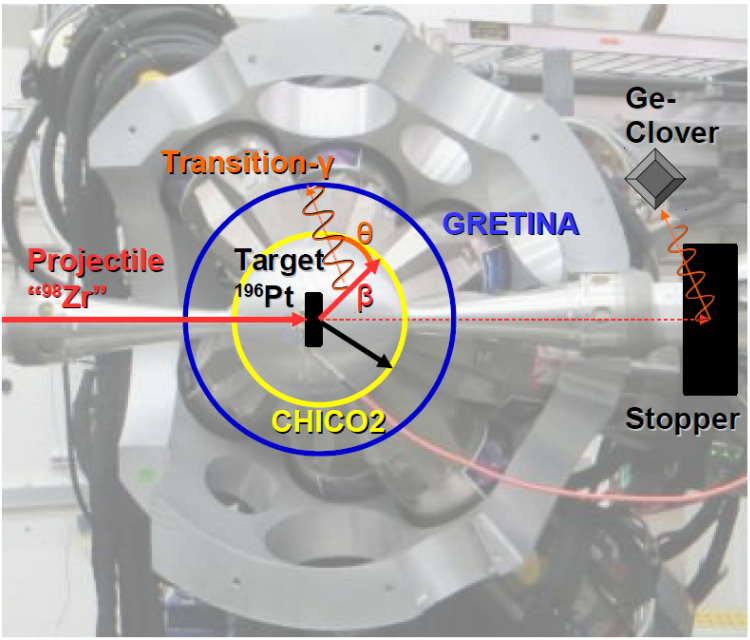

Figure 5.3.: Schema of the experimental setup. Particles following the reaction in the target are detected with CHICO2, and their de-excitation γ radiation with GRETINA. De-excitations of the stopped beam ions are measured with a HPGe-clover detector ∼2 m downstream at the beam stop (only symbolically depicted in the figure).

Finally, the unreacted beam ions were stopped in a solid Al block about 2 m downstream of the target, and their de-excitation γ-rays were detected with a HPGe-clover detector (cp. section 5.1.1) for determination of the beam composition in terms of included isotopes and their respective intensities. A schematic depiction of the experimental setup comprising the mentioned equipment is shown in figure 5.3.
In the following two subsections first the employed experimental equipment, and then the preparation and combination of the obtained data are addressed.

5.1.1 Experimental Equipment

The aims to achieve with the employed detectors of this experiment were two-fold: first, obtaining a γ-ray spectrum of the transitions in ^{98}Zr, and second, obtaining

the isobaric composition of the ion beam. For the first goal the combination of GRETINA (high-resolution γ-ray spectroscopy) and CHICO2 (particle detection) were used. The information obtained with CHICO2 allowed to set a condition for GRETINA based on beam-like ($A = 98$) or target-like ($A = 196$) ions. Also, by correlating the position of detected particles with the γ-rays of their de-excitations, a Doppler-shift correction of the γ-ray energy could be performed. Note that here, as the γ-rays were emitted by ions in flight at relativistic velocities, a Doppler correction is essential for precise and correct transition energy information. On an additional level of interest, the beam composition determined by the use of the HPGe-clover detector, was required for a Coulomb excitation analysis for transition strength measurements.
Brief introductions to GRETINA, CHICO2, and the beam stop HPGe-clover are given below, including characteristics relevant for the experiment. For technical details and other applications of said detectors the interested reader is encouraged to study the given references and, e.g., [111, 112].

GRETINA

The Gamma Ray Energy Tracking Array GRETINA is the spectrometer of choice for the γ-rays measured in this experiment. In its implemented configuration it consists of seven quad-detectors, each composed of four encapsulated and electronically 36-way segmented HPGe crystals within one cryostat. The geometrical arrangement of the quad-detectors is spherically close-packed around the (here: excitation-) target chamber covering a solid angle of roughly 1π with the active area of the detectors; hence, it is referred to as the 1π-configuration [113]. A total efficiency for γ-ray detection of ϵ_γ=6.5 % and an average energy resolution of 2.22 keV (FWHM) at 1.3 MeV is achievable [113] for source γ radiation; for Doppler-shifted γ decays (at velocities $v/c \leq$40%) an energy resolution of $\Delta E/E \leq$1% is attainable [114]. The high efficiency and energy resolution after Doppler-correction exceed those of other comparable spectrometers [115, 116]. It has to be mentioned that the main purpose of the development of γ-ray tracking arrays, such as GRETINA, in general, is the precise locating and sequencing of γ-ray interaction points within the detector, for Compton suppression and use of sum-up events, for increased peak-to-total ratios. However, in this experiment no tracking was used. Reason being mainly that reliable tracking algorithms are still in development. Instead, the complimentary use of CHICO2 allowed for the required interaction point position resolution. The interaction point with highest γ-ray energy deposition in the Germanium was assumed to be the first interaction of the event. This is known to be valid for the energies of interest here, and, hence, sufficiently accurate.

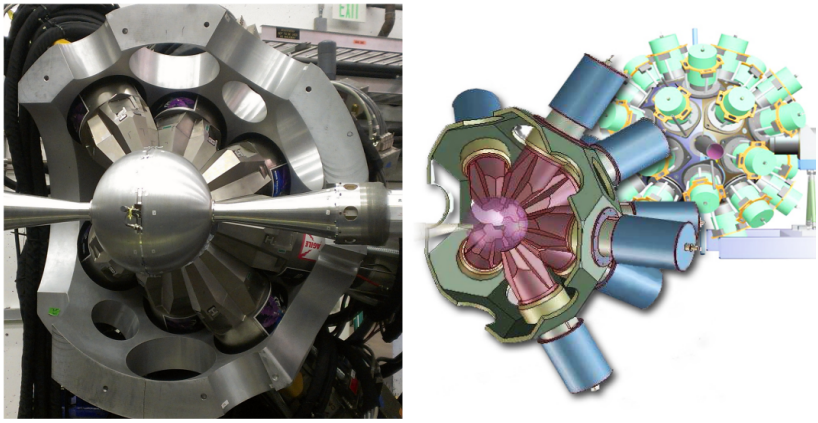

Figure 5.4.: Left-hand side: the Germanium array GRETINA in its 1π-configuration as used in the experiment for γ-ray spectroscopy. Also shown in the foreground is the closed shell of CHICO2 that allowed the detection of outgoing particles. Right-hand side: CAD model schematics of GRETINA in the 1π-configuration (foreground) and an envisioned array of the same detectors with total solid angle coverage of 4π (GRETA); figure from [117].

CHICO2

The Compact Heavy-Ion COunter CHICO2 [118] is an auxiliary charged-particle detector. It consists of two hemispherically-arranged, forward and backward shells incorporating ten position-sensitive PPACs (Parallel Plate Avalanche Counters) each with a total detection coverage of 69% of 4π; i.e., $12\,^{\circ} \leq \theta \leq 85\,^{\circ}$ for forward angle scattering. An overview on a modern PPAC application is given in [119]. The pixelation of both the anode and cathode plates allows for two-dimensional measurement in azimuthal and polar angle with a resolution of 1° and a time resolution of $\Delta t \leq 500$ ps. In this experiment CHICO2 was employed to detect out-going charged-particles following the beam ions' reaction with the excitation target. Hence, scattered and excited target-like and beam-like ions and their respective scattering angles were measured. In this way the two-body scattering kinematics (cp. section 5.1.2) was determined, and, making use of the time signals in the PPACs, employed for discrimination of the ion mass ($A = 196$ for target-like and $A = 98$ for beam-like ions). The acquired scattering angles were transformed

to velocities of the reaction partners and correlated to the de-excitation γ-rays detected in GRETINA for the Doppler-correction of their energies.

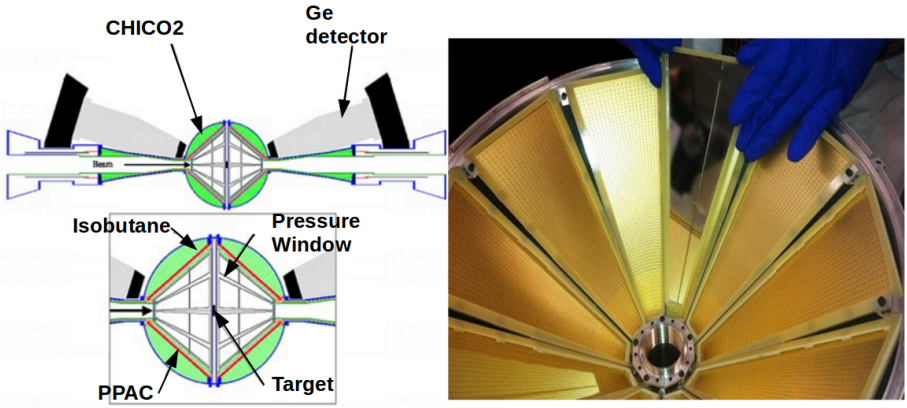

Figure 5.5.: Schematic of the CHICO2 particle detector array (left-hand side), and mounting of the PPACS onto the frame (right-hand side). Figures taken from [120] with slight modifications of the labels.

Beam Stop Ge-Detector

The unscattered ion beam was stopped in a 49.7 mg/cm^2 block made of ^{27}Al $\sim$2 m downstream of the excitation target. A single HPGe clover with no further specifications was placed close to this beam stop and measured γ-rays following de-excitations of the unreacted ion beam components with an absolute detection efficiency of ε_γ=0.2% at 1 MeV energy. The energy resolution can be assumed to be comparable to other HPGe detectors and therefore sufficient here. The γ spectroscopy at the beam stop made possible the unique identification of decaying nuclei composing the ion beam and their respective intensities. The resulting beam composition played an important role in the analysis (cp. section 5.1.3).

5.1.2 Data Preparation and Spectra

In this section the experimental procedure following the data acquisition with above described equipment is specified. The steps elaborated on are the proper calibration of the detectors, the combination of the data and the resulting Doppler

correction of measured γ-ray energies, as well as the beam composition determination. The obtained results (γ-ray spectra and beam intensities) of this first analysis step serve as input for the following Coulomb-excitation analysis, which is the main part of the work related to this experiment. Note, that as the described procedures in large part are standardized and applied in many previous experiments, the description will make use of examples for clarification.

HPGe Detector Energy and Efficiency Calibrations

A standard process, and often one of the first steps of experimental data evaluation, is the calibration of the used equipment; i.e., the normalization of measured signals to known quantities. Within the here used γ-ray spectroscopy, these quantities are γ-ray energies and their (relative) intensities, and the respective energy and efficiency calibrations. For this the use of available source material with known transition energies and intensities (e.g. tabulated in [16]) is common practice.
For the calibration of GRETINA and the beam stop HPGe detector ^{152}Eu, ^{137}Cs, and ^{60}Co isotopes were placed at the excitation target and beam stop (including the Al stopper) positions, respectively. The detector channels corresponding to the deposited γ-ray energies E_γ were adjusted to match those by a linear regression fit of observed channel numbers to the energy values, covering a range from 0 up to 1.5 MeV. The detection efficiency $\varepsilon_\gamma(E_\gamma)$ was calibrated by integrating transition peak areas A_γ of observed transitions and matching them to tabulated relative intensities I_γ with a function of the form given in equation 5.1.

$$\varepsilon_\gamma(E_\gamma) = p_0 + p_1 \frac{A_\gamma}{I_\gamma} + p_2 \left(\frac{A_\gamma}{I_\gamma}\right)^2 + p_3 \left(\frac{A_\gamma}{I_\gamma}\right)^3 \tag{5.1}$$

An exemplary $\varepsilon_\gamma(E_\gamma)$ efficiency curve is shown in figure 5.6 for the HPGe beam-stop detector. The shape of the efficiency curve is influenced by the material between the source and the detector.
Following the above described procedures, the Ge detectors; i.e., every single GRETINA crystal, and the beam stop detector, were calibrated regarding their energy and efficiency.

CHICO2 Kinematics Reconstruction and Reaction Partner Identification

Both the mass and the velocity of the charged particles measured with CHICO2 are important for the data analysis: The mass is used for separation of the particles,

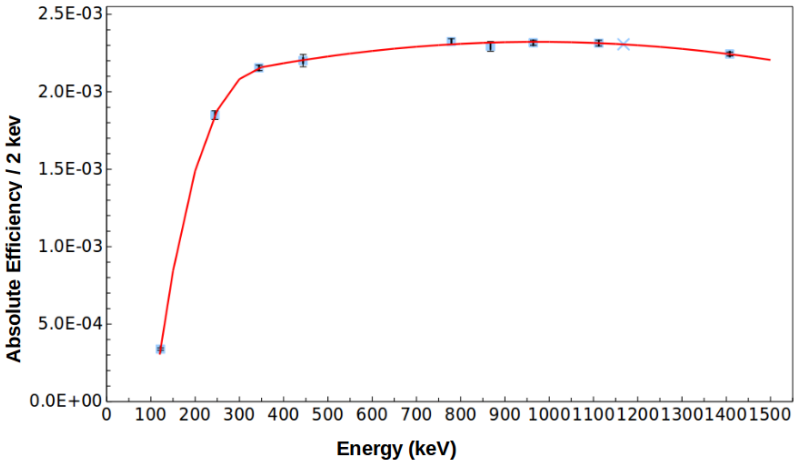

Figure 5.6.: Efficiency curve fitting known intensities of ^{152}Eu at known energies to integrated transition peak areas yielding an absolute efficiency calibration of the detector. Here, for instance, performed for the beam stop HPGe detector.

while the velocities are relevant for the Doppler-shifted energies of de-excitation γ-rays. The position-sensitive detection of out-going charged particles in CHICO2 determines the scattering angle of both beam- and target-like reaction partners. This uniquely fixes all properties of the well-known two-body scattering kinematics 5.2. As can be derived [86] making use of energy and momentum conservation the following relation holds for the velocity v_p of scattered projectiles:

$$\beta_p = \frac{v_p}{c} = \sqrt{1 - \sqrt{\left(\frac{A_t}{A_t + A_p}\right)^2 [1 + \tau^2 + 2\tau\cos(\delta)] \frac{E_p - \Delta E\left(1 + \frac{A_t}{A_p}\right)}{m_p} + 1}} \quad (5.2)$$

with

$$\tau = \frac{A_p}{A_t}\sqrt{\frac{E_p}{E_p - \Delta E\left(1 + \frac{A_p}{A_t}\right)}} \quad (5.3)$$

and

$$\delta = \pi - \Theta_t + \arcsin\left[\tau \frac{A_t}{A_p} \sin(\Theta_t)\right], \tag{5.4}$$

where ΔE is the excitation energy and c the velocity of light, and $m_{p,t}$, $A_{p,t}$, $E_{p,t}$ and $\Theta_{p,t}$ the masses, nuclear mass numbers, kinetic energies and scattering angles of respective projectile-like p and target-like t reaction partners. This kinematic relation is depicted in figure 5.7 for the case of the performed experiment, and can as well be used vice versa to obtain the target-like particle's velocity as function of the beam-like particle's scattering angle. The in-this-way obtained velocities serve as input for the Doppler-correction.

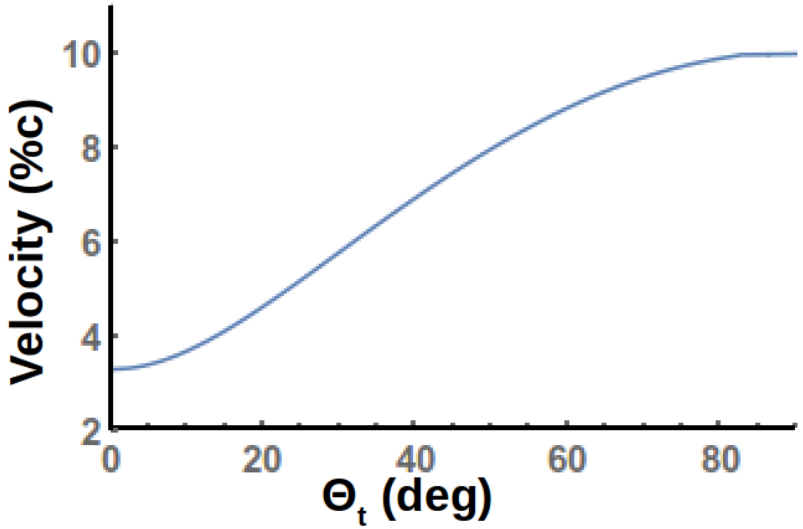

Figure 5.7.: Plot of the two-body kinematics relation between scattering angle of the target ion Θ_t and the velocity of the beam-like ion after the scattering $\beta_p = \frac{v_p}{c}$ for the reaction of ^{98}Zr on ^{196}Pt at an energy of 464 MeV. The excitation of target and beam ions are taken into account up to 4 MeV.

Additionally to the scattering angles, the time information of particle incidents in CHICO2 is employed. As ions of different masses show a different time-of-flight dependence on the scattering angle, the time signals are made use of to separate the reaction partners. Such a selection is depicted in figure 5.8. When coupled to

GRETINA it allows to put a condition on the source of the detected γ-rays in terms of the ion mass.

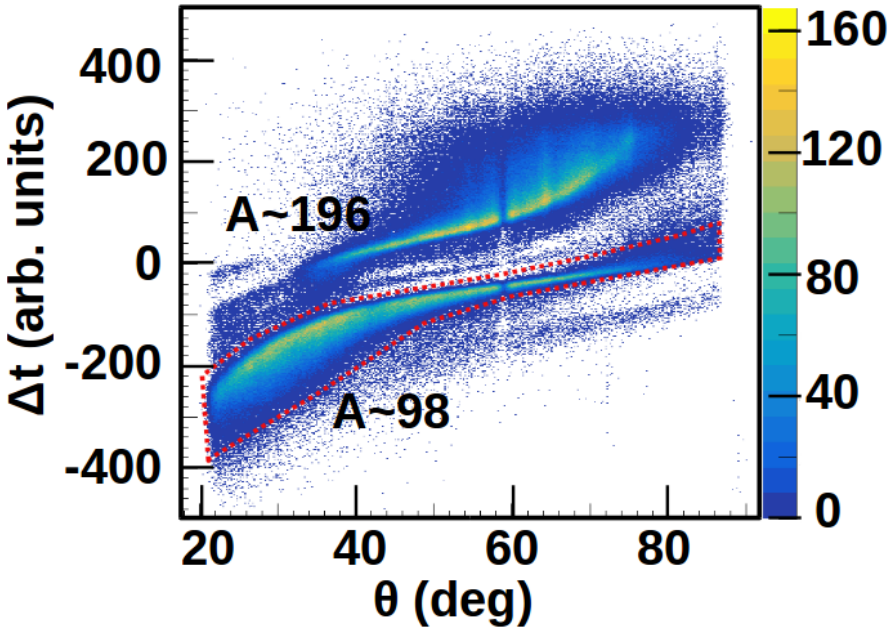

Figure 5.8.: Difference in time of flight between beam and target nuclei at the scattering angle Θ_t measured in CHICO2. A selection of A=98 ions is performed with the condition depicted in dashed red. The other high-statistic distribution above corresponds to A=196 Pt ions.

GRETINA Doppler Correction

Following the kinematics reconstruction, the velocities average at $\beta = \frac{v}{c} \sim 8\%$ for the beam-like ions, and at $\beta \sim 4\%$ for target-like ions. Thus, relativistic effects have to be taken into account. In particular, the γ-rays emitted by those ions in flight are subject to the Doppler effect [86] and consequently show a shift in their energies. Since the performed high-resolution γ-ray spectroscopy requires exactly-measured energy values to a precision of some keV, whereas the energy shift is in the order of tens of keV, the correction of this effect is indispensable. Equation

5.5 describes the relation between the shifted E'_γ and unshifted E_γ energies in dependence on the angle α between the direction of motion of the emitting ion and the detector's direction. Taking coincident particle scattering angles and velocities determined with CHICO2 the rest energy can be calculated this way event by event.

$$E'_\gamma = E_\gamma \frac{\sqrt{1+\beta^2}}{1-\beta\cos\alpha} \tag{5.5}$$

An energy spectrum obtained in GRETINA after performing the Doppler correction for $A = 98$ ions, i.e., beam ions, is shown in figure 5.9. Here, also the effect of the Doppler correction becomes clear: while transition peaks of ^{98}Mo are sharp, their energy-shifed equivalents for ^{196}Pt are smeared out. Note, that for the beam stop Ge detector no such correction is required as the γ-rays measured there are emitted at rest.

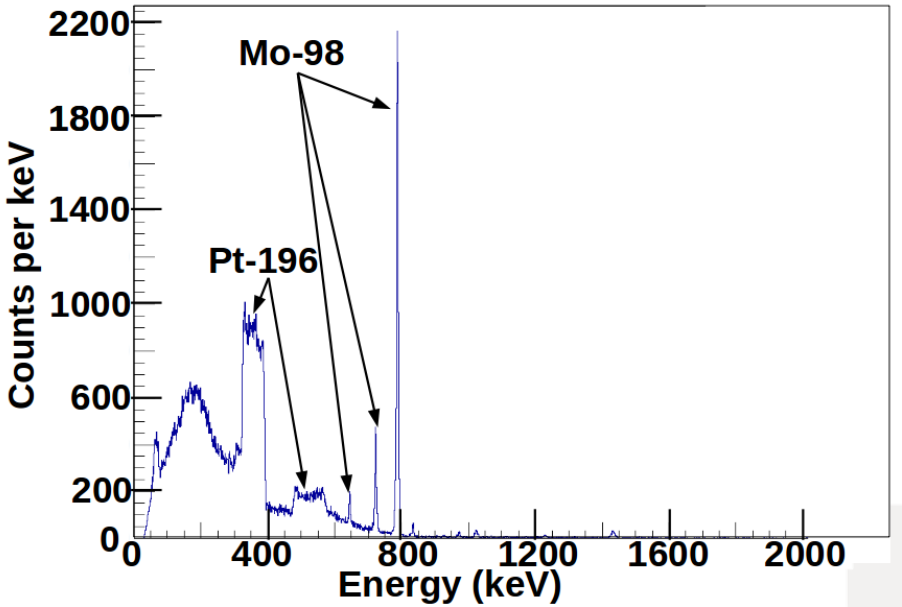

Figure 5.9.: γ-ray energy spectrum detected in GRETINA after application of the Doppler correction for $A = 98$ (beam-like) ions. Note the lack of the correction for transitions of $A = 196$ (target-like, ^{196}Pt) ions.

The result of the Doppler correction is that the measured γ-ray energies are independent of their emitting ion's velocity (corresponding to the scattering angle detected in CHICO2) and the angle between its direction of motion and the detector. This is depicted in figure 5.10 for a correction on $A = 98$ nuclei.

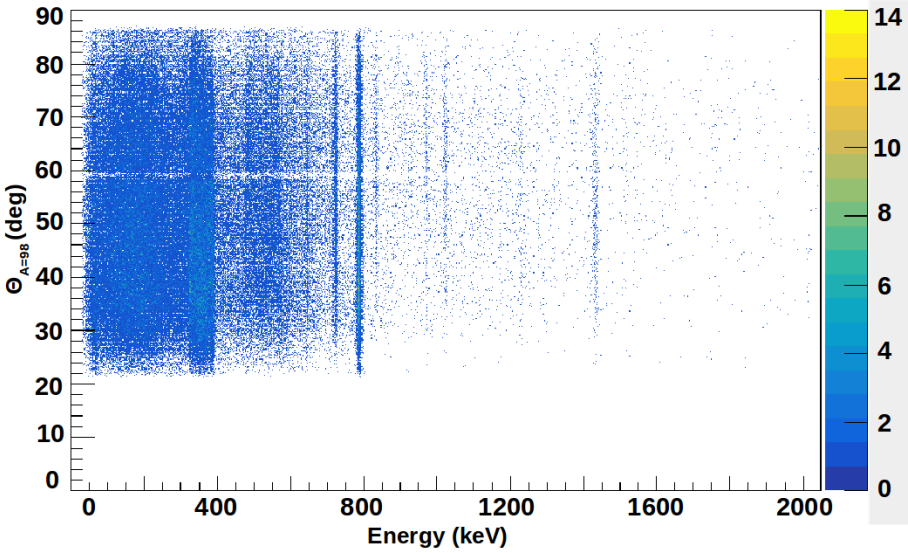

Figure 5.10.: Doppler-corrected γ-ray energies of decays of $A = 98$ nuclei detected in GRETINA over scattering angle measured with CHICO2. Since the scattering angle corresponds to the ion's velocity during emission of the γ-ray, and no dependence exists, the Doppler-correction can be verified.

After this step of the data preparation all relevant information measured with GRETINA and CHICO2 have been combined to result in Doppler-corrected γ-ray spectra with selectable origin. This combination finally allows to determine γ-transition yields of the involved beam and target nuclei in section 5.1.3. The energy resolution after Doppler-correction was achieved to be 6.8(1) keV (FWHM) at 1230 keV. The significant reduction compared to the $\Delta E/E \leq 1\%$ stated in section 5.1.1 is explained by the smaller velocity of the emitting ions.

For technical reasons, the ion beam provided by the ATLAS facility cannot be absolutely purified by magnetic rigidity selection to transmit only nuclei of one specific isotope. The here desired ^{98}Zr is thus only a fraction of the resulting "beam cocktail". Since all other beam components contribute to the excitation of the ^{196}Pt target, the determination of the total beam ingredients and their intensities is therefore a prerequisite for a Coulomb excitation analysis. It is at this point that the HPGe detector at the beam stop comes into play: the γ de-excitations of excited nuclear states following β-decays of nuclei included in the beam permits the quantitative deduction of the beam composition by means of γ-ray spectroscopy. Measuring the beam composition after the reaction target also makes sure to properly account for all ions passing the target as opposed to a beam determination at some point of the acceleration stage, which is prone to changes before the actual reaction.

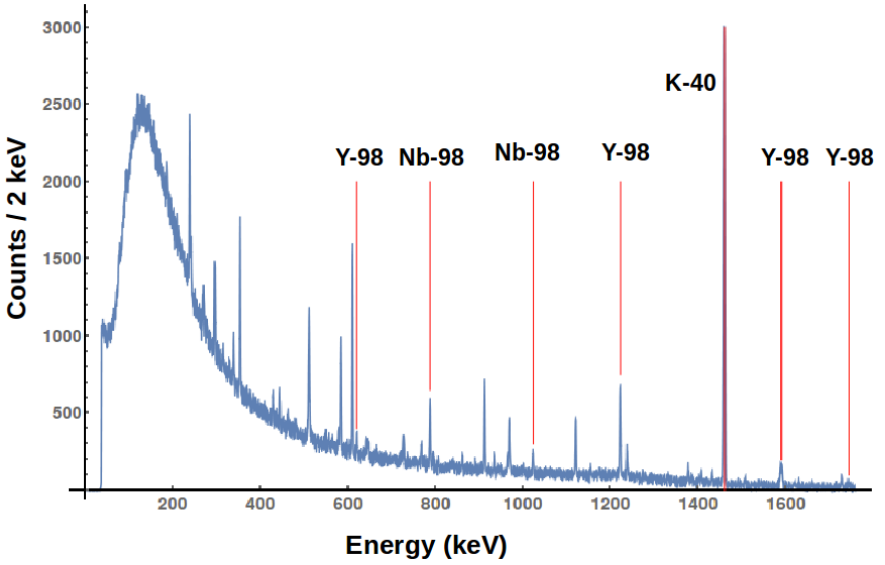

Figure 5.11.: γ-ray energy spectrum measured at the beam stop showing decays of nuclei included in the ion beam.

Table 5.1.: Beam composition as deduced by observed γ-rays following β^--decays at the beam stop and relative yield estimates (normalized to ^{98})Zr according to [122]. Isomeric states are denoted by ^{m}.

Isotope	Intensity (pps)	Intensity estimates [122] (pps)
^{98}Sr	113(9)	98
^{98}Y	159(23)	168
^{98}Y^m	101(20)	176
^{98}Nb	<30	5
^{98}Nb^m	<5	no estimate
^{98}Zr	>162	162 (norm.)

The beam composition analysis is based on the intensities of γ-rays detected by the HPGe detector at the beam stop. A typical spectrum is shown in figure 5.11. The observed transitions can be attributed to nuclei in the $A = 98$ β^--decay chain ^{98}Sr$\rightarrow$ ^{98}Y $\rightarrow$ ^{98}Zr$\rightarrow$ ^{98}Nb$\rightarrow$ ^{98}Mo. Since the relevant energy level schemes, and γ- and β-decay branching ratios are well-known [16, 27], from the observed intensities of γ-ray transitions of ^{98}Y, ^{98}Zr, ^{98}Nb, and (if applicable) their respective isomers the beam composition can be deduced. Additional information is needed to obtain the intensity of ^{98}Zr in the beam as only the sum of ^{98}Nb, ^{98}Nb^m and ^{98}Zr is obtained this way. Since no transitions unique to the decay ^{98}Zr $\rightarrow$ ^{98}Nb are observable (^{98}Zr decays directly to the ground state of ^{98}Nb), the intensity of ^{98}Zr in the beam is related to the intensity of ^{98}Nb and its isomer ^{98}Nb^m with observed decays. Here, the well-studied fission of ^{252}Cf, in particular its yield division [121] of isomeric state to total amount of ^{98}Nb, is employed. As the intensity of ^{98}Nb^m in the beam is comparably small [3(2) pps], which is statistically compatible with zero, it is deduced to be smaller 5 pps, and the upper limit is transferred to the intensity of ^{98}Nb. This results in a lower limit for the intensity of ^{98}Zr in the beam. More details on the beam composition analysis are given in appendix A.1. The total beam composition deduced is tabulated in table 5.1 and is in agreement with relative CARIBU yield estimates [122]. While the extracted intensities show the radioactive composition of the beam, the stable product of the β^--decay chain, ^{98}Mo, was the main contribution of the provided beam.
The deduced minimum intensity of ^{98}Zr>162 pps is used in the following section 5.1.3.

5.1.3 Coulomb Excitation Analysis and Transition Strength Determination

The main aim of the performed experiment; i.e., the extraction of the $B(E2; 2_1^+ \rightarrow 0_1^+)$ transition strength of ^{98}Zr by Coulomb excitation relative to the excitations in the target ^{196}Pt, is performed in two steps: first, analysing the target excitations, and then the excitations of ^{98}Zr. Therefore, the previous steps of the data preparation leading to the obtained γ-ray spectra and the beam composition are employed. Excitations of the ^{196}Pt target were performed by all components of the beam proportional to their respective intensities. Subtracting every contribution to those excitations except ^{98}Zr leaves a yield of target excitations that has to be assigned to stem from reaction with the ^{98}Zr of interest. The corresponding cross-sections and resulting excitations yields were calculated using the computer code CLX [76]. The CLX input files and the details on the calculations can be found in appendix A.2. For quantifying the total of target excitations, the γ-ray spectrum obtained with GRETINA was Doppler-corrected on a mass of $A = 196$. Since the dependence of the target excitation on the charge number Z of the beam nuclei is minor here, it can be neglected in good approximation.

The excitations of ^{98}Zr were measured by the de-excitations of the 2_1^+ state to the ground state at the well-known energy of 1222.3 keV. However, as is depicted in figure 5.12, the $3_1^- \rightarrow 2_1^+$ transition of ^{98}Mo at 1230 keV is decisively dominant in this energy region. Nevertheless, a maximum amount of observed ^{98}Zr transitions can be deduced from the spectrum. For that, analysing the minimum required transition count for a clear identification of a ^{98}Zr transition peak on the background of the ^{98}Mo transition yields a limit. This is performed by fitting a hypothetical ^{98}Zr transition peak to the measured spectrum. A variation of the involved peaks' (both Mo and Zr transitions) FWHM is performed based on the FWHM of other energetically-close lying transitions of ^{98}Mo (cp. figure 5.12). The results of both, best FWHM (smallest χ^2 of the fit procedure) and maximum FWHM, fits simultaneously lead to a maximum value of observed ^{98}Zr $2_1^+ \rightarrow 0_{g.s.}^+$ transitions of 40 counts. A larger yield would have been observed as an additional peak in the energy spectrum.

Combining the Coulomb excitation yields of the ^{196}Pt target stemming from reactions with ^{98}Zr and the value for the maximum transition counts of ^{98}Zr, the Coulomb excitation cross sections, and, thus, the transition strength values can be related to each other (cp. section 3.2). With the limiting value of 40 observed $2_1^+ \rightarrow 0_{g.s.}^+$ transitions this translates to a value of 8.9(20) W. u. for the $B(E2; 2_1^+ \rightarrow 0_{g.s.}^+)$ strength of ^{98}Zr. The main uncertainty here stems from the uncertainties in the beam composition. Including the near-zero lower limit from a previous experiment [28], the B(E2) value can be constrained to 1.83 W. u.$<B(E2; 2_1^+ \rightarrow 0_1^+)<$11 W. u.

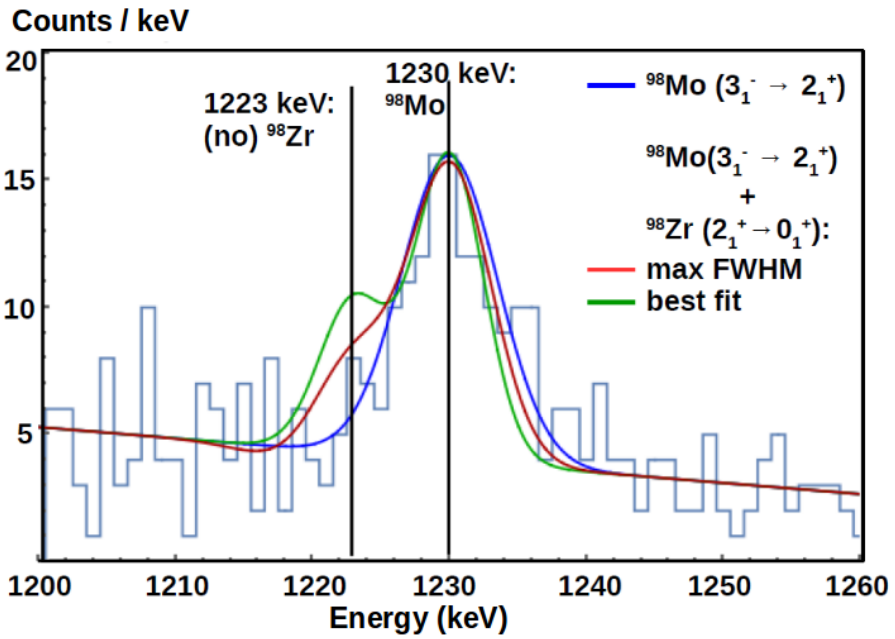

Figure 5.12.: Doppler-corrected energy spectrum obtained with GRETINA summed over all detector angles. Shown in blue (lowest line at 1222 keV) is a fit to solely the $3_1^- \rightarrow 2_1^+$ transition peak of ^{98}Mo at 1230 keV, in red (middle line at 1222 keV) and green (upper line at 1222 keV) hypothetical contributions of the $2_1^+ \rightarrow 0_1^+$ transition of ^{98}Zr at 1222 keV with 40 observed transition counts at the maximum possible FWHM (red, middle line) and best fitted value of the FWHM (green, upper line). See text for further details. Figure taken from [20].

The establishment of this upper limit on the transition strength value constitutes the result of this experiment. Its implications are discussed in section 5.3, together with the second experiment of this work with a similar goal. This second experiment is presented in the following section 5.2.

5.2 RDDS of ^{98}Zr after the ^{96}Zr(^{18}O, ^{16}O)^{98}Zr reaction at IFIN-HH

As was described in section 5.1 the Coulomb excitation experiment performed at ANL succeeded in deducing a decisive upper limit for the observable of this work's

interest, the $B(E2; 2_1^+ \rightarrow 0_1^+)$ transition strength of ^{98}Zr. However, ranging over $\sim$10 W. u., the precision of the extracted value left to be desired. The main reason for the uncertainty was identified to be the impurity of the radioactive ion beam originating from the ^{252}Cf fission; most problematic here: the high intensity ratio of ^{98}Mo to ^{98}Zr overshadowing the Zr transitions in the γ-ray spectrum. Therefore, to improve on the precision of the measured value, a second experiment with the same goal was performed in another fashion.

The general idea of the follow-up experiment utilized the insights of the first experiment, being that a) the production of ^{98}Zr by spontaneous fission is problematic for the set aims, and b) that the lifetime of the $2_1^+ \rightarrow 0_{g.s}^+$ transition can be limited to a range of one to ten picoseconds based on the limits imposed by the B(E2) transition strength bounds. From section 4.1 it can therefore be inferred that the RDDS method is the applicable method for lifetime measurements here. Also suggestive from the method's principle, the excitation (production) of ^{98}Zr has to take place at the location of the measurement, which excludes the use of a radioactive (re-accelerated) ^{98}Zr beam. What can also be excluded is the employment of a ^{98}Zr target as its β^--lifetime is too small (30.7 s [16, 27]) for a longer measurement time. A solution to this problematically-seeming accumulation of restrictions was found to be the neutron-transfer reaction (cp. figure 5.13): For only two neutrons are separating ^{98}Zr from the stable ^{96}Zr, this production mechanism is very viable here. Also as the two neutrons can be transferred from stable beam ions, which yield higher intensities and purity than accelerated radioactive ions [98], the second challenge of the first experiment can be avoided that way.

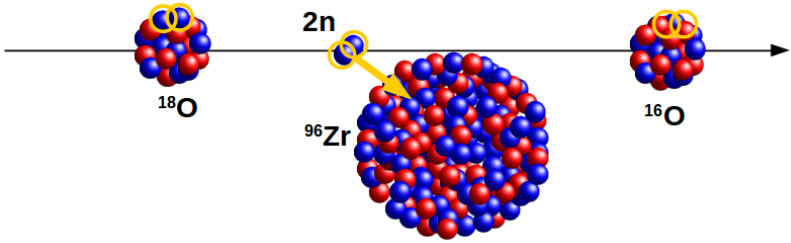

Figure 5.13.: Sketch of the neutron-pair transfer reaction employed as production and excitation mechanism in this experiment. Neutrons are depicted as blue balls (as opposed to red protons) and transferred to the target nucleus. The transferred neutron pair is highlighted in yellow.

Comparable experiments have used the multi-neutron transfer reaction to great success (e.g., [103, 104]) by employing the stable beam accelerated by a tandem accelerator at sub-Coulomb barrier energies. Since the tandem accelerator has been one of the oldest and relatively simple kind of particle accelerators the interested reader is referred to the classical literature (e.g. [86]) for its working principle. The tandem accelerator used for the experiment described in this section was the 9 MV FN Pelletron tandem accelerator of IFIN-HH [123, 124], as shown in figure 5.14. It provides a comparably high ^{18}O beam intensity and energy and, with an average run time of 5500 hours per year, works very reliably.

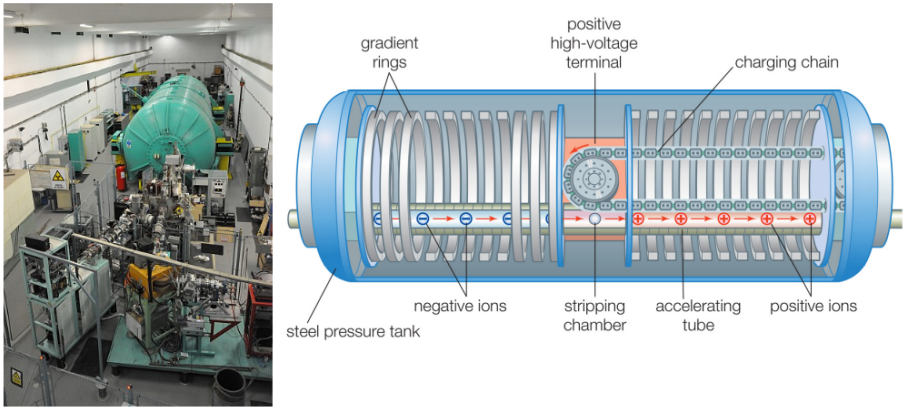

Figure 5.14.: Left-hand side: the IFIN-HH 9 MV FN Pelletron tandem accelerator, which was used to accelerate ^{18}O ions in this experiment (figure taken from [123]). On the right: simple sketch of a tandem accelerator's internal structure and working principle (taken from [125]). For details on the tandem accelerator refer to e.g. [86].

Thus, the excited ^{98}Zr of interest was produced by the ^{96}Zr(^{18}O, ^{16}O)^{98}Zr two-neutron transfer reaction directly at the experimental area; i.e., within the reaction target of the RDDS device. For the lifetime measurement via RDDS following transitions in ^{98}Zr the ROSPHERE array in a mixed configuration of $LaBr_3$(Ce) and HPGe detectors was made use of. The excitation yield of the two-neutron transfer reaction was studied in a previous (test) experiment as part of this work and is described in section 5.2.2.
The experimental equipment, the ROSPHERE array and the RDDS (Plunger) device and the targets employed, are introduced in the following subsections. Additionally, transferring the RDDS method into the DSA method (cp. chapter 4.1) in the

case of no distance between excitation target and stopper, i.e. a backed target, for measurements of shorter (sub-ps) lifetimes can be utilized. A part of the experimental time was allocated to DSAM measurements on ^{98}Zr. However, within this work the obtained data was not employed for the analysis of lineshapes for level lifetime studies. It will therefore only be mentioned in the outlook section 7.

5.2.1 Experimental Equipment

The RDDS method applied for the lifetime studies of this experiment requires a set of equipment, which is shortly described in this section: a γ-ray spectrometer for detection of de-excitation γ-rays of the produced ^{98}Zr, and the plunger device including sophisticated targets. While the γ-ray spectrometer, ROSPHERE, remained the same between the main experiment and the foregoing production-reaction test studies (cp. section 5.2.2), multiple targets with different properties and purpose were used.

ROSPHERE

The Romanian array for Spectroscopy in Heavy ion Reactions (ROSPHERE) [126] is a recently commissioned detector array specifically designed for applications at the IFIN-HH 9 MV tandem facility. It comprises a total set of 25 detectors (interchangeable HPGe or $LaBr_3$[Ce]), spherically positioned around a target chamber in an arrangement of five rings at azimuthal angles of 37/143°, 90° and 70/110° to the focal plane. A schematic is shown in figure 5.15. The employed HPGe detectors are complemented by state-of-the-art BGO shields allowing for Compton-suppression and, thus, increasing the peak-to-total ratio for observed γ-rays of interest. Also, the combination of both fast-timing ($LaBr_3$[Ce]) and high-resolution (HPGe) detectors allows a combined measurement of lifetimes by FEST (fast-electronic scintillation timing) and RDDS (cp. section 4.1). The achievable total efficiency for γ-ray detection is 1.1% at 1332 keV, and the energy resolution of the HPGe detectors is typically at 1.9 keV (FWHM) at the same energy.

Plunger Device and Targets

The employed RDDS technique for lifetime measurement requires a sophisticated device to ensure precisely-known and long-term stable distances between excitation target and the stopper. Those are prerequisites for the high-precision measurement of lifetimes as the resulting accuracy scales directly with the accuracy on the

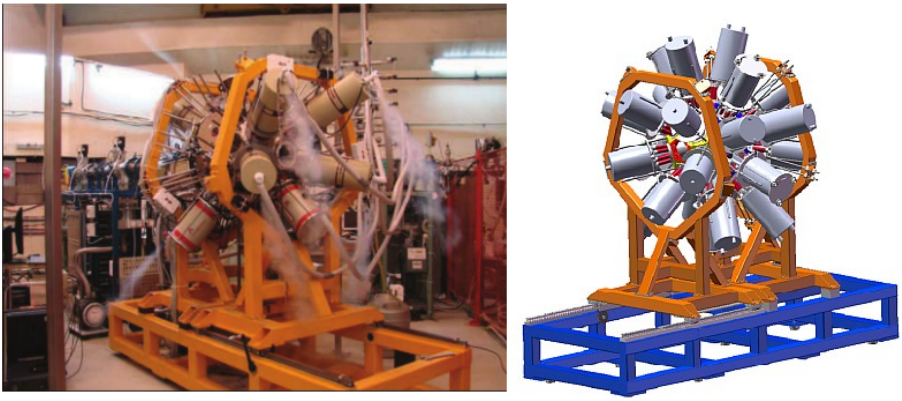

Figure 5.15.: The ROSPHERE array of HPGe and $LaBr_3$(Ce) detectors in operation during the experiment (left-hand side). On the right: CAD (computer-aided drawing) schematics of the array taken from [127].

distances (cp. section 4.1). For this, a plunger device similar to the well-established Cologne coincidence plunger [128], as shown in figure 5.16, was employed in this experiment. With this device, a maximum distance of 25 mm with a measured positioning precision of 0.02 μm (for the mechanical holding structures without targets [126]) can be achieved. Additionally, piezo-ceramics, varying the distance depending on a control-capacity input, allow the correction of beam-target-induced distance drifts, e.g. by target heating, by an automatic feedback. Conclusively, a stable distance precise up to 0.1 μm is achievable.

Three different ^{96}Zr targets were mounted onto the plunger device during the course of the experiment, specified by the material used, its thickness and the backing. Some aspects of ^{96}Zr targets of general importance worth noting: The processes involved in the enrichment of natural Zr to ^{96}Zr (natural abundance distribution: ^{90}Zr: 51.5% , ^{91}Zr: 11.2%, ^{92}Zr: 17.2%, ^{94}Zr: 17.4%, ^{96}Zr: 2.8% [16]) leaves the material in a rough poly-crystal structure impeding the production of thin, even-surfaced RDDS targets. Also, due to its chemical properties Zr is a highly reductive material making it a getter for oxygen and, thus, prone to oxidization.
The used targets are described in the following:
Excitation Function Target: The target used for the test experiment (cp. section 5.2.2) consisted of an unknown mixture of stable Zr isotopes including the ^{96}Zr of interest. It had a thickness of 1.29 mg/cm^2 and was backed by a 6 mg/cm^2 layer of

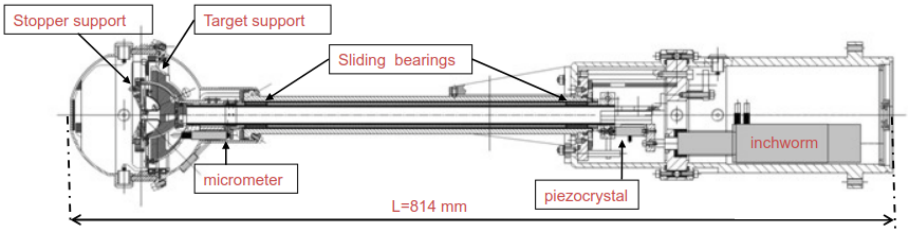

Figure 5.16.: Schematic of the IFIN-HH coincidence plunger. Its use ensures the stability and precision of the distance between the target and the stopper in the RDDS method. Figure taken from [92] with slight modifications.

Pb to completely stop the reaction products and, thus, avoid any Doppler shifts in measured transition energies from levels longer-lived than some picoseconds. The aged material was partly oxidized.

RDDS Target: The material used for the lifetime measurement with RDDS was chemically analysed before being processed into a target. It had a high chemical purity (total impurity <1%) and the Zr isotopic distribution was known (^{90}Zr: 9.2% , ^{91}Zr: 2.0%, ^{92}Zr: 27.2%, ^{94}Zr: 4.2%, ^{96}Zr: 57.4%). It was mechanically rolled to a RDDS foil with a thickness of 0.8 mg/cm^2. The poly-crystalline structure of the material resulted in an uneven target surface with local aberrations from uniformity as depicted in figure 5.17. No backing was used here and the reaction products were stopped downstream in a gold stopper.

DSAM Target: For the slowing-down of the excited reaction products, as required for use of the DSA method (cp. section 4.1), the same material as for the excitation layer was used. However, the thickness was much larger. Thus, the DSAM target consisted of one thick 9.2 mg/cm^2 layer of the material employed for the RDDS measurement. No additional backing was needed since that thickness already ensured that no Zr ions left the target after the reaction.

5.2.2 Proof of Method and Excitation Function

To test the applied method and get an estimate for the yield by the production mechanism to be experimentally employed, the ^{96}Zr(^{18}O, ^{16}O)^{98}Zr two-neutron transfer, a reaction study in a foregoing experiment was performed. While qualitatively well-understood, the kinematics and the expected yield of the reaction had to be quantified before the real experiment could be performed. The require-

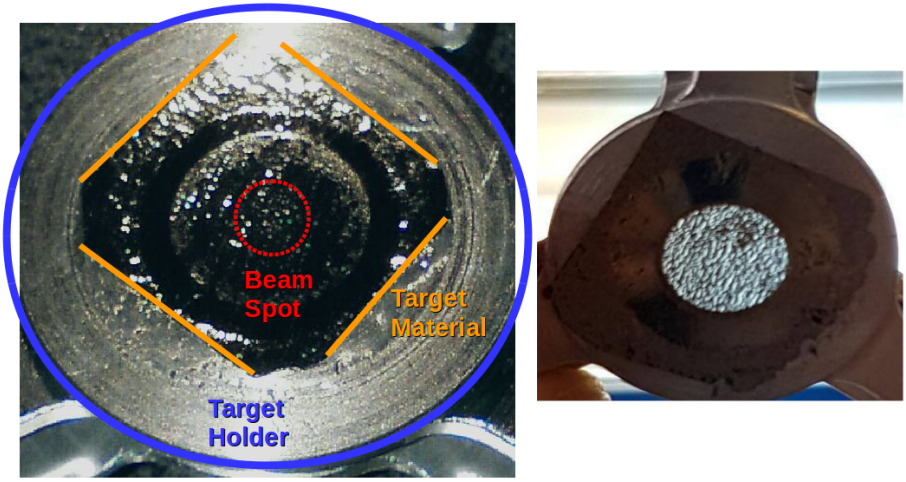

Figure 5.17.: The ^{96}Zr RDDS target as used in the main part of the experiment for lifetime studies. Processing-induced local non-uniformities are visible by eye (right: with background light). The target holder and target material, as well as the beam spot area are highlighted (left).

ments on the reaction kinematics were a large momentum transfer from the beam to the target to ensure the reaction and the acceleration of target-reaction products in forward directions. By this the scattering of the beam ions to backward angles after reaction and the choice of the beam energy are implied. The aim of this preparatory experiment, thus, was multi-fold: First and foremost to proof that the production of ^{98}Zr in excited nuclear states was possible. Secondly, since the kinematics calculation (performed with the code PTOLEMY [129] for this reaction, cp. figure 5.18) showed [130] that the ^{18}O would recoil in backwards directions, which were mechanically occupied by the plunger device in the RDDS experiment, its detection with particle detectors would not be possible. Thus, a condition on the reaction partner for a clear separation of ^{98}Zr from other reaction products, had to be performed by γ-γ coincidence conditions in the Ge detectors.

Whether gating on a transition of ^{98}Zr this way would result in pure γ-ray spectra of ^{98}Zr decays had been unclear and therefore to be tested. In case of a positive outcome of the first two experimental aims, the third and final objective was the determination of an excitation function of the employed production reaction; i.e., its cross section over a range of varying beam energies, and, in particular, its maximum. This excitation function would allow to fix the beam energy for the sub-

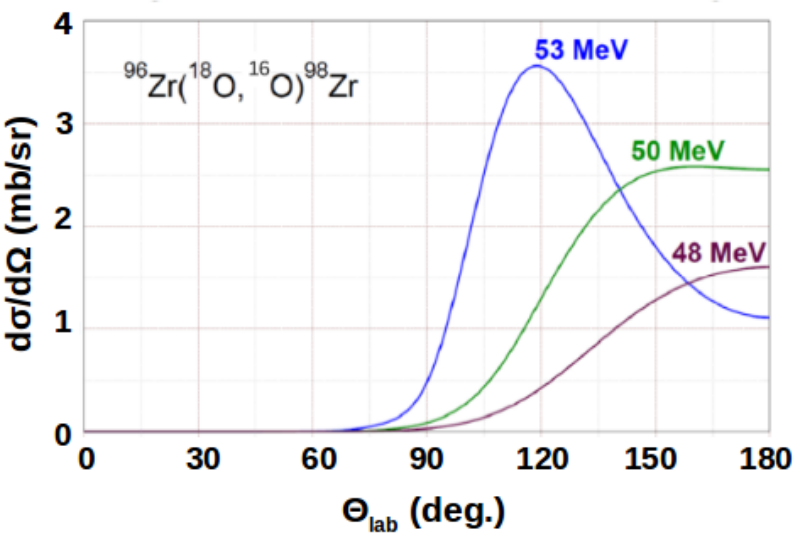

Figure 5.18.: The calculated [130] kinematics relation for the ^{96}Zr(^{18}O, ^{16}O)^{98}Zr two-neutron transfer shown as differential reaction cross section over the scattering angle Θ_{lab} for different incident beam energies. Scattering of the ^{18}O to backward angles is implied, as well as a suggestion for the range of beam energy.

sequent experiment to be performed and maximize the results of the experimental beamtime.
The test experiment was performed at IFIN-HH with employment of the ROSPHERE array and the (oxidized) backed ^{96}Zr target as described in section 5.2.1. The ^{18}O beam energy was varied in the range suggested by the kinematics calculation (from 47 to 54 MeV). The γ-ray de-excitations following the reaction were measured with the HPGe detectors of the ROSPHERE array. However, the two-neutron transfer reaction of interest was competing with other reactions creating a substantial γ-ray background by decays of their products. By quantity the main contributions to this were fusion-evaporation reactions of the beam ions with the ^{16}O and the Zr in the target. Also, the beam was not completely pure and partly included ^{16}O, which contributed to additional undesired reactions products. The cross sections for the competing fusion evaporation products were approximately (regarding their absolute value) calculated with the software CASCADE [131], and, thus, the main input for the γ-ray background was identified. For the detailed results of the calculations please refer to the appendix A.3. The most-likely products were ^{28,29}Si, ^{30,31}P, ^{27}Al and ^{24}Mg from O-O reactions, and ^{108,110}Cd from O-Zr reactions. The decays of produced ^{31}P (1266 keV), ^{29}Si (1273 keV) and ^{24}Mg (585 keV!) were the most problematic ones for the experimental aims. The reason being their low-energy level transitions lying energetically close to the ones of interest of ^{98}Zr (1222 keV and 583 keV).
The γ-ray spectrum measured with the HPGe detectors of ROSPHERE is depicted in figure 5.19. The identification of the $2_1^+ \rightarrow 0_1^+$ of ^{98}Zr transition, separated from the background, proofed to be achievable. For this a coincidence γ-energy condition was set on the higher-lying $3_1^- \rightarrow 2_1^+$ transition of of ^{98}Zr. Therewith, the first two aims of the test experiment; i.e., the proof of the reaction mechanism, and the γ-ray spectrum separation by coincidence gating, have been accomplished.

For the excitation function similar γ-energy spectra were taken following a variation of the beam energy. The result, which is a relative intensity distribution of the ^{98}Zr $3_1^- \rightarrow 2_1^+$ and $2_1^+ \rightarrow 0_1^+$ transition yields over the incident ^{18}O beam energy, is depicted in figure 5.20. Here, the same behaviour of the two transition yield curves over the beam energy is evidence for the coincidence of $3_1^- \rightarrow 2_1^+$ and $2_1^+ \rightarrow 0_1^+$ transitions, as expected considering the energy condition employed. Finally, an expected yield rate and the required beam energy for its maximum can be derived from this: $\sim$100 observed $2_1^+ \rightarrow 0_1^+$ transitions of ^{98}Zr per hour of beam-on-target time at an ^{18}O beam energy of 51.5 MeV. Considering the reaction kinematics and the ROSPHERE HPGe detector positions (angles), a slight adjustment to 49 MeV beam energy had to be made for the final experiment to prevent

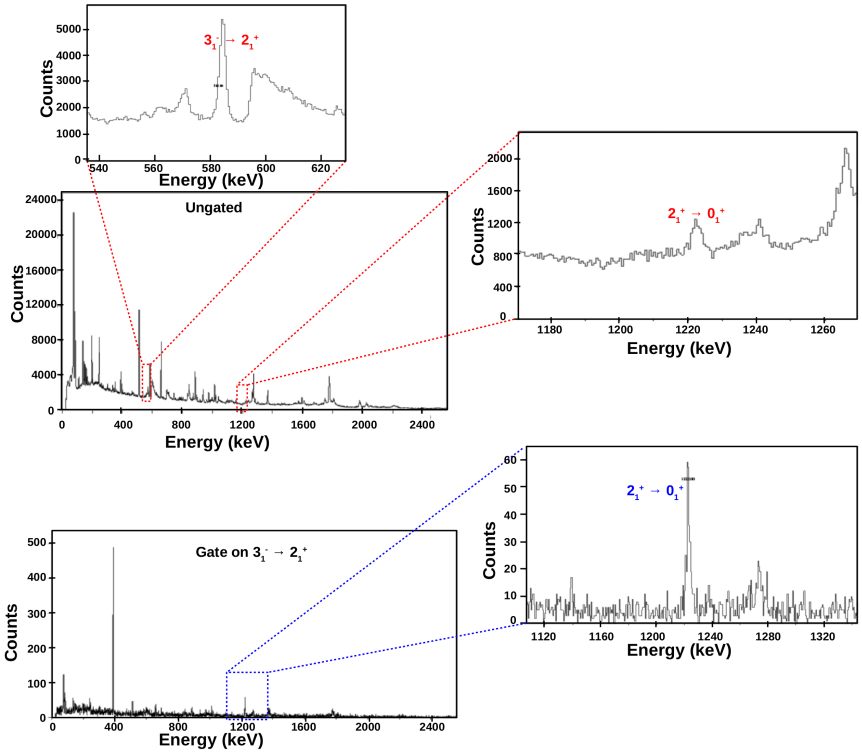

Figure 5.19.: γ-ray spectra measured with the HPGe detectors of ROSPHERE with and without γ-γ condition on a populating transition of ^{98}Zr. The clear identification of transitions of ^{98}Zr with the set condition is evident. The $2_1^+ \rightarrow 0_{g.s.}^+$ and $3_1^- \rightarrow 2_1^+$ transitions of ^{98}Zr are marked. Figure taken from the proposal to the experiment [132]; slightly modified.

the produced ^{98}Zr ions to be scattered at an angle of 90°, and, thus, ensuring a significant Doppler- shift of the observed γ-ray energies relevant for the application of the RDDS method. Additionally, the average velocity of the ^{98}Zr ions after reaction was calculated to be 0.5-1% of c after leaving a target with corresponding thickness of $\leq$ 1-1.5 mg/cm^2. The details of this calculation, including the ion energy loss within the target taken from [96], are shown in appendix A.4.

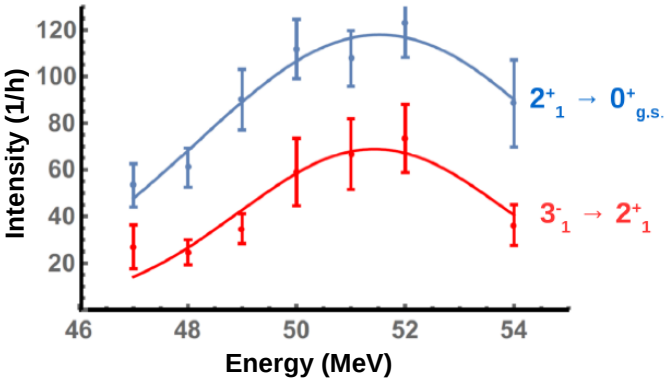

Figure 5.20.: Intensities of the $3^-_1 \rightarrow 2^+_1$ and $2^+_1 \rightarrow 0^+_1$ transitions of ^{98}Zr as observed following the producing two-neutron transfer reaction as a function of the incident beam energy. Figure taken from the proposal to the experiment [132]; slightly modified.

The findings of the test experiment, the optimum beam energy and beamtime requirement based on the excitation function, served as input for the final experiment. This is described in the following section 5.2.3.

5.2.3 RDDS/DSAM Lifetime Measurement

Following the preparations previously described in section 5.2.2, the final experiment aiming at ^{98}Zr level lifetime measurements was performed at IFIN-HH with the same experimental setup as in the test experiment including the ROSPHERE array in a configuration of 15 HPGe detectors at the 90° and 37/143° positions (five detectors per position), each coupled to an active BGO shielding, and ten $LaBr_3$(Ce)

detectors. The geometry and the detector angles relevant for the RDDS analysis are depicted in figure 5.21. The employed RDDS and DSAM targets are described in section 5.2.1. Initially, an experimental beam-on-target time of, in average, two days per RDDS target-stopper distance and measurements at a total of ten different distances were planned. This was based on the reaction yield findings of the test experiment and the set requirement of ∼1000 coincident γ-γ transition counts per distance for a resulting lifetime measurement of the 2_1^+ level of ^{98}Zr with an uncertainty $\leq$ 5%. However, since the required maximum RDDS target thickness (1.5 mg/cm^2) was problematic to achieve without breaking the foil (cp. section 5.2.1), i.e. by a repetitive cold-rolling procedure for $\sim$ 2 days, a thicker DSAM target was employed first for a part of the beamtime. An additional challenge was the fast oxidization of the used target with high beam currents resulting in the necessity for reduced beam currents as compared to the test experiment and the eventual "burning" of the DSAM target. Nonetheless, in total, an effective beam-on-target time of two days for the DSAM measurement and eight days for five distinct distances of the RDDS measurement was achieved. This section describes the RDDS lifetime analysis of the experiment, which was performed as part of this work. The DSAM lifetime analysis is out of scope here and was only used for the determination of feeding levels.

Reaction Cross Sections

As already mentioned, the production mechanism of 2n-transfer was competing with other reactions, i.e. Coulomb excitation and fusion-evaporation. To get an estimate on the order of involved cross-sections, a rough reaction-product yield study was performed. For this, γ-rays corresponding to transitions of the main fusion evaporation (FE) product ^{110}Cd, of the Coulomb excitation (CoulEx) of the RDDS stopper material ^{196}Au, and of the 2n-transfer product of interest, ^{98}Zr, were compared. The following ratios were obtained:

$$\sigma_{2n}/\sigma_{CoulEx}=0.9(2), \text{ and } \sigma_{FE}/\sigma_{CoulEx}=6.8(1).$$

Making use of the code CLX [76], the observed yields of ^{196}Au transitions were correlated to an Coulomb excitation cross section of σ_{CoulEx}=87(20) mb. The input file for this calculations [133] can be found in appendix A.5. With this, the cross sections are obtained for all the observed reactions, cp. table 5.2.
Those values are in line with the fusion evaporation cross sections obtained with CASCADE for the test experiment and typical Coulomb excitation cross sections, respectively. In particular, the dominance of the fusion evaporation reaction at

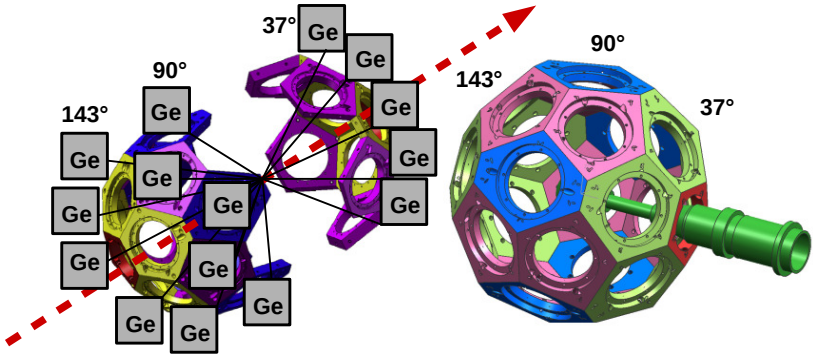

Figure 5.21.: Geometry of the ROSPHERE array configuration employed in the experiment. On the left: CAD of the open detector holder structures taken from [127]; the red dashed line depicts the beam axis. Additionally, the positions of the HPGe detectors for the used configuration are sketched. Right-hand side: closed holder structure with the ring colors corresponding to the azimuthal angles of the detectors positioned within (blue: 90°, light green: 37/143°); original CAD figure taken from [127].

Table 5.2.: Cross sections of the reactions observed in this experiment. Ratios stem from the experiment and are related to the calculated Coulomb excitation cross section.

Reaction	Product	Yield Ratio	Cross Section (mb)
Coulomb excitation	^{196}Au	1 (norm.)	87(20)
Fusion Evaporation	^{110}Cd	6.8(1)	592(152)
2n transfer	^{98}Zr	0.9(0.2)	78(27)

49 MeV (below the Coulomb barrier energy at 50.3 MeV [131]) is therefore quantified.

Data Preparation

This section deals with the rehashing of the experimental RDDS data, which prepares it for further analytic steps and, finally, the RDDS lifetime determination covered in the following section 5.2.4.
The first steps of this data preparation are the calibrations of detector efficiency and energy. Furthermore, energy and time conditions set on the detectors' (HPGe, BGO, $LaBr_3$[Ce]) output signals, are elaborated on. They are made use of to clean up the resulting γ-ray energy spectra measured with the HPGe detectors of ROSPHERE. Additionally, the analysis of the experimental RDDS data is complicated by the non-uniformities of the employed target. Since the measured distance between reaction target and stopper (i.e., the distance between the target holders) is not equal to the distance between their surfaces, an offset has to be accounted for. This offset is defined as the distance between the mechanical (touching target holders without material) and electrical contact (touching target surfaces), and was calibrated (i.e., measured distances shifted to real distances by regression) for the fist measurement distances. However, this calibration got lost when the target was flattened during the conduction of the experiment, cp. section 5.2.3. This resulted in two different plunger-distance offsets for the five target-stopper distances, with unknown second offset. The real distances had to be determined as they are an essential input for the RDDS lifetime analysis.

Energy and Efficiency Calibrations

Similar to the procedure described in section 5.1.2 of the first experiment, the energies and efficiencies of the involved HPGe detectors are calibrated. Known transitions of ^{152}Eu and ^{60}Co sources are used as reference. The achieved energy accuracy after calibration is $\leq$0.5 keV with an internal energy resolution of $\sim$2 keV. For the efficiency as example a typical efficiency curve of one HPGe detector is shown in figure 5.22. The calibrations were also performed for the LaBr(Ce_3) detectors. Since the BGO detectors are merely used as a veto for Compton-scattered events, their calibration is not needed. Also, the time information of the HPGe detectors can be used without absolute numbers. Additional information on the efficiency and energy calibrations can be found in appendix A.6.

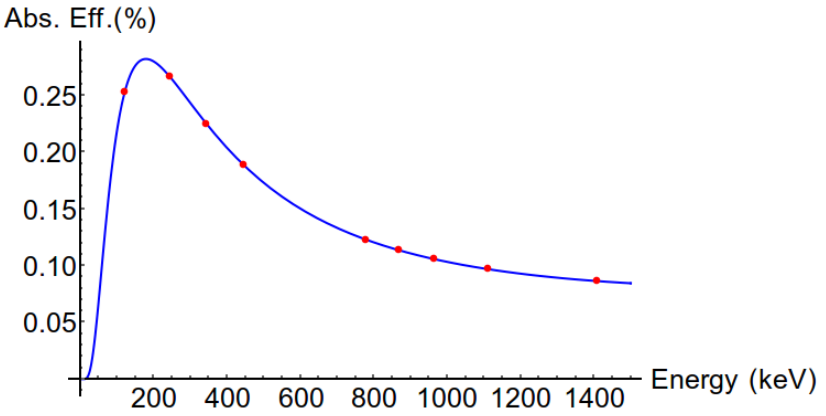

Figure 5.22.: Absolute efficiency curve for one exemplary HPGe detector of the ROSPHERE array after normalization of measured signals to reference transitions of ^{152}Eu and ^{60}Co. The depicted fitted curve's function is used for inter- and extrapolation for observed transitions outside of the reference transitions range.

RDDS Target-Stopper Distance Calibration

The RDDS measurement was performed at three known distances (offset between real to measured distance shifted to zero by calibration) of the excitation target to the stopper: 25, 74, and 148 μm, with an uncertainty of 2 μm each (based on position fluctuations observed during the experiment). As smaller distances showed a more distinct Doppler-unshifted component in the γ-ray spectrum; i.e., as measurements at smaller distances are more sensitive to the lifetime to be measured here, the stopper-target distance was reduced for further measurements. However, due to the non-uniformity of the target a closer distance could not be achieved without electrical contact of target with the stopper. Flattening the target, and, thus, reducing the minimum possible distance, resulted in a change of the before-calibrated distance offset. The real distance could therefore not be determined directly by the usual plunger device distance determination. Measurements at two additional (comparably small) distances were performed. To combine them with the previous RDDS measurements, the respective stopper-target distances had to be normalized. This was done by referencing the decays of the main product of another reaction product competitive to the two-neutron transfer for production of the ^{98}Zr of interest. Namely, known transitions observed in ^{110}Cd following fusion evaporation of the ^{18}O beam on the ^{96}Zr target (cp. section 5.2.2) were

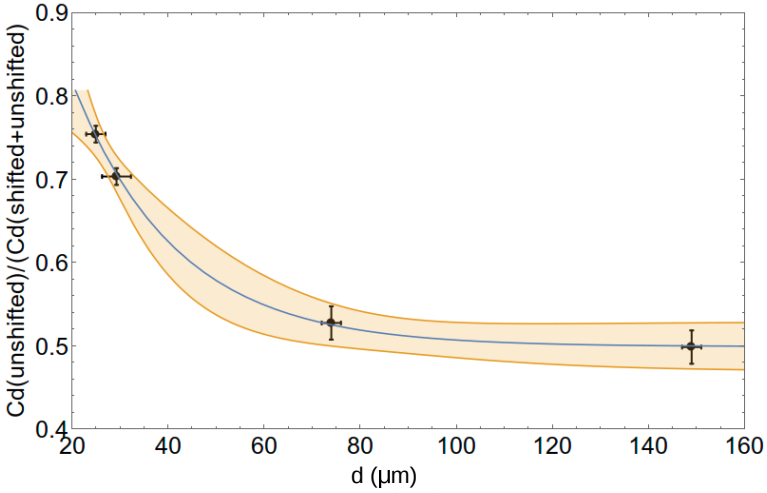

Figure 5.23.: RDDS decay curve of ^{110}Cd determined by its $2_1^+ \rightarrow 0_{g.s.}^+$ transition. Shown are a decay curve fit to the ratio of unshifted to total Cd transitions measured at the known target-stopper distances including uncertainties and feeding. Aligning the ratios measured at unknown distances to this curve is used to fix their offset. Thus, the data can be combined.

employed. Since the known level half life ($T_{1/2}$=5.42 ps [16, 134]) corresponding to the observed transition ($2_1^+ \rightarrow 0_{g.s.}^+$ at 648 keV) was in the range to be measured with the RDDS technique with the set plunger distances, the nominal distance values could be related to the decay behaviour of the regarded level. A lifetime of 7.2(7) ps was obtained from the decay of the level (including feeding from the higher-lying 4_1^+ state), which is in agreement with the literature value of $\tau_{lit.}$=7.8(2) ps. Figure 5.23 depicts the decay curve for the $2_1^+ \rightarrow 0_{g.s.}^+$ transition of ^{110}Cd as function of the excitation target-stopper distance. From this decay curve and the ratios of Doppler-unshifted components to total $2_1^+ \rightarrow 0_{g.s.}^+$ transitions of ^{110}Cd observed at the unknown distances, the plunger distances corresponding to those ratios were determined. The real distances were deduced to be 25.0(30) μm and 29.3(30) μm. Thus, summing up the data for the two measurements at 25 μm, the following four distances were used for the RDDS measurement: 25.0(30) μm, 29.3(30) μm, 74.0(20) μm, and 148.0(20) μm.

Determination of Detector Conditions (Gate Ranges) for Cleanup of γ-ray Energy Spectra

As has been previously shown, the 2n-transfer reaction producing the nucleus of this experiment's interest, is competing with other (stronger) reaction channels. Also, contributions to the measured γ-ray energy spectra are, as usual, made from background radiation. Thus, the measured transitions are very likely to not only stem from ^{98}Zr. An approach to improve on this situation is the employment of conditions on the signals measured with the used detectors. The effect to be achieved to increase the peak-to-background ratio of ^{98}Zr transitions of interest to simultaneously measured transitions of fusion-evaporation products and/or environmental background. For this the time differences obtained between the HPGe detectors and HPGe, $LaBr_3$(Ce), and BGO detectors are analysed and combined. A time condition on the Ge and $LaBr_3$(Ce) detectors ensures that the event detected in a BGO detector can be correlated to an event in the HPGe detectors. Thus, rejecting events measured in the HPGe with a timely correspondence in the BGOs ensures that Compton-scattered γ-rays do not contribute to the energy spectrum measured with the HPGe detectors. Also, timely-uncorrelated random events can be suppressed with the use of those conditions.

Typical time difference spectra obtained in the HPGe, $LaBr_3$(Ce), and BGO detectors respectively are depicted in figure 5.24. Additionally, the gating conditions are shown. The obtained effect of the time conditions on the HPGe energy spectra is shown in figure 5.25 and an improvement of intensity of the transitions of interest to the background is clearly visible; e.g., for ^{110}Cd an improvement in peak-to-background ratio from $\sim$1.5 to $\sim$4.0. In particular, transitions stemming from environmental background (^{40}K, ^{214}Bi) are suppressed.

5.2.4 RDDS Analysis for Lifetime Determination

After the preparation and cleanup of the obtained γ-ray energy spectra, the ^{98}Zr transition of interest, the $2_1^+ \rightarrow 0_{g.s.}^+$ at 1222 keV, and its Doppler-shifted component are observed for forward and backward-positioned HPGe detectors. Since the Doppler shift is directly dependent on the detector angle, the transition is shifted to higher energies at forward angles and to lower energies at backward detectors (cp. equation 5.5). The shifted and unshifted components are integrated respectively for each of the four distinct plunger distances. The correspondence of the shifted component to the transition of interest can be verified by both the direction of the energy shift when going from backward to forward angles and by the growing shifted component when going to larger target-stopper distances. Two

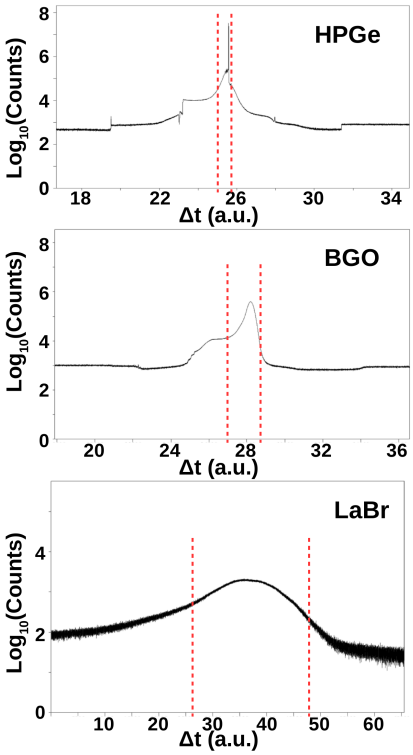

Figure 5.24.: Time difference (w. r. t. to the HPGe detectors) spectra obtained in the HPGe, BGO, and $LaBr_3$(Ce) detectors and the conditions used are depicted. Note the logarithmic y-scale. A combination of those conditions suppresses Compton-scattered and random (background) events in the resulting HPGe energy spectra. Thus, a cleanup of the spectra can be achieved.

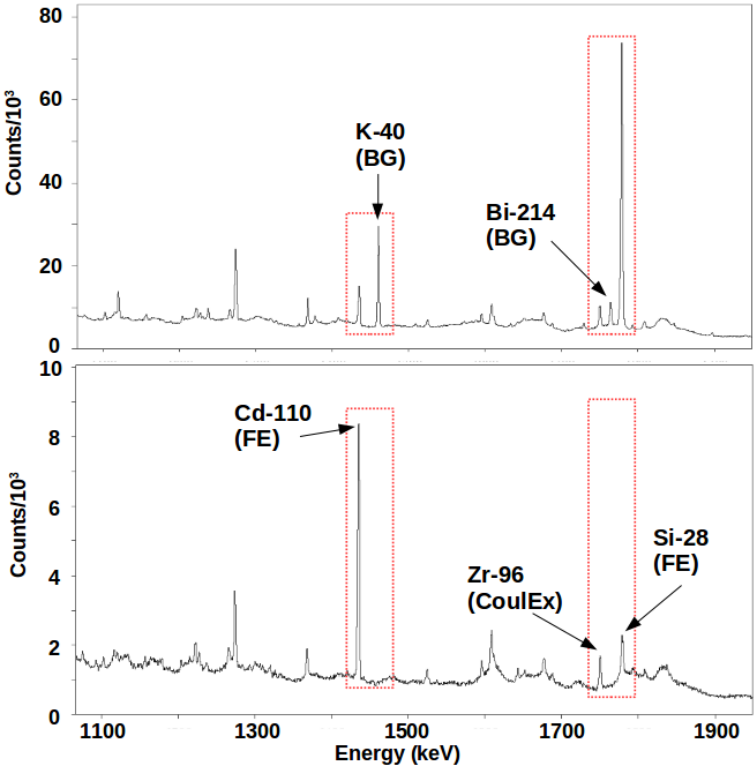

Figure 5.25.: Energy spectra obtained in the forward-angle HPGe detectors before (top) and after (bottom) application of the detector timing conditions described in the text. An example energy range is chosen: Here, the vanishing of background transitions, e.g. the 1460 keV line from ^{40}K decays, is evident. As effect, the relative transition peak height from reaction products to the background increases.

complications have to be taken into consideration here: The Doppler effect also applies to other energetically close-lying transitions not related to ^{98}Zr stemming from levels with a similar lifetime range. Thus, the shifted energies corresponding to those transitions pose an additional contamination to the spectrum. Also, since the solid angles of the HPGe detectors range according to the detector geometry, the Doppler-shifted component is smeared out; additionally, straggling within the target can be assumed to contribute here. From the center of this shifted energy distribution an average energy shift of 10 keV between unshifted and shifted component can be extracted. Thus, an average velocity of the ^{98}Zr ions of v/c =1.0(1)% after the producing 2n-transfer reaction and after the deceleration in the excitation target can be deduced. This is in agreement with the preceding velocity estimate calculated for the test experiment, cp. section 5.2.2.
Since the shifted component of the $2_1^+ \rightarrow 0_{g.s.}^+$ transition of ^{98}Zr is smeared up in the background, only the unshifted part (from decays at rest) is used for the RDDS lifetime determination. This is normalized to the total (Doppler-shifted and unshifted part) amount of $2_1^+ \rightarrow 0_{g.s.}^+$ transitions of ^{110}Cd at the respective distances. The obtained ratios can be correlated to the lifetime of interest by the RDDS equation given in section 4.1. A total spectrum over all plunger distances and detector angles is depicted in figure 5.26; marked are positions of the $2_1^+ \rightarrow 0_{g.s.}^+$ transition peaks of ^{98}Zr peaks stemming from decays at rest and their symmetrically Doppler-shifted components.

The obtained ratios over the plunger distances are plotted in figure 5.27. Naively, an exponential decay with variable lifetime could be fitted to yield the corresponding level lifetime. However, the 2_1^+ level of interest is not only populated directly, but also by decays of higher-lying levels, which are observed in the measurements; in particular, in the DSAM measurements. To take into account this feeding effect on the obtained lifetime, the DSAM spectra are regarded in singles and in γ-γ coincidences gating on the $2_1^+ \rightarrow 0_{g.s.}^+$ transition of ^{98}Zr. From the yield ratios of observed feeding transitions to the ground state transition, the total amount of indirect to direct population and the feeder decomposition can be deduced. Table 5.3 shows the contributions of identified feeding levels. Two of the feeding transitions (from the 2_3^+ level with 521.6 keV, and from the 3_1^- level with 583.3 keV) are overlapping with transitions of the fusion evaporation products ^{27}Al and ^{25}Mg in the spectra. Their contribution to the feeding of the 2_1^+ level can therefore not be obtained from the singles spectra. Assuming a $3_1^- \rightarrow 2_1^+$ transition strength similar to the one found in the neighbouring ^{96}Zr [16, 32], the lifetime of the 3_1^- level of ^{98}Zr is estimated to be in the sub-picosecond range. Since its effect on the few-picoseconds lifetime of the 2_1^+ is minor, its feeding is neglected. With the same reasoning, i.e. too short-lived for considerable effect, the indirect population from

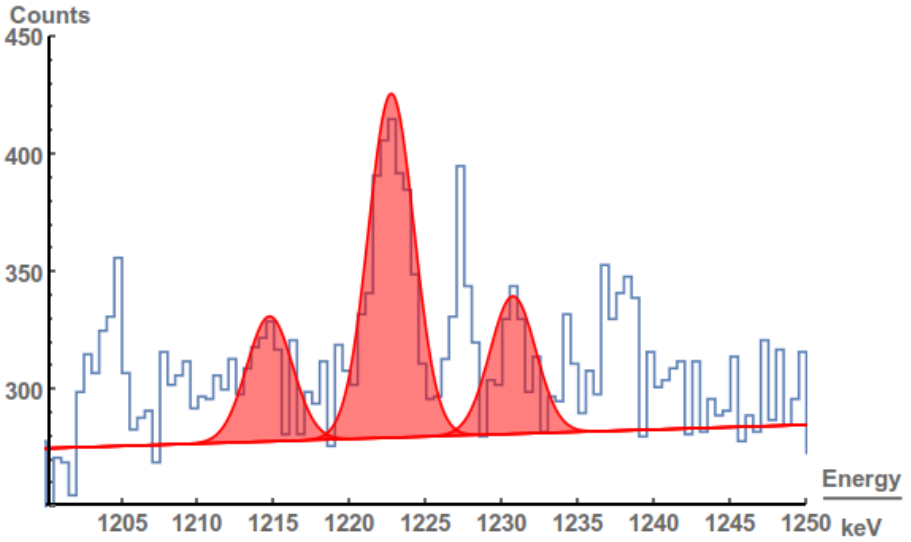

Figure 5.26.: Zoom into RDDS γ-ray energy spectrum measured with the ROSPHERE HPGe detectors. Marked are the unshifted (center) and the Doppler-shifted (left, right) components of the $2_1^+ \rightarrow 0_{g.s.}^+$ transition of ^{98}Zr. Since the statistics does not allow a proper Gaussian fit, the distributions are simply integrated for the determination of their centres. Also, the background is drawn (no fit) just to guide the eye. The peak at $\sim$1227 keV is attributed to a contaminant transition.

Feeder	Transition energy (keV)	Ratio to dir. pop.	Comment
0_3^+	213	0.1	negl., τ >1 ns
2_3^+	522	unknown	Cont.: ^{27}Al, τ <1 ps
3_1^-	583	unknown	negl., τ <1 ps
4_1^+	621	0.16	τ=7.5(18) ps [135]
4_2^+	825	0.07	τ variation irrelevant

Table 5.3.: Feeding decomposition of the 2_1^+ level of interest as deduced by γ-γ-coincidences to the $2_1^+ \rightarrow 0_{g.s.}^+$ transition. Transitions overlapping with contaminants transitions marked as unknown. For details refer to the text.

decays of the 2_3^+ level can be considered as direct feeding in good approximation. For the 4_1^+ level the lifetime measured in another experiment [135] is employed. A variation of the lifetime of the feeding 4_2^+ level did not show any significant effect on the resulting lifetime of the 2_1^+ level due to its small ratio. The indirect population stemming from the 0_3^+ level only contributes to a constant background in the effective RDDS decay curve, as its known half life of 1.24 ns [16, 27] is too large on the time scale of interest here.

The feeding level lifetimes and their relative contributions to the indirect population are all taken into account for by fitting a decay curve in the shape of the Bateman-equation (cp. section 3.1) to the experimentally obtained ratios. This is depicted in figure 5.27 and allows the direct determination of the last remaining variable, the lifetime of the populated 2_1^+ level.

Based on the function fitted to the obtained decay curve, with the known recoil velocity a lifetime of $\tau(2_1^+)$=4.0(8) ps is deduced. Taking into account uncertainties from the feeding (i.e. assuming no feeding compared to the determined feeding) and the recoil velocity spread, as well as the fit error, this transfers to a B(E2; $2_1^+ \rightarrow 0_{g.s.}^+$) transition strength of $2.8^{+1.1}_{-0.7}$ W. u. This determined lifetime is the main result of this experiment. It is compared to the results of the first experiment in the following section 5.3.

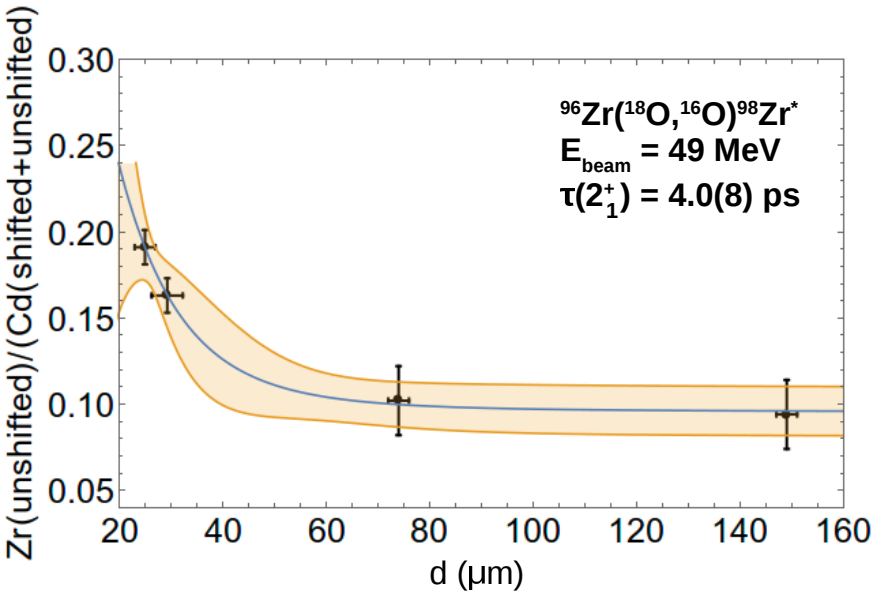

Figure 5.27.: RDDS decay curve for the $2_1^+ \rightarrow 0_{g.s.}^+$ transition of ^{98}Zr as obtained from the ratios of the unshifted component to the total (shifted and unshifted) component of the ^{110}Cd transition peak) over different plunger distances. The fitted function takes into account the feeding from higher-lying levels in accordance with the Bateman-equation for multi-step decays. From the fit the lifetime τ =4.0(8) ps of the 2_1^+ level is obtained.

5.3 Results

This section briefly summarizes the results of the two performed experiments to measure the B(E2; $2_1^+ \rightarrow 0_{g.s.}^+$) transition strength, respectively the lifetime of the 2_1^+ level, of ^{98}Zr. The obtained combined results are used to complete the known systematics of $B(E2)$ transition strength evolution in the Zr isotopic chain as development of neutron number N. Any interpreting conclusions and follow-up discussions that build up on these combined results will be addressed in the following chapter 6.

5.3.1 Transition Strength Limit and Lifetime Determination

The transition strength limit obtained by the Coulomb excitation experiment at ANL, cp. chapter 5.1, 1.83 W. u.<$B(E2; 2_1^+ \rightarrow 0_1^+)$<11 W. u. agrees very well with the lifetime of the 2_1^+ level τ=4.0(8) ps obtained in the RDDS experiment following the ^{96}Zr(^{16}O, ^{18}O)^{98}Zr 2n transfer at IFIN-HH, cp. section 5.2. The measured lifetime translates to a B(E2) value of $2.8^{+1.1}_{-0.7}$ W. u., and, thus, the value is constrained to the lower edge of the previously limited range. Table 5.4 summarizes the obtained results and shows the $B(E2; 2_1^+ \rightarrow 0_1^+)$ for the neighbouring even-even isotopes in the Zr chain. The results are profoundly discussed in the following chapter 6.

A	$B(E2; 2_1^+ \rightarrow 0_1^+)$ (W. u.)	Reference
90	5.8(9)	[136]
92	6.5(5)	[137]
94	4.7(3)	[31]
96	2.3(3)	[32]
98	>1.8	[28]
98	<11	this work [20]
98	$2.8^{+1.1}_{-0.7}$	this work
98	2.9(8)	[135]
100	80.5(44)	[33]
102	117.3(240)	[138]
104	137.7(207)	[139]
106	104.3(336)	[140]

Table 5.4.: Experimental values for the $B(E2; 2_1^+ \rightarrow 0_1^+)$ values in the Zr isotopic chain from this work and other experiments.

6 Discussion

Having obtained an accurate value for the $B(E2; 2_1^+ \rightarrow 0_1^+)$ transition strength of ^{98}Zr reliably by two independent experiments, this chapter transposes to the conclusions and discussion building on the results.

The scope of the results is better illuminated when regarded in the development of $B(E2; 2_1^+ \rightarrow 0_1^+)$ transition strength in the Zr isotopic chain, as depicted in figure 6.1. Prior to this work's result, the B(E2) value for ^{98}Zr could naively be assumed to be mid-way between the comparably very low transition strength ∼2 W. u. found in ^{94,96}Zr and the strongly different, high B(E2) values found in ^{100,102,104}Zr. While the limits from the first experiment already show a clear orientation of ^{98}Zr towards the trend of the lower-N Zr isotopes, and, thus, increase the abruptness in the rise in B(E2) value when going to A=100, the fixing of the B(E2) value to the same level as ^{94,96}Zr additionally excludes any rise between ^{96}Zr and ^{98}Zr. Therefore, any physics origin causing this abrupt change in the systematics of observables, can be pinpointed to happen between N=58 and N=60.
In the following, first, another observable, which is directly depending on the result, will be deduced and discussed. Then, the results are put into systematic context of similar and other observables within this nuclear region to derive a conclusive picture of the effects caused by the involved physics processes. This is followed up by comparison of the data to theoretical model calculations. And last, but not least, the results are discussed in the frame of shape evolution to close the circle to the ideas initially motivating the experiments, and bring back general physics concepts to the foreground.

6.1 Deduction of the $B(E2; 2_1^+ \rightarrow 0_2^+)$ transition strength value in ^{98}Zr

Fixing the B(E2; $2_1^+ \rightarrow 0_1^+$) transition strength value of ^{98}Zr directly allows to deduce the transition strength of the 2_1^+ state to the first excited 0_2^+ state. The reason for this is the known γ-ray transition branching ratio of the 2_1^+ level decays [16, 27]. For the obtained value of B(E2; $2_1^+ \rightarrow 0_{g.s.}^+$)=$2.8^{+1.1}_{-0.7}$ W. u. this results in B(E2; $2_1^+ \rightarrow 0_2^+$ =18^{+7}_{-5} W. u. The order of magnitude in strength between the two different transition paths suggest a comparably higher collectivity between the 2_1^+ level and the excited 0_2^+ than between the 2_1^+ level and ground state. While this ratio of

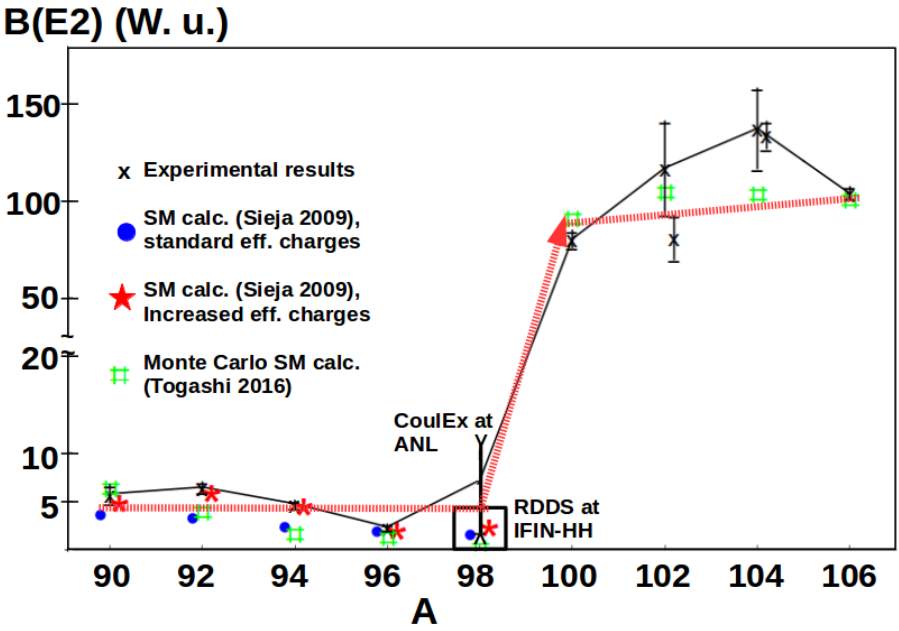

Figure 6.1.: Systematics of the $B(E2; 2_1^+ \rightarrow 0_1^+)$ transition strength in the Zr isotopic chain developing with the mass number A. Previous experimental input and the results of this work for ^{98}Zr are shown. The red dashed line guides the eye on the abrupt structural change established by this work's results. Additionally, theoretical model predictions are depicted. They are discussed in chapter 6. Note the change of y-axis scale. Figure taken from [20] and slightly modified.

the two transition strength values obviously does not change when one of them is fixed, the absolute values obtained by this work's experimental input allow for the classification of the 2_1^+ state as collective excitation on top of the 0_2^+ state. This is emphasized as opposed to classify the 2_1^+ level as a weakly-collective excitation on top of the ground state. Since the collectivity of the 2_1^+ ground state excitation is low and close to what is expected for a spherical structure, and the second structure's 2_1^+ excitation shows a significant collectivity (contrary to both being quite low or large, as is possible with a fixed ratio only), the fingerprint of two distinct level structures with a significant difference in deformation is evident here. The co-existence of a mostly-spherical structure on one hand, and the more collective, possibly deformed, structure on the other hand is the corollary phenomenon of the shape transition predicted for this nucleus by theory, cp. section 2.3. This interplay of collective and single-particle behaviour within the abrupt shape transition sets the theme for this discussion and will be elaborated on in the following.

6.2 ^{98}Zr as Transitional Nucleus in the Zr Isotopic Chain: Systematics

As already put into context of its nuclear surrounding, and the experimental observables connected to it, at the end of section 5.3 in terms of B(E2; $2_1^+ \rightarrow 0_1^+$) transition strength values, regarding the result in the frame of different observable systematics helps understanding the underlying phenomena. Here, next to the systematics of B(E2; $2_1^+ \rightarrow 0_1^+$) transition strength values, the look is directed to level energies, and their numerical differences (spacings) and ratios. The discussed observables are depicted in figure 6.2.

The strong decrease in excitation energies of the low-lying levels from $N=56$ to $N=60$, with the 2_1^+ level energy going from 1751 to 231 keV, comes along with the $\nu 2d_{5/2}$ and $\nu 3s_{1/2}$ (sub)-shell closures at $N=56$ and $N=58$, respectively. The comparably high excitation energies of ^{96}Zr and ^{98}Zr can therefore be explained by the excited neutrons having to overcome the energy gap to higher orbitals; i.e., $\nu 1g_{7/2}$, $\nu 2d_{3/2}$, and $\nu 1h_{11/2}$. Same orbital-crossing holds for excitation of the protons with the pf-$g_{9/2}$ gap to be overcome. Another development of level energy standing out from the systematics, cp. figure 6.2(a), is the 0_2^+ level energy's decrease from 854 keV at $N=58$ to 331 keV at $N=60$. For this the explanation is the structural ground-state change from $N=58$ to $N=60$ with the intruding collective (deformed?) structure in ^{98}Zr developing to the deformed ground state at $N=60$. This is evident from the experimental information available on ^{100}Zr [16, 33].

The structural change between $N=56$ and $N=58$ becomes more visible when regarding the energy differences of ground states and 2_1^+ states, cp. figure 6.2(b). Here, the crossing of energy differences of the 2^+ levels and of the 0^+ levels sug-

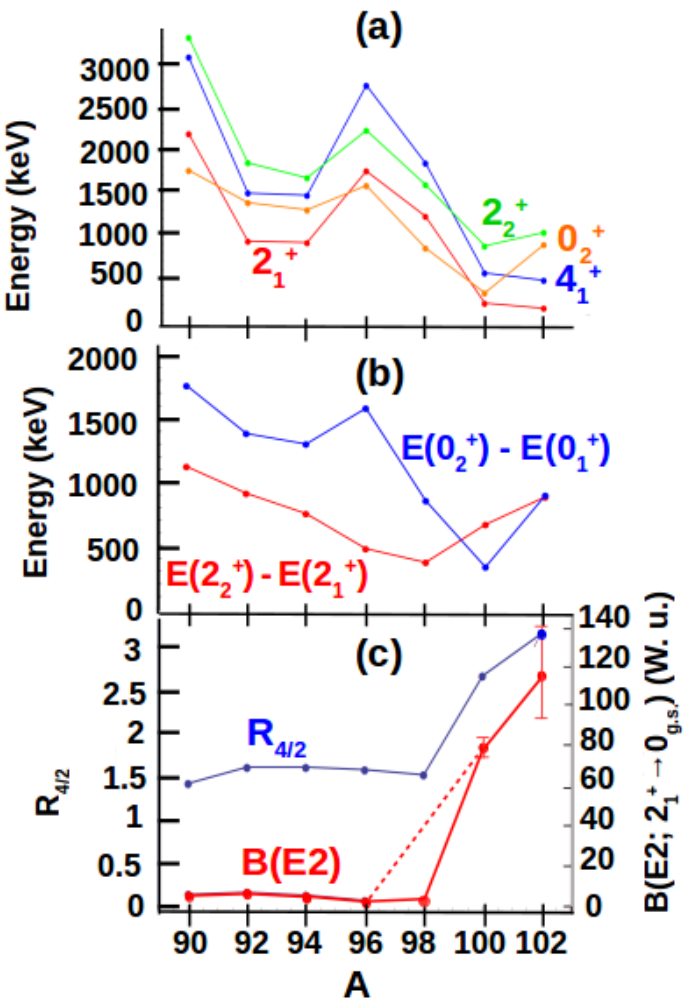

Figure 6.2.: Systematics of (a) the low-lying level energies, (b) the level spacings, and (c) the $B(E2; 2_1^+ \rightarrow 0_1^+)$ transition strength values and $R_4/2$ ratios in the Zr isotopic chain over the mass number A. A structural change becomes evident at ^{98}Zr. It is discussed in the text. Figure taken from [20] and slightly modified.

gests the exchange of the two structures in terms of single-particle energies after $N=58$ with a maximal mixing at $N=60$. Also, since the differences of the 2^+ level energies are lowest at $N=58$, while the minimum for 0^+ level energy differences occurs at $N=60$, the structural exchange of the 2^+ levels takes place earlier than the one of 0^+ levels.
The characterization of the involved coexisting structures with different deformation in the transitional Zr isotopes, as well as the sudden rearrangement corresponding to a shape transition, is regarded in terms of the dynamics of $R_{4/2}$ ratios and $B(E2)$ values of low-lying ground state transitions, cp. figure 6.2(c). An $R_{4/2}$ ∼2 ratio associated with a spherical configuration, cp. section 2.2, can be found in the Zr isotopes up to incl. ^{98}Zr and a precipitate change to an $R_{4/2}$ ∼3.3 ratio, associated with a deformed configuration, at $A=100$ is observed. The now-measured $B(E2)$ value of ^{98}Zr allows to a establish a parallel discontinuity in the dynamics of the ground state transition strength and assign a low (if not vanishing) degree of collectivity (i.e., resembling single-particle excitation characteristics) to the ground state configuration. Hence, the Zr isotopic chain can be classified as (nearly) purely spherical in the ground state up to incl. $N=58$, and well-deformed at $N=60$ and onwards. The abruptness of the transition between the two configurations is strikingly evident in figure 6.1 (dashed-red line). This makes the structural change in the Zr chain the most rapid shape transition in the whole nuclear chart and, considering the analogy to general phase transitions introduced in chapter 2.4, ^{98}Zr the nucleus closest to the critical point of this transition.

6.3 Comparison to Theoretical Model Calculations

The n-rich Zr isotopes and their neighbours have been subject to profound theoretical studies within the IBM and mean-field approach [141, 142] resulting in the successful description of the shape evolution happening in this region. In this section, the obtained results are compared with state-of-the-art model calculations in terms of the shell model [143] and the recent large-scale Monte Carlo approach [29]. They both extend the valence space of former shell model studies performed for this region, that due to the need for truncations were not able to reliably predict the exact location of the shape transition's critical point.
The former work [143] stressed the importance of interplaying structures with different configurations; i.e. shape co-existence, in the change from spherical to deformed Zr nuclei. To allow such configuration mixing, as necessity for the proper description therefore a large model space was used. Consequently, a wide range of active orbitals was included in the calculations; i.e., for protons $\pi(1f_{5/2}, 2p_{1/2}, 2p_{3/2}$, and $1g_{9/2})$, and for neutrons $\nu(2d_{5/2}, 3s_{1/2}, 2d_{3/2}$, and $1g_{7/2})$. The nucleon-

nucleon interaction employed was based on adjustments to the CD-Bonn potential [144]. In particular, the neutrons interaction was corrected in the monopole part. To obtain electric transition rates, standard and artificially increased effective charges, as usual practice within this mass region [145, 146], were used. The results are depicted in figure 6.1. For the $B(E2; 2_1^+ \rightarrow 0_1^+)$ value of ^{98}Zr, 1.5 W. u., and 2.5 W. u., with the different effective charges respectively were calculated, which is in agreement with the result of this work. However, already the next isotopic neighbour ^{100}Zr could not be studied within the same model space, as again the required large model space exceeded computational limits. Since the transition was located to happen exactly between the two nuclei, the missing calculative deductions on ^{100}Zr impede the value of those theoretical studies for their employment within this work.

It is this limiting factor of truncated valence space that is directly tackled with the recent employment of quantum-Monte-Carlo diagonalization [40] in shell model calculations. Ref. [29] applied this extension of the classical shell model calculations explicitly to the shape transition case in the N=50-70 Zr region of interest. As effect, the model space could be extended to contain the $\pi(1g_{7/2}, 2d_{5/2}, 2d_{3/2}$, and $3s_{1/2})$ orbitals for protons, and the $\nu(1g_{9/2}, 1h_{11/2}, 2f_{7/2}$, and $3p_{3/2})$ orbitals for neutrons, additional to the space covered in the former studies. Consistently, one single Hamiltonian including adapted JUN45 and SNBG3 interactions [147, 148] was used for the whole region. As result, for the first time level energies and transition strength values of Zr^{90-110} were calculated within the same calculation. Those $B(E2)$ values are also depicted in figure 6.1, and a good agreement with experimental results can be diagnosed. Especially, and this sets these new calculations apart from previous theoretical work, the shape evolution is reproduced. For the $B(E2; 2_1^+ \rightarrow 0_{g.s.}^+)$ of ^{98}Zr a value of 2 W. u. was calculated. This is in very good agreement with what was measured in the frame of the experimental work presented.

The findings of the QMC-SM calculations of Togashi et al. [29] were explained in the frame of a type-II shell evolution (cp. section 2.3) in the Zr isotopic chain. This, and specifically the role of the examined ^{98}Zr in it, is covered in the following section.

6.4 Establishing the Critical Shape-Phase Transition Point in the Zr Isotopic Chain

Since $B(E2; 2_1^+ \rightarrow 0_1^+)$ values pose a sensitive probe to quadrupole collectivity, the obtained value for ^{98}Zr fills the gap for understanding the shape evolution taking place here. From the obtained low value, comparable to the one observed

in ^{96}Zr, a low collectivity of the ground state excitation, and, thus, a spherical ground state configuration can be deduced. Contrary to this, the deduced $B(E2;2_1^+ \rightarrow 0_2^+)=18^{+7}_{-5}$ W. u. makes the 2_1^+ level a collective excitation on top of the 0_2^+ level. This intruding level formation gains in collectivity and becomes the ground state structure in ^{100}Zr with $B(E2;2_1^+ \rightarrow 0_2^+)=75(5)$ W. u. This is accompanied by the excitation energy from the ground to the first excited 2^+ state dropping rapidly (from $N=58$ to $N=60$) from 1222 to 213 keV. The evolution of deformation parameters β_2 from Ref. [29] suggesting ^{98}Zr as least ground-state deformed nucleus in this structural change can be verified with this work's result. Conclusively, the evolution of ground-state deformation from spherical to well-deformed by addition of merely two neutrons established the shape transition in the Zr chain as most rapid in the nuclear chart. Considering the definition introduced in section 2.3, the systematics of $B(E2;2_1^+ \rightarrow 0_{g.s.}^+)$ values can be identified as signature of a well-pronounced first-order quantum phase transition with the phase discontinuously changing from spherical to deformed.

While this scenario of coexisting shapes within one nucleus located at the brink of a sudden shape alteration suggests a reasonable manifestation of the mechanism of type-II shape evolution (cp. section 2.5), the involved states' configurations have to be examined for a proper deduction of their physics origin. In figure 3 of ref. [29] (cp. figure 6.3) the calculated occupation numbers of the protons and the effective single-particle energies (SPEs) of involved neutrons of the 0^+ state configurations in ^{98,100}Zr are depicted. The proton occupation number similarity of the 0_2^+ state of ^{98}Zr and of the 0_1^+ state of ^{100}Zr is in line with the deformed character of the structure and its evolution into the ground state of ^{100}Zr. When connected with the neutron SPEs it becomes evident that the strong reconfiguration of involved proton orbitals is correlated to shifts in the corresponding neutron orbitals' SPEs. In ^{98}Zr this is the effect brought about by the type-II shell evolution: a self-reinforcing reorganization of proton and neutron orbitals by the reconfiguration of the nucleons occupying them. A crucial stress has to be put on the fact that those correlated effects take place as effect of a changing excitation energy within ^{98}Zr, i.e. by going from the ground state to the 0_2^+ state. Thus, the drastic shape change between ^{98}Zr and ^{100}Zr is based on this reconfiguration. The energetic lowering of $0g_{7/2}$ and $0h_{11/2}$ neutron orbitals in this reconfiguration is remarkably stronger than energy shifts observed for other orbitals and can be regarded as direct effect of the monopole part of the effective neutron-proton interaction [29] accompanying the alteration in proton occupation numbers. The resulting configuration with deformed character of the 0_2^+ level is verified by this work's result. Furthermore, the gain in deformation associated with protons occupying the $0g_{9/2}$ orbital, is in agreement with the deduced $B(E2;2_1^+ \rightarrow 0_2^+)$ value. However, with

$B(E2; 2_1^+ \rightarrow 0_2^+)$ ∼70 W. u. the collectivity predicted by the MC shell model calculations is comparably higher than the experimentally obtained result of ∼20 W. u. A viable explanation would be the mixing of different degrees between the configurations of the 0^+ levels. In ^{98}Zr a slightly stronger mixing than in ^{100}Zr, after the orbital exchange, would suppress the collective 2_1^+ excitation on top of the deformed 0_2^+. Also, a mixing between the 2^+ states can be considered as reason.
Thus, the shape transition in the Zr isotopic chain can be explained by type-II shape evolution with ^{98}Zr serving as nucleus closest to the critical transition point. As such, it is the first "critical" nucleus identified and it serves as best-visible example for this phenomenon so far.

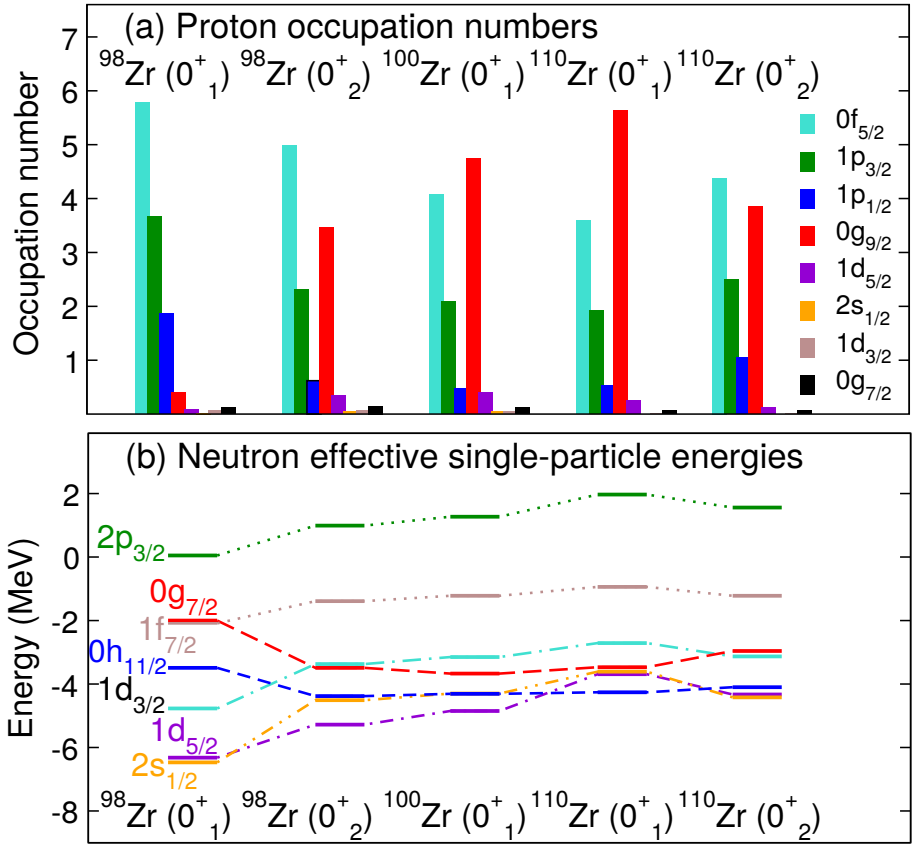

Figure 6.3.: Proton occupation numbers and neutron SPEs of the 0^+ states in ^{98,100}Zr. Taken from Ref. [29].

7 Conclusion & Outlook

To briefly grasp the scope of this thesis, in this last, closing, chapter, the content of this work is briefly repeated. Furthermore, this work's results are put into context of parallel or slightly time-delayed recent studies in this field. Additional implications that, for lack of time or the need for too many assumptions, were not studied, are mentioned, and can be regarded as outlook for further studies.

The interesting physics case of the nucleus ^{98}Zr was introduced in chapter 1 from a broader physics perspective and put into the specific nuclear structure physics context as given by the theory described in chapter 2. In particular, the topic of phase transitions and the transfer of their principles to nuclear shell evolution in finite quantum systems (cp. section 2.4) was found to relate back to the basics of nuclear force properties (cp. section 2.5). The combination of the predicted key role of the nucleus ^{98}Zr in the uniquely-pronounced nuclear shape transition, and the lack of experimental information on it, composed the motivation of this experimental work. The connecting link between the intriguing theoretical background and the results of the performed experiments was presented in the form of critical basic principles in chapter 3. The relevant techniques for such experimental studies were illuminated in chapter 4. In particular, the requirements on sophisticated equipment, i.e. detectors, were pointed out in this context. The application of the presented methods with such state-of-the-art equipment formed the main content of this work, i.e. the lifetime / transition strength measurements on ^{98}Zr (cp. chapter 5). To obtain information on the $B(E2; 2_1^+ \rightarrow 0_2^+)$ value a Coulomb excitation experiment with a radioactive ion beam, and a complimentary RDDS lifetime measurement experiment following a two-neutron transfer to the stable ^{96}Zr, were prepared, performed and analysed (cp. sections 5.1 and 5.2, respectively). The result was the first distinction on this decisive experimental input as presented in chapter 5.3. Conclusively, the nucleus ^{98}Zr was established as closest nucleus to the critical point in the predicted phase transition in Zr isotopes, cp. chapter 6.

The obtained experimental results were recently confirmed by other work [135] with additional, albeit interpretative, information on the underlying structures in ^{98}Zr. The predictions for this nucleus made in the theoretical work [29, 69] are validated by both, this work, and the recent results of [135]. The general picture of co-existing structures with different degrees of deformation and their formation as effect of type-II shell evolution is cemented. However, mentionable deviations from the predictions, in particular, the degree of collectivity of the found structures, give

rise to potential follow-up studies. Also, the mixing between the different structures, which can be deduced to be non-negligible from experiment [20, 135], is yet to be reproduced by theory, and needs more experimental work.
To further increase the understanding of the structural diversity caused by type-II shell evolution, which manifests in ^{98}Zr, additional experimental studies are required. The two-neutron transfer reaction producing ^{98}Zr, as employed in this work (cp. section 5.2) proved to populate the excited states up to the 4^+ at 2048 keV. Extending the lifetime information to shorter-lived levels, as intended by the DSAM part of this work's second experiment (cp. section 5.2), could not be performed in the frame of this thesis since the obtained γ-ray spectra showed to many contaminating transitions. However, a better cleanup of the spectra can be achieved by additional conditions on ion (i.e., reaction partners, here ^{16}O) detection, and higher quality of the target material (i.e., less oxidization). As all lifetimes measured in the RDDS studies of [135] are in the application range of DSAM, next to yet unmeasured lifetimes of shorter-lived levels, the improvement of the measured lifetimes' accuracy (down to the $\sim$ 10% systematic uncertainty of DSAM, cp. section 4.1) could be subject of a dedicated DSAM measurement. To directly access quadrupole moments for better judging on the quadrupole collectivity of the different structures, a multi-step Coulomb excitation, as e.g. performed in [77, 149], would be an idea worth considering. As can be seen in the challenging analysis of the performed Coulomb excitation experiment (cp. section 5.1), the separation and intensity of radioactive ion beams is a key requirement for this approach. Whether improvements of the employed CARIBU fission source at ANL to provide the $\sim$2 order of magnitude increase in peak over background for such multi-step Coulomb excitation studies on ^{98}Zr are sufficient can only be speculated. An alternative could be the production of the nucleus of interest by fusion-fission in (future) RIBFs [97]. Regarding the mixing of the structures found in ^{98}Zr, with the known $\rho(E0)$ values connecting the 0^+ levels, the determination of the difference in the bands' degrees of quadrupole deformation could help quantify the mixing (in the context introduced in [150]).
As is evident by the extent of the outlook incorporated in this section, experimental studies on the nucleus ^{98}Zr are far from exhausted. While establishing ^{98}Zr as pivotal manifestation of type-II shell-evolving nucleus was crucial for the theoretical frame on which this work was based, the implications are not (yet) fully understood. Developments in both, theory and experiment, can improve the understanding of the underlying phenomena. From the experimental point of view, also the shell-evolution in the neighbouring Sr isotopes, predicted within the same theoretical frame [151, 30], though presumably less-pronounced, is worth studying. Modifications to the existing theory describing this intriguing region of the

nuclear chart, e.g. to the Hamiltonian employed in the MCSM calculations [29], have to be performed for better reproduction of the experimental findings. Also the extension of type-II shell evolution to other regions of the nuclear chart might hold consequences of high impact. For instance, its effect on fission in (super) heavy nuclei can be put into (future) perspective, cp. [30].
The underlying mechanisms of shell evolution in the vicinity of (sub-) shell closures presumably also influence nuclear structure in exotic nuclei. Therefore, their understanding based on studies of experimentally accessible nuclei can be crucial for the theoretical access to the formation of new magic numbers in the terra incognita of the nuclear chart.

8 Acknowledgements

Die vorliegende Arbeit wäre ohne Beiträge einer ganzen Reihe von Leuten und ihrer Mitwirkung in verschiedenster Art und Weise in dieser Form nicht zu Stande gekommen. Diesen Personen möchte ich an dieser Stelle Dank und Lob für ihre Unterstützung aussprechen.
Names are abbreviated in this public version.

In erster Linie bedanke ich mich bei NP für die Aufnahme in die Arbeitsgruppe. Ihm und VW danke ich für die langjährige Betreuung und Unterstützung sowie die andauernde Motivation mit immer neuen Ideen. Insbesondere danke ich VW für seine ständige Präsenz (ausgenommen vormittags) und die vielen prägnanten Ratschläge und Diskussionen. Auch CS, der mich damals als Master-Studenten für die Kernphysik begeistert hat, verdient an dieser Stelle Anerkennung.
Der Büroalltag während der Promotion war häufig nicht annähernd so interessant wie die zugrundeliegende Wissenschaft. Umso mehr schätze ich die Kollegen, die mich während dieser Zeit begeleitet, mir unter die Arme gegriffen und/oder für Ablenkung gesorgt haben oder auch einfach für einen Plausch zur Verfügung standen. Vornehmlich gilt mein Dank meinem nächsten kollegialen Umfeld, den Bürokollegen vom IKP und der GSI: CL, ML und PK. Vielen Dank für die lockere Atmosphäre und den Spaß neben der Arbeit! Für die produktive und unterhaltsame Zusammenarbeit geht ein generelles Dankeschön an die gesamte Arbeitsgruppe des IKP und die Kernspektroskopie-Gruppe der GSI, sowie bestimmte Individuen der Graduiertenschule HGS-HIRe. Namentlich adressieren möchte ich zusätzlichen Dank an JW (für Antworten auf alle Fragen), RK (für die Beihilfe zum Fahraddiebstahl) und PN (für die schlechten Witze). Ich schätze mich glücklich, beim Promovieren auch den essenziellen Soft Skill des Kickerspielens erworben zu haben, und möchte hierfür ML, JI und den anderen Mitspielern die angebrachte Anerkennung aussprechen.
The experiments performed in the frame of this work could not have been conducted without the involvement of numerous collaborators.
I thank NM and his group at IFIN-HH for the energetic support in the RDDS experiment. In particular, the overtime work put into the difficult target production by AM, and the assisting correspondence with CN are appreciated. Regarding the CoulEx experiment, I acknowledge all contributors and the work of the ANL ATLAS team. I would like to express my gratitude to RJ for his vigorous contribution to

the paper manuscript.
Für das Korrekturlesen meiner Arbeit danke ich JW, ML, LM, PN, RK, NP und VW.
Nicht zuletzt möchte ich mich für die Unterstützung und den Zuspruch während der Promotion bei meiner Familie JW, SW und WW und insbesondere bei meiner Freundin LM bedanken.

The author acknowledges the funding of the German Federal Ministry of Education and Research (BMBF) within the NUSTAR R & D project (grant no. 05P15RDFN1) and the support of the Helmholtz Graduate School for Hadron and Ion Research (HGS-HIRe).

Bibliography

[1] D Richter et al. *The age of the hominin fossils from Jebel Irhoud, Morocco, and the origins of the Middle Stone Age*. In: *Nature* 546 (2017).

[2] C Singer. *A Short History of Science to the Nineteenth Century*. New York, NY: Oxford Univ. Press, 1942 (first publication).

[3] S Berryman. *Ancient Atomism*. In: *The Stanford Encyclopedia of Philosophy*. Ed. by Edward N. Zalta. Metaphysics Research Lab, Stanford University, 2016.

[4] A J Rocke. *Chemical Atomism in the Nineteenth Century*. Ohio State Univ. Press, 1984.

[5] B Pullmann. *The Atom in the History of Human Thought*. New York, NY: Oxford Univ. Press, 1998.

[6] W Demtroeder. *Experimentalphysik 3*. Springer Verlag, 2005.

[7] J Bienlein and R Wiesendanger. *Einfuehrung in die Struktur der Materie*. B. G. Teubner Verlag, 2003.

[8] G Fraser (ed.) *The Particle Century*. Institue of Physics Publishing Ltd., 1998.

[9] G D Coughlan, J E Dodd, and B M Gripaios. *The Ideas of Particle Physics: An Introduction for Scientists*. Cambridge University Press, 2006.

[10] K S Krane. *Introductory Nuclear Physics*. John Willey and Sons, Inc., 1988.

[11] S Weinberg. *Dream of a Final Theory: The Scientist's Search of the Ultimate Laws of Nature*. Knopf Doubleday Publishing Group, 2011.

[12] F Wilczek. *Quantum Chromodynamics: The Modern Theory of the Strong Interaction*. In: *Annual Review of Nuclear and Particle Science* 32 (2003).

[13] M J Savage. *Nuclear physics from lattice QCD*. In: *Progress in Particle and Nuclear Physics* 67.2 (2012).

[14] R Machleidt and I Slaus. *The nucleon-nucleon interaction*. In: *Journal of Physics G-nuclear and Particle Physics - J PHYS G-NUCL PARTICLE PHYS* 27 (2001).

[15] M Thoennessen. *Reaching the limits of nuclear stability*. In: *Reports on Progress in Physics* 67.7 (2004).

[16] B Pritychenko et al. *The Nuclear Science References (NSR) database and Web Retrieval System*. In: *Nucl. Instr. and Meth. in Phys. Res. A* 640.1 (2011).

[17] R F Casten. *Nuclear Structure from a Simple Perspective*. New York, NY: Oxford Univ. Press, 1990.

[18] M G Mayer. *Nuclear Configurations in the Spin-Orbit Coupling Model. I. Empirical Evidence*. In: *Phys. Rev.* 78 (1950).

[19] D Sorlin and M G Porquet. *Nuclear magic numbers: New features far from stability*. In: *Progress in Particle and Nuclear Physics* 61.2 (2008).

[20] W Witt et al. *Sub-shell closure and shape coexistence in the transitional nucleus* ^{98}Zr. In: *Phys. Rev. C* 98 (2018).

[21] C Crockett. *Synopsis: Changing the Shape of a Zirconium Nucleus*. In: *Phys. Rev. C* 98.4 (2018).

[22] C Eidemueller. *Sieht aus wie ein Rugbyball*. In: *Welt der Physik* (2018).

[23] S A E Johansson. *Gamma de-excitation of fission fragments: (II). Delayed radiation*. In: *Nuclear Physics* 64.1 (1965).

[24] J Eberth, R A Meyer, and K Sistemich (ed.) *Nuclear Structure of the Zirconium Region*. In: *Research Reports in Physics*. Springer Verlag, 1988.

[25] P Federman and S Pittel. *Towards a unified microscopic description of nuclear deformation*. In: *Physics Letters B* 69.4 (1977).

[26] P Cejnar, J Jolie, and R F Casten. *Quantum phase transitions in the shapes of atomic nuclei*. In: *Rev. Mod. Phys.* 82 (2010).

[27] B Singh and Z Hu. *Nuclear Data Sheets for A=98*. In: *Nuclear Data Sheets for A=98, Nucl. Data Sheets 98, 335* (2003).

[28] S Ansari et al. *Experimental study of the lifetime and phase transition in neutron-rich* ^{98,100,102}Zr. In: *Phys. Rev. C* 96 (2017).

[29] T Togashi et al. *Quantum Phase Transition in the Shape of Zr isotopes*. In: *Phys. Rev. Lett.* 117 (2016).

[30] T Otsuka, Y Tsunoda, T Togashi, et al. *Quantum self-organization and nuclear collectivities*. In: *Journal of Physics: Conference Series* 966.1 (2018).

[31] D Abriola and A A Sonzogni. *Nuclear Data Sheets for A = 94*. In: *Nuclear Data Sheets* 107.9 (2006).

[32] D Abriola and A A Sonzogni. *Nuclear Data Sheets for A = 96*. In: *Nuclear Data Sheets* 109.11 (2008).

[33] B Singh. *Nuclear Data Sheets for A = 100*. In: *Nuclear Data Sheets* 109.2 (2008).

[34] K L G Heyde. *The Nuclear Shell Model*. Springer Verlag, 1992.

[35] W M Elsasser. *Sur le principe de Pauli dans les noyaux*. In: *J. Phys. Radium* 4.10 (1933).

[36] G Audi. *The history of nuclidic masses and of their evaluation*. In: *International Journal of Mass Spectrometry* 251.2 (2006).

[37] K E Johnson. *Independent-particle models of the nucleus in the 1930s*. In: *American Journal of Physics* 60.2 (1992).

[38] I Kaplan. *The Pauli Exclusion Principle: Origin, Verifications, and Applications*. In: (2016).

[39] E Wigner, M Goeppert Mayer, and H Jensen. *From Nobel Lectures, Physics 1963-1970*. In: (1972).

[40] N Shimizu et al. *Monte Carlo shell model studies with massively parallel supercomputers*. In: *Physica Scripta* 92.6 (2017).

[41] T Otsuka. *Monte Carlo shell model*. In: *Nuclear Physics A* 693.1 (2001).

[42] S G Nilsson. *Binding States of Individual Nucleons in Strongly Deformed Nuclei*. In: *Det Kongelige Danske Videnskabernes Selskab, Matematisk-Fysiske Meddelelser* 29 (1955).

[43] A Bohr and B Mottelson. *Collective and Individual-particle Aspects of Nuclear Structure*. In: *Det Kongelige Danske Videnskabernes Selskab, Matematisk-Fysiske Meddelelser* 27.16 (1953).

[44] F Villars. *The Collective Model of Nuclei*. In: *Annual Review of Nuclear Science* 7.1 (1957).

[45] M Pi et al. *Time-dependent Thomas-Fermi approach to nuclear monopole oscillations*. In: *Physics Letters B* 166.1 (1986).

[46] J M Pearson. *The incompressibility of nuclear matter and the breathing mode*. In: *Physics Letters B* 271.1 (1991).

[47] S Shlomo, B K Agrawal, and V Au Kim. *Status of the nuclear matter equation of state as determined from compression modes*. In: *Nuclear Physics A* 734 (2004).

[48] M Goldhaber and E Teller. *On Nuclear Dipole Vibrations*. In: *Phys. Rev.* 74 (1948).

[49] J O Newton et al. *Observation of Giant Dipole Resonances Built on States of High Energy and Spin*. In: *Phys. Rev. Lett.* 46 (1981).

[50] D Savran, T Aumann, and A Zilges. *Experimental studies of the Pygmy Dipole Resonance*. In: *Progress in Particle and Nuclear Physics* 70 (2013).

[51] L Gaffney et al. *Studies of pear-shaped nuclei using accelerated radioactive beams*. In: *Nature* 497 (2013).

[52] D J Rowe. *Equations-of-Motion Method and the Extended Shell Model*. In: *Rev. Mod. Phys.* 40 (1968).

[53] A Arima and F Iachello. *The Interacting Boson Model*. In: *Annual Review of Nuclear and Particle Science* 31.1 (1981).

[54] J P Draayer and J Jänecke. *Group Theory and Special Symmetries in Nuclear Physics*. In: *Group Theory and Special Symmetries in Nuclear Physics*. 1992.

[55] R F Casten. *Shape phase transitions and critical-point phenomena in atomic nuclei*. In: *Nature Physics* 2 (2006).

[56] F Iachello. *Dynamic Symmetries at the Critical Point*. In: *Phys. Rev. Lett.* 85 (2000).

[57] F Iachello. *Analytic Description of Critical Point Nuclei in a Spherical-Axially Deformed Shape Phase Transition*. In: *Phys. Rev. Lett.* 87 (2001).

[58] N Pietralla and O M Gorbachenko. *Evolution of the "β excitation" in axially symmetric transitional nuclei*. In: *Phys. Rev. C* 70 (2004).

[59] D W Oxtoby et al. *Principles of Modern Chemistry*. Thomson/Brooks/Cole, 2008.

[60] Gregg Jaeger. *The Ehrenfest Classification of Phase Transitions: Introduction and Evolution*. In: *Archive for History of Exact Sciences* 53.1 (1998).

[61] F Fillaux. *The quantum phase-transitions of water*. In: *EPL (Europhysics Letters)* 119.4 (2017).

[62] E Williams, R J Casperson, and V Werner. *Effective critical points in finite quantum phase transitional systems*. In: *Phys. Rev. C* 82 (2010).

[63] V Werner et al. *Singular Character of Critical Points in Nuclei*. In: *Physics Letters B* 527 (2001).

[64] J L Wood and K Heyde. *A focus on shape coexistence in nuclei*. In: *Journal of Physics G: Nuclear and Particle Physics* 43.2 (2016).

[65] R Budaca and A I Budaca. *Coexistence, mixing and fluctuation of nuclear shapes*. In: *EPL (Europhysics Letters)* 123.4 (2018).

[66] C Kremer et al. *First Measurement of Collectivity of Coexisting Shapes Based on Type II Shell Evolution: The Case of ^{96}Zr*. In: *Phys. Rev. Lett.* 117 (2016).

[67] K Heyde et al. *Phase transitions versus shape coexistence*. In: *Phys. Rev. C* 69 (2004).

[68] K Heyde and J L Wood. *Shape coexistence in atomic nuclei*. In: *Rev. Mod. Phys.* 83 (2011).

[69] T Otsuka and Y Tsunoda. *The role of shell evolution in shape coexistence*. In: *Journal of Physics G: Nuclear and Particle Physics* 43.2 (2016).

[70] T Otsuka et al. *Evolution of Nuclear Shells due to the Tensor Force*. In: *Phys. Rev. Lett.* 95 (2005).

[71] J Suhonen. *From Nucleons to Nucleons - Concepts of Microscopic Nuclear Theory*. Springer Verlag, 2007.

[72] D S Pressyanov. *Short Solution of the Radioactive Decay Chain Equations*. In: *American Journal of Physics* 444.70 (2002).

[73] K Alder et al. *Study of Nuclear Structure by Electromagnetic Excitation with Accelerated Ions*. In: *Rev. Mod. Phys.* 28 (1956).

[74] D Cline. *Nuclear Shapes Studied by Coulomb Excitation*. In: *Annual Review of Nuclear and Particle Science* 36.1 (1986).

[75] A Winther and K Alder. *Relativistic coulomb excitation*. In: *Nuclear Physics A* 319.3 (1979).

[76] H Ower et al. *Computer program CLX*. In: *Computer program CLX, PhD Thesis Goethe university of Frankfurt am Main* (original 1980).

[77] D Czosnyka et al. *Computer program GOSIA*. In: *Bull. Am. Phys. Soc.* 28.745 (1983).

[78] M Zielinska et al. *Analysis methods of safe Coulomb-excitation experiments with radioactive ion beams using the GOSIA code*. In: *The European Physical Journal A* 52.4 (2016).

[79] P J Nolan and J F Sharpey-Schafer. *REVIEW: The measurement of the life-times of excited nuclear states*. In: *Reports on Progress in Physics* 42 (1979).

[80] I Y Lee, M A Deleplanque, and K Vetter. *Developments in large gamma-ray detector arrays*. In: *Reports on Progress in Physics* 66.7 (2003).

[81] G F Knoll. *Radiation Detection and Measurement*. John Willey and Sons, 2010.

[82] W R Leo. *Techniques for Nuclear and Particle Physics Experiments*. Springer Science and Business Media, 2012.

[83] M Moszyński and H Mach. *A method for picosecond lifetime measurements for neutron-rich nuclei: (2) Timing study with scintillation counters*. In: *Nuclear Instruments and Methods in Physics Research Section A: Accelerators, Spectrometers, Detectors and Associated Equipment* 277.2 (1989).

[84] H Mach, R L Gill, and M Moszyński. *A method for picosecond lifetime measurements for neutron-rich nuclei: (1) Outline of the method*. In: *Nuclear Instruments and Methods in Physics Research Section A: Accelerators, Spectrometers, Detectors and Associated Equipment* 280.1 (1989).

[85] U Kneissl, H H Pitz, and A Zilges. *Investigation of nuclear structure by resonance fluorescence scattering*. In: *Progress in Particle and Nuclear Physics* 37 (1996).

[86] D Meschede. *Gerthsen Physik (23. Aufl.)* Springer Verlag, 2006.

[87] D G Ghita. *Electronic Techniques in Timing Measurements for Nuclear Structure*. In: *U. P. B. Sci. Bull., Series A* 70 (2008).

[88] J-M Régis et al. *The generalized centroid difference method for picosecond sensitive determination of lifetimes of nuclear excited states using large fast-timing arrays*. In: *Nuclear Instruments and Methods in Physics Research Section A Accelerators Spectrometers Detectors and Associated Equipment* 726 (2013).

[89] M Nakhostin, Zs Podolyak, and P Regan. *Digital processing of signals from LaBr 3 :Ce scintillation detectors*. In: *Journal of Instrumentation* 9 (2014).

[90] J-M Régis. *Fast Timing with LaBr 3 (Ce) Scintillators and the Mirror Symmetric Centroid Difference Method*. PhD thesis. 2011.

[91] P Regan et al. *Precision Lifetime Measurements Using LaBr3 Detectors With Stable and Radioactive Beams*. In: vol. 63. 2013.

[92] A Dewald, O Möller, and P Petkov. *Developing the Recoil Distance Doppler-Shift technique towards a versatile tool for lifetime measurements of excited nuclear states*. In: *Progress in Particle and Nuclear Physics* 67 (2012).

[93] A Dewald, S Harissopulos, and P von Brentano. *The differential plunger and the differential decay curve method for the analysis of recoil distance Doppler-shift data*. In: *Zeitschrift für Physik A Atomic Nuclei* 334.2 (1989).

[94] T K Alexander and J S Forster. *Lifetime Measurements of Excited Nuclear Levels by Doppler-Shift Methods*. In: *Advances in Nuclear Physics: Volume 10*. Ed. by Michel Baranger and Erich Vogt. Boston, MA: Springer US, 1978.

[95] C Stahl. *New methods for the γ-ray spectroscopy with position-sensitive detector systems*. PhD thesis. Darmstadt: Technische Universität, 2015.

[96] J Ziegler, M D Ziegler, and J P Biersack. *The Stopping and Range of Ions in Mater*. In: *Nuclear Instruments and Methods in Physics Research Section B: Beam Interactions with Materials and Atoms* 268 (2010).

[97] Y Blumenfeld, T Nilsson, and P Van Duppen. *Facilities and methods for radioactive ion beam production*. In: *Physica Scripta* T152 (2013).

[98] National Research Council. *Scientific Opportunities with a Rare-Isotope Facility in the United States*. Washington, DC: The National Academies Press, 2007.

[99] A N Andreyev, K Nishio, and K-H Schmidt. *Nuclear fission: a review of experimental advances and phenomenology*. In: *Reports on Progress in Physics* 81.1 (2018).

[100] V V Volkov. *Deep inelastic transfer reactions — The new type of reactions between complex nuclei*. In: *Physics Reports* 44.2 (1978).

[101] L Corradi et al. *Multinucleon transfer reactions: Present status and perspectives*. In: *Nuclear Instruments and Methods in Physics Research Section B: Beam Interactions with Materials and Atoms* 317 (2013).

[102] J J Valiente-Dobón. *Gamma-Ray Spectroscopy of Neutron-Rich Nuclei Populated via Multinucleon-Transfer Reactions*. In: *Basic Concepts in Nuclear Physics: Theory, Experiments and Applications*. Ed. by José-Enrique García-Ramos et al. Cham: Springer International Publishing, 2016.

[103] J Wiederhold et al. *Signatures for a nuclear quantum phase transition from E 0 and E 2 observables in Gd isotopes*. In: *Journal of Physics: Conference Series* 1023 (2018).

[104] F L Bello Garrote et al. *Lifetime measurements in Nd 138*. In: *Physical Review C* 97 (2018).

[105] U. S. Department of Energy Office of Science. *ATLAS floorplan*. URL: `https://www.phy.anl.gov/atlas/facility/floorplan.html` (visited on 01/09/2019).

[106] R Janssens. *The Atlas facility*. 2010. URL: `http://www.scholarpedia.org/article/The_ATLAS_facility` (visited on 01/09/2019).

[107] W Henning. *The ATLAS facility at argonne national laboratory*. In: *Nuclear Physics News* 5 (1995).

[108] N Pietralla et al. *Coulomb excitation of the 2^+_{ms} state of ^{96}Ru in inverse kinematics*. In: *Phys. Rev. C* 64 (2001).

[109] G Savard et al. *CARIBU: a new facility for the study of neutron-rich isotopes*. In: *Hyperfine Interactions* 199.1 (2011).

[110] R C Pardo, G Savard, and R V F Janssens. *ATLAS with CARIBU: A Laboratory Portrait*. In: *Nuclear Physics News* 26.1 (2016).

[111] P Fallon, A Gade, and I-Y Lee. *GRETINA and Its Early Science*. In: *Annual Review of Nuclear and Particle Science* 66.1 (2016).

[112] D Doherty et al. *Triaxiality near the 110Ru ground state from Coulomb excitation*. In: *Physics Letters B* 766 (2017).

[113] S Paschalis et al. *The performance of the Gamma-Ray Energy Tracking In-beam Nuclear Array GRETINA*. In: *Nucl. Instr. and Meth. in Phys. Res. A* 709.Supplement C (2013).

[114] M Cromaz. *The GRETINA Spectrometer*. In: *Journal of Physics: Conference Series* 606.1 (2015).

[115] I Y Lee, M A Deleplanque, and K Vetter. *Developments in large gamma-ray detector arrays*. In: *Reports on Progress in Physics* 66.7 (2003).

[116] M A Riley, J Simpson, and E S Paul. *High resolution gamma-ray spectroscopy and the fascinating angular momentum realm of the atomic nucleus*. In: *Physica Scripta* 91.12 (2016).

[117] P Preuss. *GRETINA moves into its new Cave*. 2010. URL: `https://newscenter.lbl.gov/2010/11/12/gretina-cave/` (visited on 01/09/2019).

[118] C Y Wu et al. *CHICO2, a two-dimensional pixelated parallel-plate avalanche counter*. In: *Nucl. Instr. and Meth. in Phys. Res. A* 814.Supplement C (2016).

[119] H Kumagai et al. *Development of Parallel Plate Avalanche Counter (PPAC) for BigRIPS fragment separator*. In: *Nuclear Instruments and Methods in Physics Research Section B: Beam Interactions with Materials and Atoms* 317 (2013).

[120] LLNL-Rochester CHICO2 collaboration. *CHICO-II; a 4pi heavy-ion detector*. In: *GRETINA Meeting, ANL* (2013).

[121] T R England and B F Rider. *Evaluation and Compilation of Fission Yields*. In: *Evaluation and Compilation of Fission Yields, ENDF-349, LA-UR-94-3106* ENDF-349, LA-UR-94-3106 (1994).

[122] G Savard and R Pardo. *Proposal for the 252Cf source upgrade to the ATLAS facility*. In: *Proposal for the 252Cf source upgrade to the ATLAS facility, Technical report, ANL* (2005).

[123] Nuclear Physics Dpt. IFIN-HH and Tandem Accelerator Dpt. *9 MV FN Pelletron Tandem Accelerator*. URL: https://tandem.nipne.ro/9MV_Pelletron.php (visited on 01/09/2019).

[124] S Dobrescu et al. *The Bucharest FN Tandem Accelerator: Modernization and Development*. In: *AIP Conference Proceedings* 1099 (2009).

[125] Inc. Encyclopaedia Britannica. *Tandem Accelerator*. URL: https://www.britannica.com/technology/tandem-accelerator/media/582236/3083 (visited on 01/09/2019).

[126] D Bucurescu et al. *The ROSPHERE gamma-ray spectroscopy array*. In: *Nuclear Instruments and Methods in Physics Research Section A: Accelerators, Spectrometers, Detectors and Associated Equipment* 837 (2016).

[127] Nuclear Physics Dpt. IFIN-HH and Tandem Accelerator Dpt. *Nuclear Structure - The ROSPHERE gamma-ray Spectroscopy Array*. URL: http://www.nipne.ro/facilities/facilities/tandem.php (visited on 01/09/2019).

[128] O Moeller. *Test der X(5)-Symmetrie in 156Dy und 178Os durch Messung elektromagnetischer Übergangswahrscheinlichkeiten*. PhD thesis. Cologne: University of Cologne, 2005.

[129] M H Macfarlane and S C Pieper. *PTOLOMY - A Program for Heavy-ion Direct-reaction Calculations (original version)*. In: *ANL-76-11 Rev. 1 Mathematics and Computers* (1978).

[130] N Marginean. *PTOLEMY Kinematics Calculations*. Private Communication. 2017.

[131] F Pühlhofer. *On the interpretation of evaporation residue mass distributions in heavy-ion induced fusion reactions*. In: *Nuclear Physics A* 280.1 (1977).

[132] V Werner, W Witt, et al. *Shape-Phase Transtion at Zr-98*. (Accepted) Experimental Proposal to IFIN-HH PAC 2017. 2017.

[133] R Kern. *CLX Cross-Section Calculations*. Private Communication. 2018.

[134] G Gürdal and F G Kondev. *Nuclear Data Sheets for A = 110*. In: *Nuclear Data Sheets* 113.5 (2012).

[135] P Singh et al. *Evidence for Coexisting Shapes through Lifetime Measurements in* ^{98}Zr. In: *Phys. Rev. Lett.* 121 (2018).

[136] E Browne. *Nuclear Data Sheets for A = 90*. In: *Nuclear Data Sheets* 82.3 (1997).

[137] C M Baglin. *Nuclear Data Sheets for A = 92*. In: *Nuclear Data Sheets* 113.10 (2012).

[138] D De Frenne. *Nuclear Data Sheets for A = 102*. In: *Nuclear Data Sheets* 110.8 (2009).

[139] J Blachot. *Nuclear Data Sheets for A = 104*. In: *Nuclear Data Sheets* 108.10 (2007).

[140] D De Frenne and A Negret. *Nuclear Data Sheets for A = 106*. In: *Nuclear Data Sheets* 109.4 (2008).

[141] K Nomura, R Rodríguez-Guzmán, and L M Robledo. *Structural evolution in A ≈ 100 nuclei within the mapped interacting boson model based on the Gogny energy density functional*. In: *Phys. Rev. C* 94 (2016).

[142] H Abusara and S Ahmad. *Shape evolution in Kr, Zr, and Sr isotopic chains in covariant density functional theory*. In: *Phys. Rev. C* 96 (2017).

[143] K Sieja et al. *Shell model description of zirconium isotopes*. In: *Phys. Rev. C* 79 (2009).

[144] R Machleidt. *High-precision, charge-dependent Bonn nucleon-nucleon potential*. In: *Phys. Rev. C* 63 (2001).

[145] C Fransen et al. *Investigation of low-spin states in ^{92}Zr with the $(n, n'\gamma)$ reaction*. In: *Phys. Rev. C* 71 (2005).

[146] A F Lisetskiy et al. *Shell model description of "mixed-symmetry" states in 94Mo*. In: *Nuclear Physics A* 677.1 (2000).

[147] M Honma et al. *New effective interaction for f_5pg_9-shell nuclei*. In: *Phys. Rev. C* 80 (2009).

[148] T Otsuka et al. *Novel Features of Nuclear Forces and Shell Evolution in Exotic Nuclei*. In: *Phys. Rev. Lett.* 104 (2010).

[149] Christopher Bauer et al. *Level lifetimes and quadrupole moments from Coulomb excitation in the Ba chain and the N = 80 isotones*. In: *EPJ Web of Conferences* 38 (2012).

[150] J L Wood et al. *Electric monopole transitions from low energy excitations in nuclei*. In: *Nuclear Physics A* 651.4 (1999).

[151] T Otsuka et al. *Novel Features of Nuclear Forces and Shell Evolution in Exotic Nuclei*. In: *Phys. Rev. Lett.* 104 (2010).

[152] H Xiaolong. *Nuclear Data Sheets for A = 196*. In: *Nuclear Data Sheets* 108.6 (2007).

[153] S Sjue. *Two-Body Kinematics Calculator and Plotter*. URL: https://skisickness.com/2010/04/21/ (visited on 01/09/2019).

Appendices

A Auxiliary Information on Analysis

A.1 CARIBU Beam Analysis Calculations

Decay chain of interest:

^{98}Sr $\rightarrow$ ^{98}Y $\rightarrow$ ^{98}Zr $\rightarrow$ ^{98}Nb $\rightarrow$ ^{98}Mo (stable)

Isotope intensity determination:

Isotope	Identifying γ-Transition	Energy (keV)	$\frac{I_\gamma}{I_{\gamma,total}}$	Intensity (pps)
^{98}Sr	^{98}Y: $(1, 2)^-_{564} \rightarrow (1^-)_{119}$	445	0.39(4)	102
^{98}Sr	^{98}Y: $(1)^+_{548} \rightarrow (1^-)_{119}$	429	0.31(3)	117
^{98}Y	^{98}Zr: $2^+_{1744} \rightarrow 0^+_{g.s.}$	1744	0.054(3)	272(21)
^{98}Y^m	^{98}Zr: $(4^+)_{1843} \rightarrow 2^+_{1222}$	621	0.63(3)	214(18)
^{98}Zr	^{98}Mo: $2^+_{787} \rightarrow 0^+_{g.s.}$	787		591(30)*
^{98}Nb	^{98}Mo: $2^+_{787} \rightarrow 0^+_{g.s.}$	787	13	591(30)*
^{98}Nb^m	^{98}Mo: $2^+_{787} \rightarrow 0^+_{g.s.}$	787	93	591(30)*
^{98}Nb^m	^{98}Mo: $4^+_{1510} \rightarrow 2^+_{787}$	723	74(15)	<5

Table A.1.: Isotope intensities in the beam.

*: All nuclei of the decay chain decay though the $2^+_{787} \rightarrow 0^+_{g.s.}$ transition of ^{98}Mo, given is the total intensity of this transition.

Intensities from mother-nuclei are subtracted to gain the isotope intensities in the beam:
^{98}Sr: 113(9) pps (from average of identifying transition intensities)
^{98}Y: 159(23) pps (subtracted ^{98}Sr intensity)

$^{98}Y^{m}$: 101(20) pps (subtracted ^{98}Sr intensity)
^{98}Zr + ^{98}Nb + $^{98}Nb^{m}$: 218(44) pps (subtracted intensities of ^{98}Sr, ^{98}Y and $^{98}Y^{m}$)

From Cf fission yield division of isomeric state to total amount of ^{98}Nb $\frac{I(^{98}Nb^{m})}{I(^{98}Nb^{m})+I(^{98}Nb)} = 0.15$ [121], and $I(^{98}Nb^{m})$<5 pps:
$^{98}Nb^{m}$: <5 pps
^{98}Nb: <30 pps
^{98}Zr: >183(21) pps (subtracting $^{98}Nb^{m}$, ^{98}Nb)

The calculations result in a minimum of 162 pps of ^{98}Zr in the beam.

A.2 CLX Calculations for CoulEx Experiment at ANL

Input files for target and beam (^{98}Zr and ^{98}Mo) are given at the end of this section. The respective CLX output is not given here, due to length. The cross-sections for Coulomb excitation yields σ (decays after excitation) of separate nuclear states included in it are used in the following way:
With $\sigma(^{196}\text{Pt})$: CLX cross-section for $2_1^+ \rightarrow 0_{g.s.}^+$ of ^{196}Pt; $\sigma(^{98}\text{Mo})$: CLX cross-section for $2_1^+ \rightarrow 0_{g.s.}^+$ of ^{98}Mo; $\sigma(^{98}\text{Zr})$: CLX cross-section for $2_1^+ \rightarrow 0_{g.s.}^+$ of ^{98}Zr:

- Integrate $2_1^+ \rightarrow 0_{g.s.}^+$ of transition peak ^{196}Pt at 356 keV in GRETINA γ-ray spectrum (Doppler-corrected for target ions) $\rightarrow I_{Pt}$
- Integrate $2_1^+ \rightarrow 0_{g.s.}^+$ of transition peak ^{98}Mo at 735 keV in GRETINA γ-ray spectrum (Doppler-corrected for beam ions) $\rightarrow I_{Mo}$
- Calculate target transition yield to be attributed to unstable beam ions employing CoulEx cross section proportionality for E2 transitions (cp. section 3.2):
$I_{Pt,unst} = I_{Pt} - I_{Mo} \cdot \frac{\sigma(^{98}Mo)}{\sigma(^{196}Pt)}$
- Subtract target excitation yield according to beam composition (cp. section 5.1.2) to obtain target excitation yield attributable to ^{98}Zr reactions:

$I_{Pt,Zr} = I_{Pt,unst} \cdot \frac{Int(^{98}Zr)}{Int(^{98}Sr)+Int(^{98}Y)+Int(^{98}Y^m)+Int(^{98}Nb)+Int(^{98}Nb^m)}$,
with $Int(^AX^{[m]})$: beam intensity of respective nucleus $^AX^{(isomer)}$.
- Calculate $\sigma(^{98}Zr)$ (function of $B[E2; 2_1^+ \rightarrow 0_{g.s.}]$ value in CLX input file) according to relative yields and excitation cross sections:
$\sigma(^{98}Zr) = \sigma(^{196}Pt) \cdot \frac{I_{Zr}}{I_{Pt,Zr}}$ (*)

From $\sigma(^{98}Zr)$ the $B(E2; 2_1^+ \rightarrow 0_{g.s.})$ value of ^{98}Zr is obtained from CLX. It depends directly on the amount of observed ^{98}Zr $2_1^+ \rightarrow 0_{g.s.}$ transition yield.
For $I_{Zr} \cdot \varepsilon_{1222keV} = 40$ (upper limit for $2_1^+ \rightarrow 0_{g.s.}$ transitions of ^{98}Zr in the spectrum, cp. section 5.1.3) above equation (*) is true for $B(E2; 2_1^+ \rightarrow 0_{g.s.}) = 8.9(20)$ W. u., with the uncertainty stemming from uncertainties in beam compositions $\Delta Int(^AX)$. Uncertainties in CLX calculation, transition peak integration fits, and CLX input parameters (from [27, 152]) are negligible.
From above value and its uncertainty follows the upper limit:
$B(E2; 2_1^+ \rightarrow 0_{g.s.}) < 11$ W. u.

CLX Input file for target (^{196}Pt) excitations:

98Zr -> Pt @464.12 MeV
11101111
13 2 4.
0. 0. 0.
40 98
78 196
464.12
0.001 90. 1

1 0 0.0 1 0
2 2 0.356 1 0
3 2 0.689 1 0
4 4 0.877 1 0
5 3 1.015 1 0
6 0 1.135 1 0

7 5 1.270 -1 0
8 4 1.293 1 0
9 2 1.361 1 0
10 7 1.373 -1 0
11 0 1.402 1 0
12 3 1.447 -1 0
13 6 1.525 1 0

1 1 0 2 0.0

2 1 1.1697 2 0.0
2 2 0.82 2 0.0

3 2 1.36 2 0.0
3 3 -0.52 2 0.0

4 2 1.91 2 0.0
4 4 1.36 2 0.0
4 1 -0.11 4 0.0

6 2 0.167 2 0.0
6 3 -0.35 2 0.0

8 4 0.87 2 0.0
8 3 1.28 2 0.0
8 2 0.11 2 0.0
8 8 -0.34 2 0.0

13 13 -0.26 2 0.0

13 4 2.42 2 0.0

CLX Input file for unstable beam (^{98}Zr) excitations:

98Zr -> Pt @464.12 MeV
11101111
8 2 4.
0. 0. 0.
78 98
40 196
464.12
12 85. 2
1 0 0.0 1 0
2 0 0.854 1 0
3 2 1.223 1 0
4 0 1.436 1 0
5 2 1.591 1 0
6 2 1.744 1 0
7 3 1.806 -1 0
8 4 1.843 1 0

1 1 0 2 0.0

3 1 0.36632 2 0.0

8 3 0.51546 2 0.0

4 3 0.36997 2 0.0

5 1 0.20064 2 0.0

6 1 0.20064 2 0.0

7 3 2.18988 1 0.0

CLX Input file for stable beam (^{98}Mo) excitations:

98Mo -> Pt @464.12 MeV
11101111

8 2 4.
0. 0. 0.
78 98
42 196
464.12
12 85. 2
1 0 0.0 1 0
2 0 0.735 1 0
3 2 0.787 1 0
4 2 1.432 1 0
5 4 1.510 1 0
6 2 1.758 1 0
7 0 1.963 1 0
8 3 2.018 -1 0

1 1 0 2 0.0

3 1 0.526 2 0.0
3 2 0.36 2 0.0
3 3 -0.06 2 0.0

4 1 0.123 2 0.0
4 2 0.251 2 0.0
4 3 0.25 2 0.0
4 4 -0.025 2 0.0

5 3 1.01 2 0.0
5 4 -0.30 2 0.0
5 5 -0.43 2 0.0

6 1 -0.021 2 0.0
6 2 0.311 2 0.0
6 3 0.12 2 0.0
6 4 -1.51 2 0.0
6 5 0.593 2 0.0

6 6 -0.30 2 0.0

8 3 1.2823 1 0.0

A.3 CASCADE Cross Section Calculations

Cross-section calculations for fusion-evaporation reactions performed with CASCADE [131] for the experiment described in section 5.2; cross-sections given in units of mb:

Target: ^{96}Zr, Projectile: ^{16}O, V_{Coul}: 49.9 MeV

Nucleus	Channel	49 MeV	50 Mev	51 MeV
^{110}Cd	2n	0	0.01	0.14
^{109}Cd	3n	7.50	19.72	37.20
^{108}Cd	4n	7.10	21.56	46.77
^{110}Ag	np	0	0	0
^{109}Ag	2np	0.42	1.93	4.18
^{108}Ag	3np	0	0.30	0.98
^{107}Pd	nα	0	0	0
^{106}Pd	2nα	0.14	0.96	2.44
^{105}Pd	3nα	0	0	0.18

Table A.2.: CASCADE FE cross-section calculations: ^{96}Zr-^{16}O.

Target: ^{96}Zr, Projectile: ^{18}O, V_{Coul}: 50.3 MeV

Nucleus	Channel	49 MeV	50 Mev	51 MeV
^{111}Cd	3n	1.82	5.24	9.69
^{110}Cd	4n	10.09	32.16	72.95
^{111}Ag	2np	0	0.39	0.81
^{110}Ag	3np	0	0.59	1.90
^{108}Pd	2nα	0	0.29	0.82
^{107}Pd	3nα	0	0.25	0.79

Table A.3.: CASCADE FE cross-section calculations: ^{96}Zr-^{18}O.

Target: ^{16}O, Projectile: ^{16}O, V_{Coul}: 21.1 MeV

Nucleus	Channel	49 MeV	50 Mev	51 MeV
^{31}S	n	9.09	6.96	5.15
^{30}S	2n	0	0	0.24
^{31}P	p	37.18	29.21	22.26
^{30}P	np	208.45	210.27	204.91
^{29}P	2np	0	0	0
^{30}Si	2p	154.86	144.04	131.56
^{29}Si	n2p	24.50	38.04	54.94
^{28}Si	α	57.12	55.20	55.99
^{28}Si	2n2p	0	0	0
^{27}Si	nα	3.17	5.79	9.88
^{29}Al	3p	0	0	0
^{27}Al	pα	257.43	291.31	328.56
^{26}Al	npα	0	0	0
^{26}Mg	2pα	0	0.49	1.42
^{24}Mg	2α	37.59	45.10	54.24

Table A.4.: CASCADE FE cross-section calculations: ^{16}O-^{16}O.

Target: ^{18}O, Projectile: ^{16}O, V_{Coul}: 22.2 MeV

Nucleus	Channel	49 MeV	50 Mev	51 MeV
^{33}S	n	3.23	2.50	1.89
^{32}S	2n	35.33	30.46	26.61
^{33}P	p	3.02	2.28	1.70
^{32}P	np	181.54	171.13	152.83
^{31}P	2np	125.81	147.73	175.97
^{32}Si	2p	6.37	5.66	5.24
^{31}Si	n2p	12.14	17.21	20.89
^{30}Si	α	5.40	5.01	4.89
^{30}Si	2n2p	0	0	1.42
^{29}Si	nα	227.18	229.94	246.46
^{28}Si	2nα	129.91	161.65	164.43
^{29}Al	pα	26.63	32.36	37.35
^{28}Al	npα	6.39	6.64	11.70
^{26}Mg	2α	11.05	13.82	16.55
^{25}Mg	n2α	1.14	2.43	4.58

Table A.5.: CASCADE FE cross-section calculations: ^{18}O-^{16}O.

A.4 RDDS Recoil Velocity Estimate

Starting with the reaction ^{96}Zr(^{18}O, ^{16}O)^{98}Zr with a beam (^{18}O) energy of 49 MeV and a target thickness of 1 mg/cm^2:
- Assuming reaction in the target center, subtract beam energy loss due to electr. stopping at 40-50 MeV: 3 MeV/(mg/cm^2) [96] → $E_{beam,eff.}$=47.5 MeV
- Calculate maximum recoil (^{98}Zr) energy E in relativistic two-body kinematics, e.g. [153]: E=21.6 MeV; including excitations of 4 MeV for ejectile (^{16}O) and recoil each
- Subtract recoil energy loss due to electr. stopping at 15-22.8 MeV: 11.1 MeV/(mg/cm^2) [96] → $E_{recoil,max}$=16 MeV
- Average recoil energy after leaving the target:
$E_{recoil} = (0 + E_{recoil,max})/2$=8 MeV
- Calculate corresponding recoil velocity v: E_{recoil}=8 → v_{recoil}=1.1(1)%c (incl. 10% uncertainty for stopping power)

Similar for different values of target thickness. Note: no linear scaling between recoil velocity after target and target thickness (less stopping distance but higher energy loss/distance as higher energy).

A.5 CLX Input File for RDDS Experiment Cross-Section Calculations

CLX input file:

```
18O@197 @ IFIN-HH !Title
11101111 4 0 3 !Max states inv-0-Max Value of Magnetic N
0. 0. 0. !Accuracy parameters
8 18 !projectile Z projectile A
79 197 !target Z target A
47 !Average beam energy (target thickness)
1 180 10 !Starting anlge-stopping,step in cm sys
1 1.5 0.0 1 0 !Levels-Spin-energy(mev)-Paritiy
2 0.5 0.077 1 0
3 1.5 0.269 1 0
4 2.5 0.279 1 0

1 2 0.69 2
1 3 0.72 2
1 4 1.03 2
2 3 0.701 2
2 4 0.767 2
```

Calculations performed by R. Kern [133] with the following results:

cross sections in mbarn (level,x-sec,delta x-sec):

(2, 51.00710473, 4.452130553311597)
(3, 43.54191659999999, 4.8306706607820455)
(4, 87.36523977, 20.260912835666296)

A.6 Additional Material (RDDS Experiment)

Energy calibration (file) for HPGe detectors:

Obtained by fitting a polynomial of degree n to channel number c_i corresponding to calibration source (^{152}Eu) transition energies E_i, so that $E(c) = p_1 c^0 + p_2 c^1 + ... p_n c^{n-1}$.

(# of parameters, Det. #, n, p_1, p_2, ..., p_n)

7 0 5 -10.360 0.377585 -0.280603E-05 0.564613E-09 -0.386708E-13
7 1 5 -10.263 0.376551 -0.228347E-05 0.439116E-09 -0.290689E-13
7 2 5 -12.127 0.376332 -0.139839E-05 0.265800E-09 -0.175921E-13
7 3 5 -13.618 0.376001 -0.117284E-05 0.197325E-09 -0.119259E-13
7 4 5 -12.402 0.375546 -0.130507E-05 0.235675E-09 -0.150114E-13
7 5 5 -8.823 0.377979 -0.458086E-05 0.150059E-08 -0.237693E-12
7 6 5 -11.238 0.378513 -0.279250E-05 0.552487E-09 -0.371193E-13
7 7 5 -10.861 0.377383 -0.274335E-05 0.547026E-09 -0.370191E-13
7 8 5 -10.755 0.377027 -0.251996E-05 0.510587E-09 -0.348091E-13
7 9 5 -11.325 0.375774 -0.162854E-05 0.305559E-09 -0.196119E-13
7 10 5 -11.017 0.377849 -0.285466E-05 0.576783E-09 -0.393355E-13
7 11 5 -11.615 0.377244 -0.271105E-05 0.527251E-09 -0.349436E-13
7 12 5 -11.366 0.380091 -0.291665E-05 4.08751E-09 -9.15842E-13
7 13 5 -11.366 0.377821 -0.291665E-05 0.558033E-09 -0.366265E-13
7 14 5 -10.576 0.378443 -0.323523E-05 0.653182E-09 -0.443832E-13

Efficiency calibrations for HPGe detectors:
Obtained by integrating calibration source (^{152}Eu) transition peak areas and normalizing to respective transition intensities. Relative efficiency curves for HPGe detector numbers # are shown in figures A.1, A.2.
For absolute efficiency values: normalized to 1172 keV-transition of ^{60}Co with activity A=41.881 kBq.

(Det. #, Abs. efficiency)

0 0.0008284619
1 0.0010182152
2 0.0008856384
3 0.0019565824
4 0.0008766435
5 0.0008096586
6 0.0006637738
7 0.0007093862
8 0.0007575385
9 0.0009911837
10 0.0009911837
11 0.0008433617
12 0.0009408661
13 0.0009813051
14 0.0008497231

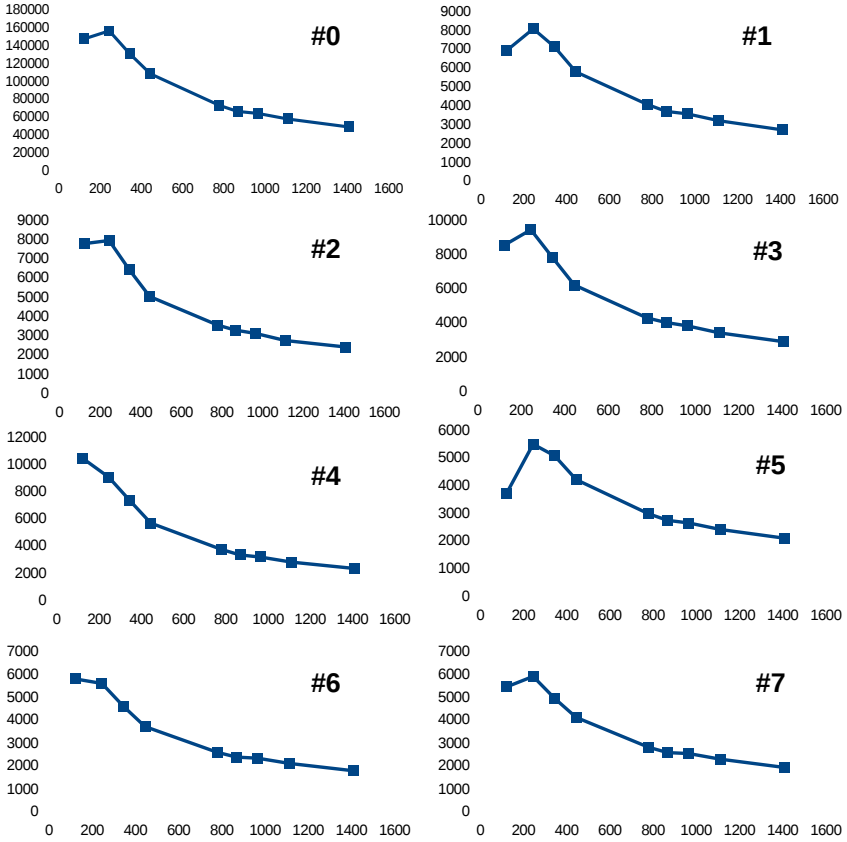

Figure A.1.: Relative efficiencies for ROSPHERE HPGe detectors # 0-7. X-axis: Energy (keV), y-axis: rel. efficiency (arb. units). Line to guide the eye.

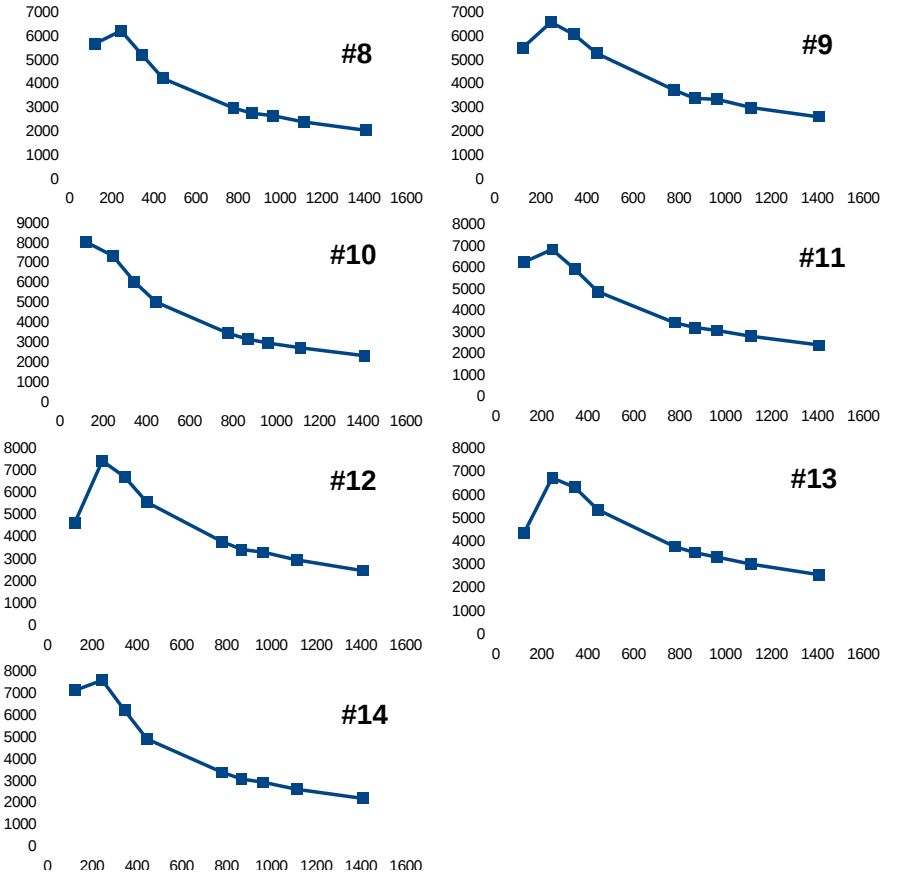

Figure A.2.: Relative efficiencies for ROSPHERE HPGe detectors # 8-14. X-axis: Energy (keV), y-axis: rel. efficiency (arb. units). Line to guide the eye.

DSAM γ-Ray and γ-γ Coincidence Spectra (1)

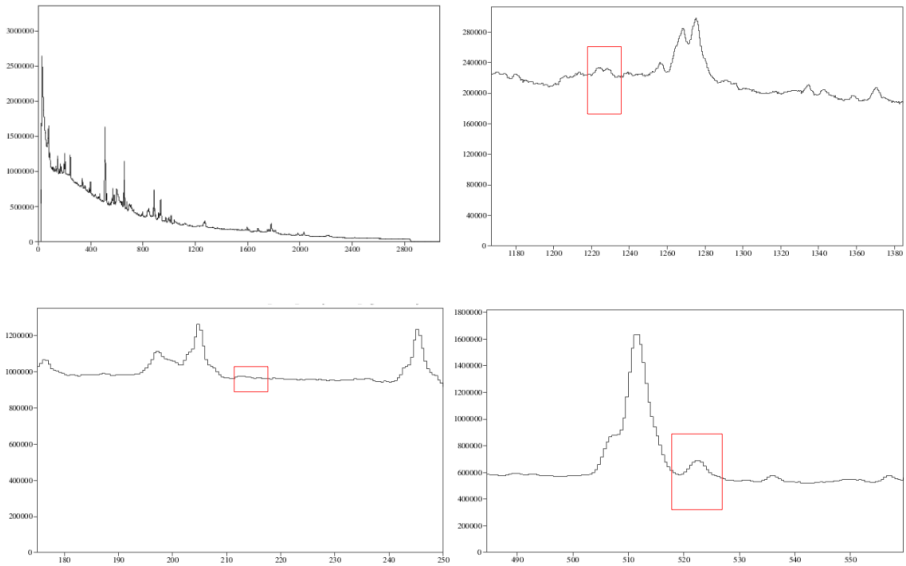

Figure A.3.: γ ray singles spectra measured with in HPGe detectors of ROSPHERE (all angles) with the DSAM target. Top-left: full energy range, top-right: 1222 keV peak, bottom-left: 213 keV peak, bottom-right: 522 keV. X-axis: Energy (keV), y-axis: counts. Transitions of ^{98}Zr are highlighted.

DSAM γ-Ray and γ-γ Coincidence Spectra (2)

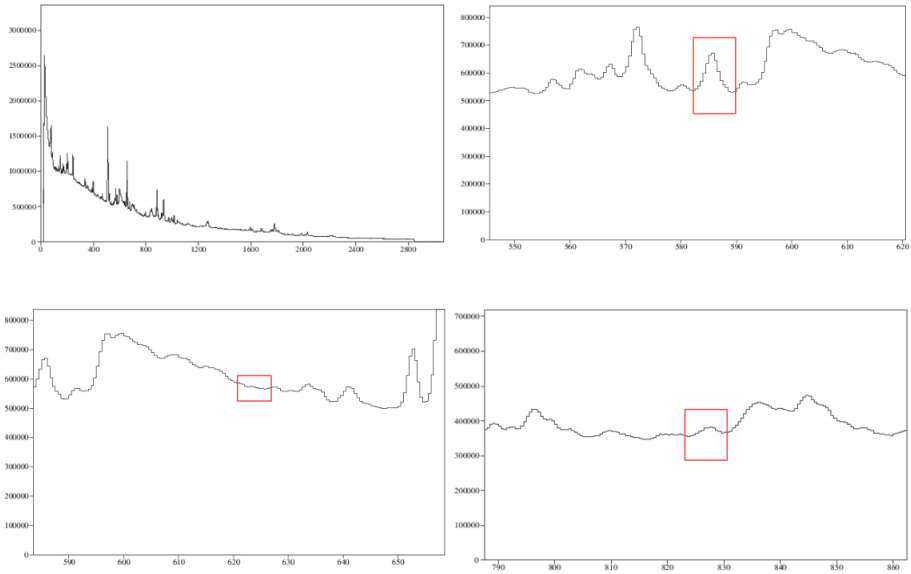

Figure A.4.: γ ray singles spectra measured in the HPGe detectors of ROSPHERE (all angles) with the DSAM target. Top-left: full energy range, top-right: 583 keV peak, bottom-left: 621 keV peak, bottom-right: 825 keV. X-axis: Energy (keV), y-axis: counts. Transitions of ^{98}Zr are highlighted.

DSAM γ-Ray and γ-γ Coincidence Spectra (3)

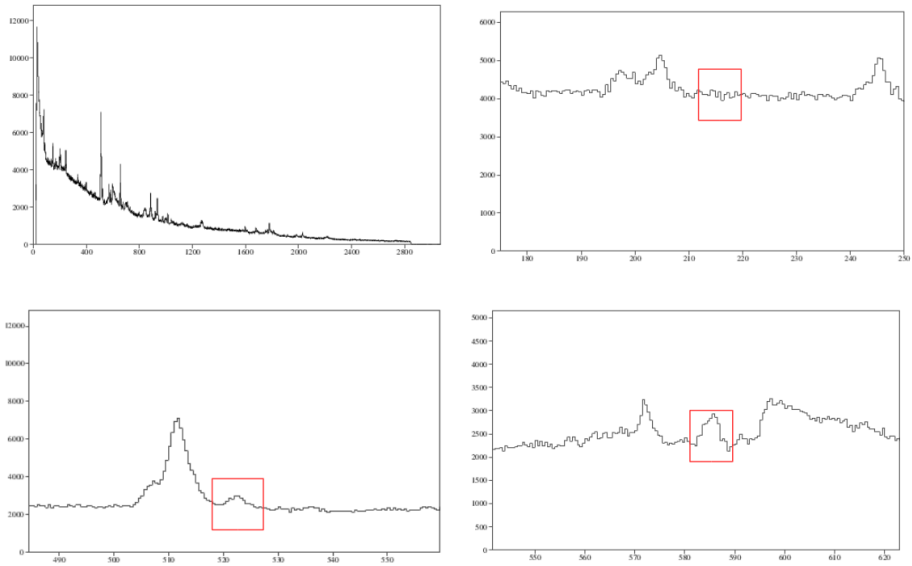

Figure A.5.: γ-γ spectra coincident to the 1222 keV transition of ^{98}Zr measured in the HPGe detectors of ROSPHERE (all angles) with the DSAM target. Top-left: full energy range, top-right: 213 keV peak, bottom-left: 522 keV peak, bottom-right: 583 keV. X-axis: Energy (keV), y-axis: counts. Transitions of ^{98}Zr are highlighted.

DSAM γ-Ray and γ-γ Coincidence Spectra (4)

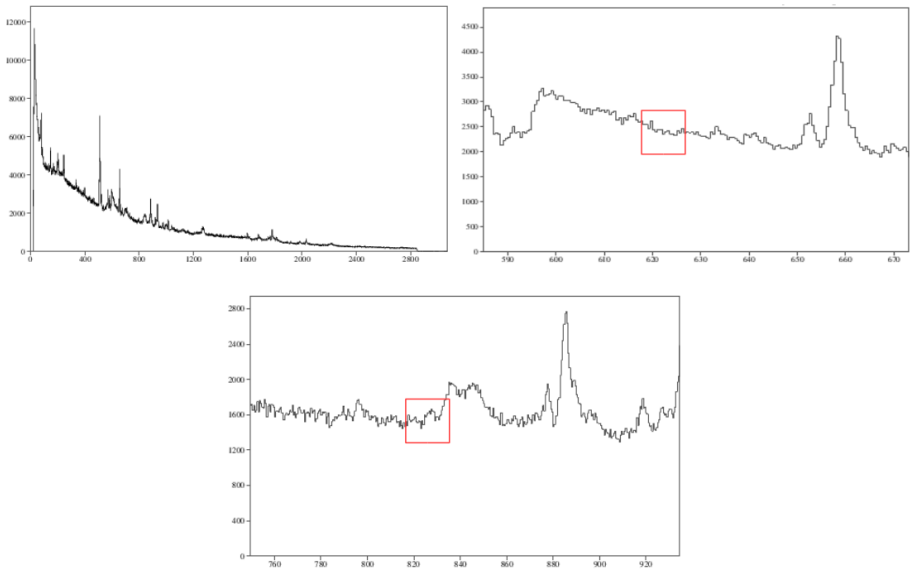

Figure A.6.: γ-γ spectra coincident to the 1222 keV transition of ^{98}Zr measured in the HPGe detectors of ROSPHERE (all angles) with the DSAM target. Top-left: full energy range, top-right: 621 keV peak, bottom: 825 keV peak. X-axis: Energy (keV), y-axis: counts. Transitions of ^{98}Zr are highlighted.

RDDS γ-Ray Spectra (1)

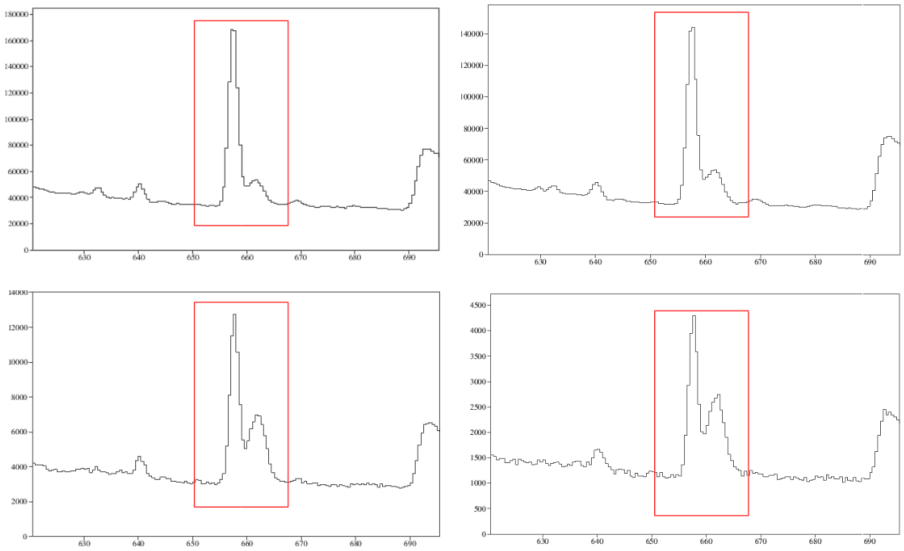

Figure A.7.: γ-ray spectra of the 658 keV transition of ^{110}Cd measured in the HPGe detectors of ROSPHERE (forward angles) with the RDDS target at distance d/μm to the stopper. Top-left: d=25(3), top-right: d=29(3), bottom-left: d=74(2), bottom-right: d=148(2). X-axis: Energy (keV), y-axis: counts. Transitions of ^{110}Cd (unshifted and shifted) are highlighted.

RDDS γ-Ray Spectra (2)

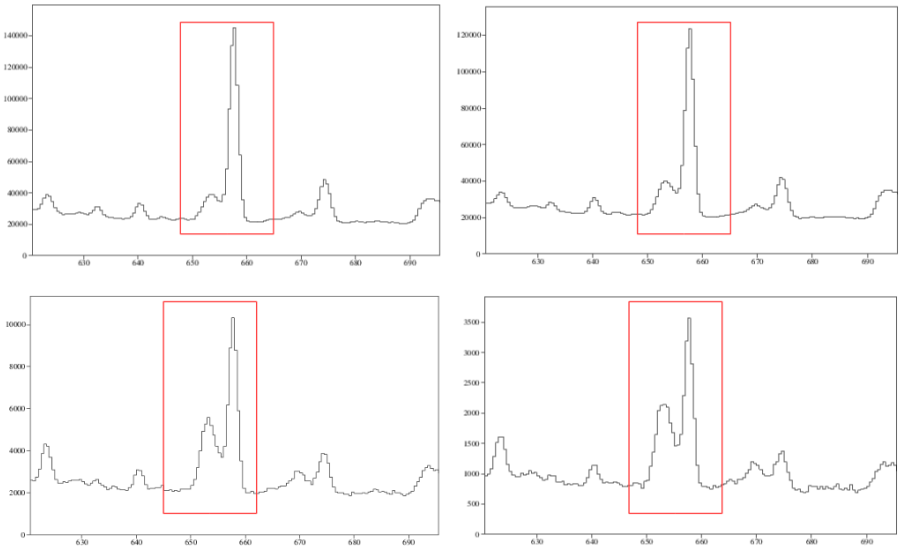

Figure A.8.: γ-ray spectra of the 658 keV transition of ^{110}Cd measured in the HPGe detectors of ROSPHERE (backward angles) with the RDDS target at distance d/μm to the stopper. Top-left: d=25(3), top-right: d=29(3), bottom-left: d=74(2), bottom-right: d=148(2). X-axis: Energy (keV), y-axis: counts. Transitions of ^{110}Cd (unshifted and shifted) are highlighted.

RDDS γ-Ray Spectra (3)

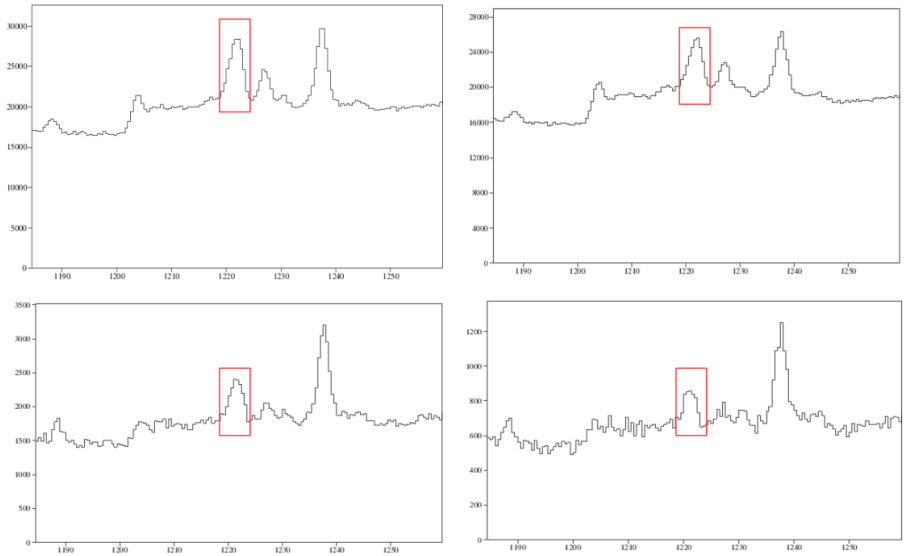

Figure A.9.: γ-ray spectra of the 1222 keV transition of ^{98}Zr measured in the HPGe detectors of ROSPHERE (forward angles) with the RDDS target at distance d/μm to the stopper. Top-left: d=25(3), top-right: d=29(3), bottom-left: d=74(2), bottom-right: d=148(2). X-axis: Energy (keV), y-axis: counts. Transitions of ^{98}Zr (unshifted only) are highlighted.

RDDS γ-Ray Spectra (4)

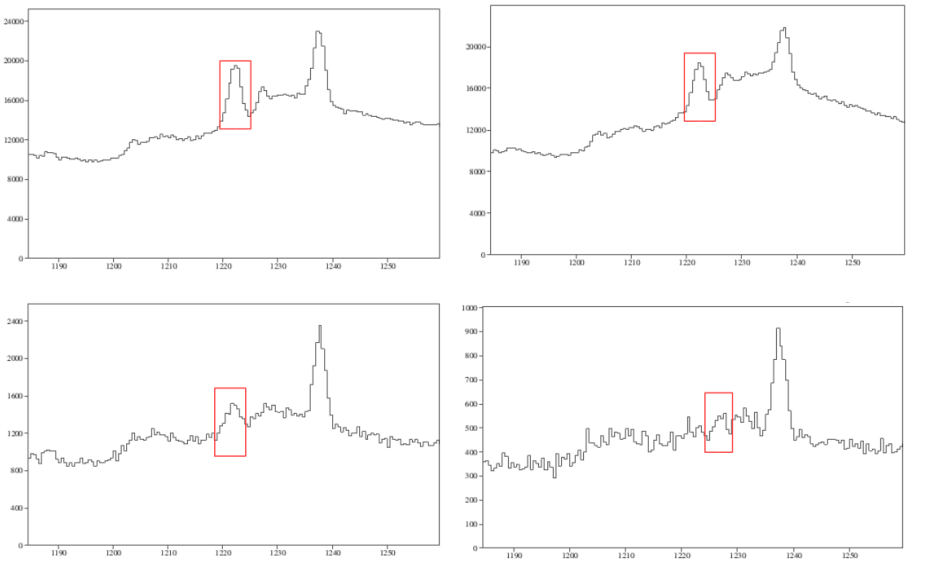

Figure A.10.: γ-ray spectra of the 1222 keV transition of ^{98}Zr measured in the HPGe detectors of ROSPHERE (backward angles) with the RDDS target at distance d/μm to the stopper. Top-left: d=25(3), top-right: d=29(3), bottom-left: d=74(2), bottom-right: d=148(2). X-axis: Energy (keV), y-axis: counts. Transitions of ^{98}Zr (unshifted only) are highlighted.

B List of Figures

C List of Tables

D List of Abbreviations

(2)n: (two-) neutron
A: mass number
abs.: absolute
ANL: Argonne National Laboratory
ATLAS: Argonne Tandem Linac Accelerator System
BGO: bismuth germanate
Bq: Becquerel
c. p.: compare
c: velocity of light (in vacuum)
CAD: computer-aided design
caDSAM: continuous-angle DSAM
CARIBU: Californium Rare Isotope Breeder Upgrade
CHICO: Compact Heavy Ion Counter
Ci: Curie
cont.: Contaminant
CoulEx: Coulomb excitation
d: distance
det.: detector
DSAM: Doppler-Shift Attenuation Method
e. g.: exempli gratia (for example)
ECR: Electron Cyclotron Resonance
eff.: Efficiency
electr.: electronic
etc.: et cetera (and so on)
eV: electronvolt
FE: fusion evaporation
g. s.: ground state
GRET(IN)A: Gamma-Ray Energy Tracking (In-beam Nuclear) Array
HPGe: high-purity germanium
IBA: Interacting Boson Approximation

IBM: Interacting Boson Model
i. e.: id est (that is to say)
IFIN-(HH): Institutul National de Cercetare-Dezvoltare pentru Fizica si Inginerie Nucleara (Horia Hulubei) ([Horia Hulubei] National Institute for R& D in Physics and Nuclear Engineering)
incl.: including
MC: Monte Carlo
MCSM: Monte-Carlo Shell Model
N: neutron number
negl.: neglected
norm.: normalized to
P, **T**, **V** (water): pressure, temperature, volume
PPAC: Parallel Plate Avalanche Counter
QCD: Quantum Chromodynamics
r. h. s.: right-hand side
RDDS: Recoil-Distance Doppler Shift
rel.: relative
RIB(F): Radioactive Ion Beam Facility
ROSPHERE: ROmanian array for SPectroscopy in HEavy ion REactions
SPE: single-particle energy
TAC: Time-to-Amplitude Converter
w. r. t.: with respect to
W. u.: Weisskopf unit
Z: charge number

Elements (Zr, O, Pt, etc.) are referred to by their chemical element symbol according to the periodic table of elements.
Units of measurement (m, s, g, etc.) and their prefixes (mili-, femto-, kilo-, etc.) are used as defined in the International System of Units.

E List of Publications

Journal Papers

D. Kocheva, G. Rainovski, J. Jolie, N. Pietralla, C. Stahl, P. Petkov, A. Blazhev, A. Hennig, A. Astier, Th. Braunroth, M.L. Cortes, A. Dewald, M. Djongolov, C. Fransen, K. Gladnishki, V. Karayonchev, J. Litzinger, C. Müller-Gatermann, M. Scheck, Ph. Scholz, R. Stegmann, P. Thöle, V. Werner, **W. Witt**, D. Wölk, and P. Van Isacker. *Low-lying isovector 2^+ valence-shell excitations of ^{212}Po*, in: Phys. Rev. C 93, 011303(R) (2016)

D. Kocheva, G. Rainovski, J. Jolie, N. Pietralla, A. Blazhev, A. Astier, R. Altenkirch, S. Ansari, Th. Braunroth, M.L. Cortes, A. Dewald, F. Diel, M. Djongolov, C. Fransen, K. Gladnishki, A. Hennig, V. Karayonchev, J.M. Keatings, E. Kluge, J. Litzinger, C. Müller-Gatermann, P. Petkov, M. Rudigier, M. Scheck, Ph. Scholz, P. Spagnoletti, M. Spieker, C. Stahl, R. Stegmann, M. Stoyanova, P. Thöle, N. Warr, V. Werner, **W. Witt**, D. Wölk, K.O. Zell, P. Van Isacker, V.Yu. Ponomarev. *A revised B(E2; $2_1^+ \rightarrow 0_1^+$) value in the semi-magic nucleus ^{210}Po*, in: Eur. Phys. J. A 53, 175 (2017)

W. Witt, V. Werner, N. Pietralla, M. Albers, A. D. Ayangeakaa, B. Bucher, M. P. Carpenter, D. Cline, H. M. David, A. Hayes, C. Hoffman, R. V. F. Janssens, B. P. Kay, F. G. Kondev, W. Korten, T. Lauritsen, O. Möller, G. Rainovski, G. Savard, D. Seweryniak, J. Smith, R. Stegmann, S. Zhu, C. Y. Wu. *Sub-shell closure and shape coexistence in the transitional nucleus ^{98}Zr*, in: Phys. Rev. C 98, 041302(R) (2018)

W. Witt., N. Pietralla, V. Werner, T. Beck. *Data on the Structural Coexistence in the ^{96}Zr Nucleus*, submitted to Eur. Phys. Journal A (2019)

D. A. Sazonov, E. A. Kolganova, T. M. Shneidman, R. V. Jolos, N. Pietralla, **W. Witt**. *Description of shape coexistence in ^{96}Zr based on the collective quadrupole Bohr Hamiltonian*, submitted to Phys. Rev. C, Rapid Communication (2019)

K. Wimmer, F. Recchia, S.M. Lenzi, S. Ricetto, T. Davinson, A. Estrade, C. Griffin, S. Nishimura, F. Nowacki, V. Phong, A. Poves, P.-A. Söderström, O. Atkas, M. Alaqueel, T. Ando, H. Baba, S. Bae, S. Choi, P. Doornenbal, J. Ha, L. Harkness-Brennan, T. Isobe, P.R. John, D. Dahl, G. Kiss, M. Labiche, K. Matsui, S. Momiyama, D.R. Napoli, M. Niikura, C.R. Nita, Y. Saito, H. Sakurai, P. Schrock, C. Stahl, T. Sumikama, V. Werner, **W. Witt**. *First spectroscopy of ^{61}Ti and the transition to the Island of Inversion at $N = 40$*, submitted to Phys. Let. B (2019)

W. Witt, V. Werner, et al. *RDDS Lifetime Measurement of the 2_1^+ State of ^{98}Zr*, to be submitted to Eur. Phys J. A (2019)

Conference Proceedings

D. Kocheva, G. Rainovski, J. Jolie, N. Pietralla, C. Stahl, P. Petkov, A. Blazhev, A. Hennig, A. Astier, Th. Braunroth, L. Cortes, A. Dewald, M. Djongolov, C. Fransen, K. Gladnishki, V. Karayonchev, J. Litzinger, C. Müller-Gatermann, M. Scheck, Ph. Scholz, C. Schramm, P. Tölle, V. Werner, **W. Witt**, D. Wölk and P. Van Isacker. *Search for mixed-symmetry states in ^{212}Po*, in: J. Phys.: Conf. Ser. 724, 012023 (2016).

D. Kocheva, G. Rainovski, J. Jolie, N. Pietralla, A. Blazhev, A. Astier, R. Altenkirch, M. Bast, M. Beckers, S. Ansari, Th. Braunroth, M. Cappellazzo, M.L. Cortes, A. Dewald, F. Diel, M. Djongolov, C. Fransen, K. Gladnishki, A. Goldkuhle, A. Hennig, V. Karayonchev, J.M. Keatings, E. Kluge, Th. Kröll, J. Litzinger, K. Moschner, C. Müller-Gatermann, P. Petkov, M. Rudigier, M. Scheck, P. Spagnoletti, Ph. Scholz, T. Schmidt, M. Spieker, C. Stahl, R. Stegmann, A. Stolz, A. Vogt, M. Stoyanova, P. Thöle, N. Warr, V. Werner, **W. Witt**, D. Wölk, J.C. Zamora, K.O. Zell, P. Van Isacker. *Low*

collectivity of the first 2^+ states of $^{212,210}Po$, in: Journal of Physics: Conference Series 1023, 01209 (2018)

N. Pietralla, C. Kremer, M. Lettmann, S. Aslanidou, A. Krugmann, C. Lizarazo, P. von Neumann-Cosel, V. Werner and **W. Witt**. *Shell Evolution and E2 collectivity: New Spectroscopic Information*, in: Journal of Physics: Conference Series 966, 012058 (2018)

N. Pietralla, C. Kremer, T. Beck, **W. Witt**, U. Gayer, P. von Neumann-Cosel, V. Werner. *Shell Evolution and E2 Collectivity: New Spectroscopic Information*, in: EPJ Web Conf. 178, 2007 (2018)

F. Recchia, K. Wimmer, S.M. Lenzi, S. Riccetto, T. Davinson, A. Estrade, C. Griffin, S. Nishimura, F. Nowacki, V. Phong, A. Poves, P.-A. Söderström, O. Aktas, M. Alaqueel, T. Ando, H. Baba, S. Bae, S. Choi, P. Doornenbal, J. Ha, L. Harkness-Brennan, T. Isobe, P.R. John, D. Kahl, G. Kiss, M. Labiche, K. Matsui, S. Momiyama, D.R. Napoli, M. Niikura, C. Nita, Y. Saito, H. Sakurai, P. Schrock, T. Sumikama, C. Stahl, V. Werner, **W. Witt**. *Isomer spectroscopy in odd-even Ti isotopes: approaching N=40*, in: Zakopane 2018 proceedings, Acta Phys. Pol. B48 (to be published in March 2019)

R.L. Canavan, M. Rudigier, P.H. Regan, P.A. Söderström, M. Lebois, J.N. Wilson, N. Jovancevic, S. Bottoni, M. Brunet, N. Cieplicka-Orynczak, S. Courtin, D.T. Doherty, K. Hadynska-Klek, M. Heine, I.W. Iskra, V. Karayonchev, A. Kennington, P. Koseoglou, G. Lotay, G. Lorusso, M. Nakhotsin, C.R. Nita, S. Oberstedt, Zs. Podolyak, L. Qi, J.-M. Regis, R. Shearman, P.M. Walker, **W. Witt**. *Excited State Lifetime Studies in the N = 100 Isotone ^{166}Dy* , in: Zakopane 2018 proceedings, Acta Phys. Pol. B48 (to be published in March 2019)

M. Rudigier, R.L. Canavan, P.H. Regan, P.A. Söderström, M. Lebois, J.N. Wilson, N. Jovancevic, S. Bottoni, M. Brunet, N. Cieplicka-Orynczak, S. Courtin, D.T. Doherty, K. Hadynska-Klek, M. Heine, I.W. Iskra, V. Karayonchev, A. Kennington, P. Koseoglou, G. Lotay, G. Lorusso, M. Nakhotsin,

C.R. Nita, S. Oberstedt, Zs. Podolyak, L. Qi, J.-M. Regis, R. Shearman, P.M. Walker, **W. Witt**. *Isomer Spectroscopy and Sub-Nanosecond Lifetime Determination in ^{178}W Using the NuBALL Array*, in: Zakopane 2018 proceedings, Acta Phys. Pol. B48 (to be published in March 2019)

Conference Contributions

W. Witt, N. Pietralla. *O(6) – Symmetry in the ^{196}W region*, in: NUSTAR Week, York, England, Sept. 2016

W. Witt. *CoulEx - Measurement of the B(E2; $2_1^+ \rightarrow 0_1^+$) in ^{98}Zr using GRETINA & CHICO2 at ANL*, in: DPG-Frühjahrstagung 2017, Münster, Deutschland, Mar. 2017

W. Witt. *The shape-transitional ^{98}Zr: Measurement of the 2_1^+ B(E2) value with GRETINA/CHICO2 at ATLAS/CARIBU*, in: NUSPIN workshop, Darmstadt, Germany, June 2017

W. Witt. *S452 - The Oblate-Prolate Shape Transition around A ∼190*, in: NUSTAR Annual Meeting 2018, Darmstadt, Germany, Febr. 2018

W. Witt. *RDDS Lifetime Measurement on Zr-98 - Fixing the Critical Point of the Quantum Phase Transition*, accepted submission for DPG-Frühjahrstagung 2019, Munich, Germany, Mar. 2019

Laboratory Reports

W. Witt, P. Koseoglou, I. Kojouharev, J. Gerl, *Tests of Sunpower CryoTel CT Stirling cooling engine for DEGAS*, in: GSI Scientific Report 2016 (2017).

F. Recchia, S. Riccetto, K. Wimmer, S.M. Lenzi, T. Davinson, A. Estrade, C. Griffin, S. Nishimura, V. Phong, P.-A. Söderström, O. Aktas, M.

Alaqueel, T. Ando, H. Baba, S. Bae, S. Choi, P. Doornenbal, J. Ha, L. Harkness-Brennan, T. Isobe, P.R. John, D. Kahl, G. Kiss, M. Labiche, K. Matsui, S. Momiyama, D.R. Napoli, M. Niikura, C. Nita, Y. Saito, H. Sakurai, P. Schrock, T. Sumikama, C. Stahl, V. Werner, **W. Witt**. *Shape Coexistence Along N = 40 Studied with Isomer and Beta Decay*, in: LLNL Annual Report 2016 (2017)

I. Zanon, M. Siciliano, A. Goasduff, P.R. John, D. Bazzacco, D. Ashad, G. Benzoni, B. Birkenbach, A. Boso, T. Braunroth, M. Cicerchia, N. Cieplicka, G. Colucci, F. Davide, G. de Angelis, B. de Canditiis, A. Gadea, F. Galterossa, L.P. Gaffney, A. Gozzelino, K. Hadynska-Klek, G. Jaworski, P. Koseoglou, S.M. Lenzi, B. Melon, R. Menegazzo, D. Mengoni, A. Nannini, D.R. Napoli, J. Pakarinen, D. Quero, P. Rath, F. Recchia, M. Rocchini, D. Testov, J.J. Valente-Dobon, A. Vogt, J. Wiederhold, **W. Witt**. *Shape Coexistence in the Neutron-Deficient ^{188}Hg Isotope*, in: LNL report 2017 (2018).

S. Gaire, A. Estrade, D.S. Ahn, M. Amthor, O. Aktas, H. Baba, S. Bae, P. Coleman-Smith, T. Davinson, P. Doornenbal, N. Fakuda, C. Griffin, Z. Ge, J. Ha, L. Harkness-Brennan, T. Isobe, N. Inabe, D. Kahl, G. Kiss, T. Kubo, S. Kubono, M. Labiche, G. Larusso, G. Lotay, Y. Litvinov, C. Lizarazo, B. Moon, F. Montes, K. Matsui, S. Momiyama, S. Naimi, S. Neupane, S. Nishimura, C.R. Nita, V. Phong, F. Recchia, S. Riccetto, H. Sakura, Y. Saito, P. Schrock, Y. Shimizu, P.A. Säderström, H. Suzuki, T. Sumikama, H. Takeda, V. Werner, K. Wimmer, **W. Witt**, P. Woods, K. Yoshida. *Mass and β-decay measurement of neutron-rich nuclei around N=56*, in: RIKEN RIBF Accelerator Progress Report 2018 (2018)

J. Wiederhold, R. Kern, C. Lizarazo, **W. Witt**, V. Werner, N. Pietralla, D. Bucurescu, N. Florea, D. Ghita, T. Glodariu, R. Lica, N. Marginean, R. Marginean, C. Mihai, R. Mihai, I.O. Mitu, A. Negret, C. Nita, A. Olacel, S. Pascu, L. Stroe, S. Toma, A. Turturica. *Fast-timing lifetime measurement of ^{152}Gd with FATIMA-type $LaBr_3$ detectors* , in: GSI-FAIR Scientific Report 2017 (2018)

P.-A. Söderström, M. Rudigier, T. Arici, S. Bottoni, M. Brunet, R. Canavan, N. Cieplicka-Orynczak, S. Courtin, D. Doherty, J. Ger, M. Gorska, K. Hadynska-Klek, M. Heine, L.W. Iskra, N. Jovancevic, V. Karayonchev, A. Kennington, I. Kojouharov, P. Koseoglou, M. Lebois, N. Kurz, C. Lizarazo, G. Larusso, G. Latay, M. Nakhostin, C.R. Nita, S. Oberstedt, N. Pietralla, S. Pietri, Zs. Podolyak, L. Qi, P.H. Regan, J.-M. Regis, S. Saha, H. Schaffner, R. Shearman, J. Vesic, J. Wilson, **W. Witt**. Fast timing with FATIMA - From νBall at ALTO to DESPEC at GSI, in: GSI-FAIR Scientific Report 2017 (2018)

W. Witt, P. Koseoglou, P.-A. Söderström, E. Adamska, J. Gerl, I. Kojouharev, N. Pietralla, *Characterization of a Sunpower CryoTel CT cooling engine for DEGAS*, in: GSI-FAIR Scientific Report 2017 (2018).

F Curriculum Vitae

Removed in this public version.